Coastal flows driven by vorticity

Oliver Robert Southwick

Department of Mathematics

University College London

A thesis submitted in conformity with the requirements for the degree of Doctor of Philosophy.

Supervised by Prof. E. R. Johnson and Prof. N. R. McDonald

March, 2016

I, Oliver Robert Southwick, confirm that the work presented in this thesis is my own. Where information has been derived from other sources, I confirm that this has been indicated in the thesis.

SIGNED

Abstract

This thesis develops and applies simple models to investigate coastal flows driven by vorticity and compares these results to existing observations, experiments, numerical models and theory. Two main phenomena are considered: the generation of ocean eddies by flow separation along coastlines; and outflows into the coastal ocean from rivers and straits. In both of these cases, simple models in quasigeostrophic $1\frac{1}{2}$-layer flow are developed, analysed and solved numerically.

Eddies may be formed as flow separates at sharply varying topography, shedding vorticity into the main flow. Recent work by Dewar et al. [2015], Gula et al. [2015] and Molemaker et al. [2015] shows that vertical eddy diffusivity is sufficient on its own to introduce intense horizontal shear layers at sloping ocean margins. As the shear layer detaches it typically rolls up into a concentrated eddy. These shed eddies, or "sheddies", may have significant oceanographic impacts. Here a point vortex model for the formation and evolution of these sheddies is developed based on the Brown and Michael [1954] model for two-dimensional vortex shedding, adapted to more realistically model mesoscale oceanic flow by including a deforming free surface. With a free surface, the streamfunction for the flow is not harmonic so the conformal mapping methods used in the standard Brown–Michael approach cannot be used and the problem must be solved numerically. A numerical scheme is developed based on a Chebyshev spectral method for the streamfunction partial differential equation and a second order implicit timestepping scheme for the vortex position ordinary differential equations. The results of the model are first tested and examined for the simple case of eddies shed from the tips of infinite wedges with various ambient flows, then are applied to a number of oceanographic examples. The model shows good qualitative agreement with observations and experimental and numerical results. It is applied to a number of well known cases of sheddy formation, including the

Agulhas Cyclones, California Undercurrent and Canary Eddy Corridor, and also to investigate the effects of shed vorticity in the growth of the Cook Strait Eddy and the interaction of the North Brazil Current Rings with the islands of the Lesser Antilles.

Outflows from rivers or through straits into the coastal ocean form distinct features which are highly important both dynamically and ecologically. Significant observational, experimental, numerical modelling and theoretical attention has been devoted to investigating the dynamics of coastal outflows, which can be highly complex due to non-linearity, the range of temporal and spatial scales, time-dependence and influencing effects including buoyancy, rotation, bathymetry, currents, tides, winds and mixing. Due to this complexity, theoretical investigations have typically focussed on one aspect or area of the flow in isolation or have developed scalings or qualitative representations of the dynamics.

Here, a simple quasigeostrophic model representing an outflow as a source of constant potential vorticity fluid expelled into an initially quiescent ocean is presented. This focusses on the key dynamics: the rotation modified outflow velocity and the generation of vorticity as the buoyant fluid adjusts, and enables the full evolution to be investigated. The complex and varied results are explored in detail with contour dynamics simulations. Using a long wave approximation, analytical results, which accurately describe the outflow evolution, are derived, with the significant insight they offer and their relation to existing oceanographic studies discussed. These solutions give the form of variable width steady boundary profiles, showing for what parameters these exist or the outflow grows offshore indefinitely. It is shown that the unsteady heads leading the outflow are described by simple analytical expressions. The formation and evolution of shocks in the solution are accurately predicted and computed by analysing the long wave speed, and for simple source velocity profiles the full time-dependent solution is found.

The model is extended to consider the effects of variable source strength, ambient alongshore currents, tides and winds using both contour dynamics and extensions to the long wave theory. A consideration of the momentum fluxes in the model is used to understand the turning of the current but also enables the momentum imbalance paradox of Pichevin and Nof [1997] to be resolved, showing that steady solutions are indeed possible. A new numerical scheme to compute steady profiles is developed.

Citations to previously published work

Chapter 2 is based on the paper

> "A point vortex model for the formation of ocean eddies by flow separation",
> O. R. Southwick, E. R. Johnson, N. R. McDonald, *Physics of Fluids*, 27 (1), 2015.

Chapter 3 has been submitted as the paper

> "A simple model for "sheddies" – ocean eddies formed from shed vorticity",
> O. R. Southwick, E. R. Johnson, N. R. McDonald, *Journal of Physical Oceanography*, submitted 2016.

Chapters 4 and 5 form the basis of the papers

> "Rotating vortical outflows",
> E. R. Johnson, O. R. Southwick, N. R. McDonald, *Journal of Fluid Mechanics*, submitted 2016.

> "Potential vorticity dynamics of coastal outflows",
> O. R. Southwick, E. R. Johnson, N. R. McDonald, *Journal of Physical Oceanography*, submitted 2016.

Acknowledgements

It has been a pleasure to work under the supervision of Ted Johnson and Robb McDonald. I have benefited enormously from their expertise, their approach to research and to communicating your work, and to their sharp and rapid insight. I also owe them thanks for being so supportive of me in pursuing a range of activities alongside our research.

I have greatly enjoyed my time at UCL and owe my thanks to all the staff of the Maths Department, but especially to my Ph.D. colleagues Adam, Ali, Anna, Belgin, Doaky, Gin, Huda, Jamie, Mart, Peter, Pietro, Raf, Sam, Scroggs and Tom for their help and friendship, and to Helen and Soheni for putting up with me. My thanks also go to the Engineering and Physical Sciences Research Council for funding my research project.

Contents

Chapter 1

Introduction

1.1 Sheddies - ocean eddies formed from shed vorticity

Eddies play an important role in oceanic circulation by transporting significant amounts of heat, salt, mass and momentum. Those on the mesoscale (∼10–500 km in diameter) can be highly coherent features with lifespans of months, or even years, enabling them to travel across entire ocean basins. While large enough to be significant, these eddies are small enough to be difficult to resolve in global ocean models. Indeed, all such models must include a parametrisation of the effects of eddies at some scale. Therefore, an improved understanding of the generation and dynamics of eddies is important for further improvement in large scale ocean modelling. One aspect of this must be an understanding of the dynamics of eddies in the presence of topographic features. Long-lived eddies have been observed to interact with topographic features such as islands, mid-ocean ridges and sea-mounts. The North Brazil Current Rings, which contribute substantially to the Atlantic Meridional Overturning Circulation [Jochumsen et al., 2010], often interact with the islands of the Lesser Antilles [Simmons and Nof, 2002]. Typically, they either disintegrate upon collision or pass between the islands. As such, they have received significant theoretical, observational, numerical and experimental attention [Cenedese, 2005, Duran-Matute and Velasco Fuentes, 2008]. Another example are the lenses of dense, salty water of Mediterranean origin known as 'meddies', which propagate deep in the North At-

lantic and are observed to frequently interact with sea-mounts [Richardson et al., 2000].

Since the large horizontal lengthscales of oceanic flows give Reynolds numbers typically of the order of 10^{11}, viscous effects are generally negligible. Exceptions occur in thin boundary layers, which can nevertheless be highly important. In typical ocean models, boundary layers at lateral boundaries are assumed insignificant and only the much thinner boundary layers on the upper and lower boundaries are considered. Recent work [Dewar et al., 2015, Gula et al., 2015, Molemaker et al., 2015] considers the effect of the turbulent bottom boundary layer over sloping bathymetry, and demonstrates that the vertical shear in the bottom boundary layer necessarily implies a horizontal shear as well. Importantly, this effect does not require horizontal viscosity: the vertical eddy viscosity introduces horizontal shear. Full representation of these horizontal shear layers requires the inclusion of sloping boundaries, no slip boundary conditions and high resolution, which are not achieved in most global models. Molemaker et al. [2015] estimate the horizontal scale of the boundary layer in the California Undercurrent as 200 m or less. Such fine features are not accurately resolved even in the finest of their three nested grids.

Provided the shear layers remain attached to the lateral boundaries, low horizontal diffusivity means that their vorticity remains confined to the boundary and does not influence the interior flow. However, if the shear layer detaches at a point of adverse pressure gradient or at a sharp change in direction of the boundary, vorticity is ejected from the layer into the interior of the fluid and can become dynamically significant in the interior flow. It is the aim of the work here to model the effect of the ejection of boundary vorticity. This tackles directly the difficulty of achieving realistically large Reynolds numbers in numerical ocean models. Vorticity diffusion is negligible in the bulk of the flow away from the boundaries and so a simple model that tracks vorticity in the interior flow can accurately model many aspects of the flow.

Molemaker et al. [2015] run detailed nested-grid simulations using the Regional Ocean Modelling System (ROMS). An example of one of their high resolution simulations of the Californian Undercurrent is shown in fig. 1.1. The shear layer can be seen attached to the wall in the bottom right of the figure with its strong negative

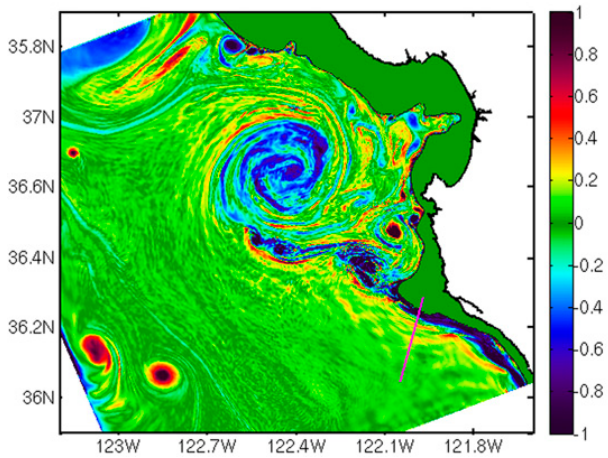

Figure 1.1: Normalised relative vorticity in the California Undercurrent showing the shear layer separating at Point Sur from the ROMS simulation of Molemaker et al. [2015].

vorticity coloured dark blue. As the current flows northward past the headland at Point Sur the shear layer detaches, shedding vorticity into the main flow. The instabilities of this layer of vorticity initially form a number of small eddies before rolling up into a single large eddy. This work builds on the work of Dewar, Molemaker, McWilliams and Gula by modelling the evolution of the detached shear layer into a coherent shed eddy, or "sheddy".

Ocean eddies created by flow separation have frequently been observed around islands such as the Canaries [Piedeleu et al., 2009] and Izu Islands [Isoguchi et al., 2009] and capes such as Cape Ann [Jiang et al., 2011]. These eddies are often mesoscale [Heywood et al., 1996, Jiang et al., 2011, Takikawa et al., 2011] and their dynamics can be affected by rotation (away from the equator) [Heywood et al., 1996] and stratification. They are of significant biological—as well as physical—interest as they can cause strong upwelling and increased levels of chlorophyll and phytoplankton production: the 'island mass effect' [Andrade et al., 2014]. Topographic forcing of the oceanic flow has been shown to be the main mechanism for the eddy generation—with wind shear acting as an additional supporting source of vorticity—in observational [Piedeleu et al., 2009] and numerical [Jiménez et al., 2008] investigations of eddy generation from Gran Canaria. The stability of island wakes in the flow of rotating, stratified, shallow water has been studied experimentally using the three-dimensional LEGI Coriolis Platform [Teinturier et al., 2010]. As such, the formation of eddies by flow separation has received significant observational, experimental and numerical

attention. Numerical investigations have often aimed to realistically capture the full complexity of the flow with relatively complex models. For example, the wake of the ocean flow past the Madeira archipelago was recently investigated using a three-dimensional primitive equation model with realistic bathymetry [Caldeira and Sangrà, 2012]. It would be complementary to these approaches to develop a simplified model that captures the key features of the flow but which is easier to implement and understand. A model which isolates the key physical process in a simple way will benefit understanding and aid interpretation of the results of more complex models, experiments and observations. Additionally such a model will have the significant extra benefit of being much cheaper to implement numerically than more complex approaches.

Simple low-order models have many important strengths when considering the dynamics of ocean eddies. Many eddies are below the grid size of large scale ocean models but are still dynamically important, meaning that their effects must be parametrised. Modelling helps build effective and physically appropriate parametrisations. It is often not possible to achieve realistically large Reynolds numbers in numerical ocean models and indeed it may not be necessary. An appropriate alternative approach to modelling extremely high Reynolds number flow may be to use inviscid models with no interior viscous effects and boundary viscous effects represented solely by their vortical dynamics.

Although oceanic flows have very high Reynolds number, the highly coherent eddies observed in the lee of islands match well to numerical experiments which show that, for rotating, stratified flows, coherent vortices are found for all values of the Reynolds number [Dong et al., 2007]. However it may not be possible to apply standard results from the wake of a cylinder to all island shapes. Observations of island wakes with differing flow direction but otherwise similar conditions show significantly different wakes [Heywood et al., 1996], suggesting that it is important to consider the coastal shape. This work therefore considers a number of examples of different coastal shapes representing different oceanic scenarios.

The simplest approach to modelling ocean eddies is to consider a constant-depth barotropic ocean, with point vortices and topography extending vertically through the entire fluid depth. The flow dynamics then evolve according to the two-

dimensional Euler equations. This model enables significant analytical progress with complex variable methods and has been used in a number of works which consider different configurations of topography. Johnson and McDonald used conformal mapping techniques to construct the vortex Hamiltonian (Kirchoff–Routh path function) for a point vortex and compared it to the motion of an initially circular vortex patch in various domains: a single gap in a wall [Johnson and McDonald, 2004a], two circular islands [Johnson and McDonald, 2004b], multiple circular islands using the point island approximation [Johnson and McDonald, 2005a] and a wall with multiple gaps [Johnson and McDonald, 2005b]. They found that the centroid of the patch very closely followed the trajectory of a point vortex except when the patch deformed significantly, as it does, for example, when it approaches a horizontal boundary. Crowdy and Marshall [2005a] derived the vortex Hamiltonian for N point vortices in multiply connected domains and applied it to find point vortex trajectories around multiple circular islands [Crowdy and Marshall, 2005b] and vortex trajectories in more general multiply connected slit domains by conformally mapping them to circular domains [Crowdy and Marshall, 2006]. As well as the case of a flat plane, these techniques have been expanded to vortex motion on a sphere with boundaries [Nelson and McDonald, 2009].

While this model enables a large number of exact solutions, in many oceanographic contexts it may be appropriate to include the effect of surface deformation. This surface could either be a fluid–air interface or the interface between two layers of different density. Surface deformation is modelled using the quasigeostrophic (QG) flow equations and has a single parameter: the Rossby radius of deformation (or simply 'Rossby radius'), which is the lengthscale over which surface perturbations decay. A constant depth fluid is the limiting case when the Rossby radius goes to infinity and is often referred to as the 'rigid-lid limit'. From here onward, fluid with finite Rossby radius will be referred to simply as a quasigeostrophic or QG flow, and constant depth fluid (i.e. infinite Rossby radius flow) will be referred to as rigid-lid flow. QG flow is not harmonic so the complex variable methods previously applied cannot be used, meaning that exact solutions are difficult to find and numerical approaches must be employed instead. Nilawar et al. [2012] considered the motion of a point vortex approaching a gap in a wall for QG flow. For various Rossby radii,

they calculated point vortex trajectories numerically using boundary integral methods and compared them to the motion of vortex patches computed with contour dynamics. They found that with lower Rossby radius, the vortices were more likely to pass through the gap.

Many of the shapes of topography previously considered (e.g. semi-infinite plates, gaps in walls and wedges) feature sharp corners representing sharply curving boundary topography. In these situations, without viscosity, the flow field typically becomes singular at the boundary corners. In reality this unphysical effect is prevented by flow separation at the sharp corner. Flow at large Reynolds number around obstacles—especially obstacles with a sharp point—typically separates, shedding the viscous boundary layer out into the flow. This shed fluid has high vorticity and rolls up into a concentrated core: a shed eddy, or "sheddy".

A simple approach to modelling flow separation is to focus on the developing core of vorticity as the most dynamically important feature and represent this as a single point vortex. The strength of this vortex increases as vorticity leaves the boundary layer at the separation point and rolls up. The vorticity distribution is determined by requiring that the velocity remain finite at the separation point: a Kutta condition. Irrotational flow of inviscid fluid around a corner has infinite velocity at the corner. The presence of even infinitesimal viscous effects at sufficiently high Reynolds number means the flow separates at the corner. In the model here, the vorticity shed at the corner is taken to roll up into a point vortex whose strength increases continuously, following Brown and Michael [1954] who derived an equation of motion for the location of a shed eddy through a force balance argument.

The Brown–Michael model has been shown to capture the qualitative features of high Reynolds number, two-dimensional, incompressible, non-rotating flows and has been used, and further developed, extensively [Cortelezzi and Leonard, 1993, Graham, 1983, Rott, 1956]. As well as traditional applications in aeronautics [Manela and Huang, 2013] it has been applied to a variety of problems such as swimming [Sheng et al., 2011, Ysasi et al., 2011], biological models such as ventricle filling [Pedrizzetti, 2010] and coupled solid-fluid interactions such as a falling playing card or a flapping flag [Michelin and Llewellyn Smith, 2010, Michelin et al., 2008, Michelin and Llewellyn Smith, 2009]. The model shows good qualitative agreement with

both experimental results [Blondeaux and De Bernardinis, 1983], more sophisticated models [Sheng et al., 2011] and high resolution numerical simulations [Eldredge and Wang, 2010] in a variety of flow situations. It was compared to a vortex sheet method and a penalised Navier–Stokes method in a model of the wake produced by a swimming fish [Sheng et al., 2011]. The wake structures produced by the three methods were qualitatively similar (as shown in their Fig.(2), (3) and (4)) and the shed circulation and drag coefficient were of the same order of magnitude but with more significant differences across the three methods. A comparison between the Brown–Michael method and a more sophisticated numerical solution of the Navier–Stokes equations using a viscous vortex particle method showed good qualitative agreement in an investigation of flow separation over a rapidly pitching plate [Eldredge and Wang, 2010]. As well as a range of applications, there have also been developments on the model itself. Cortelezzi [1995] solved the equation of motion for a vortex shed from a semi-infinite plate for any free-stream condition and derived a time-dependent scaling that collapses all solutions onto the impulsively started case. Howe [1996] studied sound generated by a vortex translating around a semi-infinite plate and proposed an amended Brown–Michael equation where the vortex motion is set to cancel a previously unbalanced reaction force caused by the residual couple. Here, a new Brown–Michael model will be derived for quasigeostrophic flow and applied to a number of situations of oceanographic interest.

1.2 Coastal outflows

Outflows of buoyant fluid to the coastal ocean from rivers or straits connecting seas and ocean basins can be highly important features both dynamically and ecologically. More than a third of land-based rainfall transits to the ocean through rivers [Trenberth et al., 2007]. The fluid in the source may have significantly different temperature, salinity or depth to the ambient and will adjust and gain relative vorticity as it is expelled [Spall and Price, 1998]. These differing properties may cause dramatic ecological effects, supporting marine ecosystems but also serving as sources of pollutants such as in the eutrophied dead zone of the Mississippi plume [Rabalais et al., 2002].

The dynamics of coastal outflows can be highly complex due to non-linearity, the range of temporal and spatial scales, time-dependence and the significant number of influencing effects including buoyancy, rotation, bathymetry, currents, tides, winds and mixing. However the dynamics can be understood and classified into categories based on the Kelvin and Rossby numbers. Garvine [1995] identifies the Kelvin number, the ratio of the typical current width to the Rossby radius, as a key diagnostic of outflow dynamics. Small scale outflows such as the River Teign in Devon or those close to the equator such as the Amazon, have small Kelvin number so are not affected significantly by rotation, and tend to form radially spreading outflows. Outflows with large Kelvin number, comprising large-scale mid- and high-latitude outflows such as the Delaware and Rhine plumes and the Algerian and Norwegian coastal currents, are affected significantly by rotation. These typically form asymmetric outflows which turn in the direction of Kelvin wave propagation, hereafter referred to as "downstream" (rightward in the Northern Hemisphere, leftward in the Southern Hemisphere), and form coherent coastal currents stretching up to hundreds of kilometres along the coast.

The second key parameter is the Rossby number of the outflow. For narrow sources with high discharge, such as the Columbia River [Hickey et al., 1998, Horner-Devine, 2009] and Hudson River [Chant et al., 2008] plumes, the Rossby number is large enough that inertia is dynamically significant in the near source region. In these cases a large, roughly circular bulge grows near the source and a much smaller coastal current carrying only a fraction of the source flux is formed [Avicola and Huq, 2003, Horner-Devine et al., 2008]. The bulge region is in gradient-wind balance but the coastal current is in geostrophic balance [Horner-Devine et al., 2006, Yankovsky and Chapman, 1997]. For wider sources, or when the outflow velocity is not as large, such as the Chesapeake Bay or Delaware Bay outflows, the Rossby number is low and the near-source region is in geostrophic balance with a smaller bulge and more of the source flux entering the coastal current [Fong and Geyer, 2002, Horner-Devine et al., 2015]. Buoyancy is important in the dynamics of outflows with the expelled fluid adjusting in depth and gaining vorticity via the stretching or squashing of vortex columns. While this generation of relative vorticity or differences in potential vorticity from the source to the ambient fluid is not always discussed explicitly in

studies of outflows, it has been investigated in a number of works including observational [Lake et al., 2005], experimental [Lane-Serff and Baines, 2000] and modelling [Marques et al., 2014] studies of outflows, both through straits [Spall and Price, 1998] and from rivers [Beardsley et al., 1985].

Outflows may also be surface-advected or bottom-attached, with the Hudson Bay, Connecticut River, Chesapeake Bay outflow and Mississippi River plumes being examples of surface-advected outflows and the Rhine and Long Island Sound being bottom-attached outflows [Horner-Devine et al., 2015]. A number of factors such as variable outflow strength, ambient currents, tides, wind forcing and a range of processes responsible for mixing may have significant effects on the dynamics of an outflow. The extent of the source of a coastal current can be anything from highly focused river outflows to extremely broad, almost continuous sources such as along the Greenland coast [Chapman and Beardsley, 1989]. In chapters 4 and 5, surface-advected, low Rossby number outflows are considered over the full range of Kelvin numbers and source width and velocity profiles with the effects of variable source strength, ambient currents, tides and winds also analysed. In particular, observations of the Chesapeake Bay outflow are used as a typical example to test and compare to a number of the results.

The dynamical complexity of coastal outflows has led to theoretical investigations typically focussing on one particular aspect or area of the flow in isolation and developing scalings or qualitative representations of the dynamics. A number of works have considered steady coastal currents with constant width. For example the two-dimensional alongshore velocity and depth profiles of a rotating gravity current in a channel have been derived [Hacker and Linden, 2002, Martin and Lane-Serff, 2005, Martin et al., 2005]. In experiments the scalings of steady, geostrophic, constant width coastal currents typically match well to the results [Avicola and Huq, 2002, Davies et al., 1993, Lentz and Helfrich, 2002, Thomas and Linden, 2007].

Kubokawa [1991] considered the formation of steady constant width currents in an outflow with a flux of zero potential vorticity fluid from the left hand side of the source and a flux of negative quasigeostrophic potential vorticity fluid from the right hand side of the source in a quasigeostrophic $1\frac{1}{2}$-layer model representing the outflow from the Tsugaru strait, similar to the approach here. He showed that steady

solutions do not always exist, in which case a bulge of outflow fluid confined near the source must grow. McCreary et al. [1997] performed simulations in a fully nonlinear $1\frac{1}{2}$-layer model with entrainment and horizontally varying salinity, for both low and moderate Rossby numbers. For low Rossby number the results of this more complex model supported those of the simpler Kubokawa model.

It is important to understand where and when these steady constant width currents will form and how they will attach to unsteady or variable width parts of the flow by considering the full dynamics of the outflow. Johnson and McDonald [2006] considered an outflow of vortical fluid in the rigid-lid limit of the quasigeostrophic model (i.e. for zero Kelvin number), and derived an analytical expression for the steady profile and velocity field, showing how the downstream constant width current joined to a variable width steady current near the source and an unsteady head downstream.

Other theoretical approaches have included conceptual models for the influence of winds on a river plume [Fong and Geyer, 2001, Lentz, 2004] or, for inertial outflows, modelling the bulge as a circular eddy with bottom 'clipped' by the wall [Nof, 1988]. This clipped circle method appears to closely resemble bulges observed in laboratory [Avicola and Huq, 2003] and numerical [Chen, 2014] experiments for moderate Rossby number and has been used to diagnose the fraction of downstream transport in these experiments as a function of the 'impact angle' of the outer bulge current, represented as a baroclinic jet, based on the theory of Whitehead [1985].

Another approach is to integrate the momentum equations over a control volume to deduce properties of the flow [Nof, 1988, 2005, Nof and Pichevin, 2001, Nof et al., 2002, Pichevin and Nof, 1997]. Applying this technique, Pichevin and Nof [1997] deduced that steady rightward turning currents cannot conserve momentum and so are impossible: the so-called momentum imbalance paradox. To resolve this paradox they suggest that the flow must be unsteady and either periodically produce westward propagating eddies for a northward oriented outflow on a β-plane or have an indefinitely growing bulge near the source for non-northward outflows or those on an f-plane. The significant implication of these results is that buoyancy and the Coriolis force are not sufficient to explain observations of steady rightward currents in the oceans and in experiments as previously thought. Instead, some other effect,

such as an angled outflow, alongshore currents or winds, must provide the momentum flux to turn the current in each one of these cases.

The approach of chapters 4 and 5 is to develop and apply a model of outflows which captures the key dynamics yet is simple enough to easily interpret and to enable full mathematical analysis. It is hoped that a complete understanding of this simple model can be used as a base to expand on and to contextualise the results of more sophisticated studies. The dynamics are analysed in full before further effects and complexity are introduced. It will be seen that this model actually represents many aspects of outflows very well. Considering the full spatial and temporal dynamics of the whole outflow shows when and where certain features will be formed. For example, it will be seen that there are situations in which steady solutions exist but are never realised by an evolving flow upon initiation of the source. Analysing the momentum fluxes in the model highlights the resolution to the momentum imbalance paradox [Pichevin and Nof, 1997].

The outflow is considered in a quasigeostrophic $1\frac{1}{2}$-layer model which aims to capture the key dynamics: the rotation modified source velocity and the generation of vorticity as the buoyant outflow adjusts. Although this model makes many simplifications it is able to explore the effects of important factors affecting river plumes such as variable source outflow, ambient currents, tides and winds. The strength of the model is its simplicity. This enables analytical solutions to be found for the profile of the outflow and velocity field over time in many cases. These analytical solutions are derived for the primary problem of a constant strength outflow in chapter 4. In chapter 5, this theory is discussed in an oceanographic context using the analytical solutions, along with numerical simulations to build a detailed understanding of the dynamics of quasigeostrophic outflows.

1.3 Quasigeostrophic flow

The flows considered here are shallow, with horizontal lengthscales of tens of kilometres and timescales of days or weeks. The flow is thus modelled as a $1\frac{1}{2}$-layer quasigeostrophic (QG) flow with an active layer of interest, and passive layers above or below, depending on the scenario under consideration. This section begins by

outlining the key equations of interest for this thesis before giving a full derivation of the governing equations for $1\frac{1}{2}$-layer quasigeostrophic flow. The outline of the main equation should be a sufficient introduction to the work in the body of the thesis. The additional derivation of $1\frac{1}{2}$-layer quasigeostrophic flow is quite standard, but is reproduced here for completeness and because some of the details, for example the asymptotic derivation of QG from the nondimensional rotating shallow water equations, are required later in the thesis. Also, the derivation given here is slightly more general than those usually presented, in that it considers an active layer with passive layers both above and below, which would apply to, for example, the California Undercurrent [Molemaker et al., 2015]. The standard simpler case of a single passive layer (either above or below) is then contained as a sub-case within this model.

1.3.1 Governing equations

The non-dimensional surface perturbation η is a streamfunction for the two-dimensional flow and so the fluid velocity $\boldsymbol{u} = (u, v)$ is given by

$$\boldsymbol{u} = \left(-\frac{\partial \eta}{\partial y}, \frac{\partial \eta}{\partial x} \right), \tag{1.1}$$

where $\boldsymbol{x} = (x, y)$ are the horizontal spatial coordinates. The potential vorticity (PV) $q = \nabla^2 \eta - \eta / a^2$ is conserved following the fluid motion so

$$\frac{\mathrm{D}}{\mathrm{D}t} \left(\nabla^2 \eta - \frac{1}{a^2} \eta \right) = 0 \tag{1.2}$$

where a is the ratio of the Rossby radius of deformation L_R to the lengthscale for the flow L and $\mathrm{D}/\mathrm{D}t = \partial/\partial t + (\boldsymbol{u} \cdot \boldsymbol{\nabla})$ is the material derivative. The Rossby radius of deformation, or simply "Rossby radius", is given by $L_\mathrm{R} = \sqrt{g' D}/f$, where g' is the reduced gravity, D is the undisturbed layer depth and f is the Coriolis parameter.

The parameter $a = L/L_\mathrm{R}$, the reciprocal of the Kelvin number, is the ratio of the Rossby radius L_R to the lengthscale L of the flow and is of key importance in this thesis. It gives the non-dimensional lengthscale over which perturbations to the free surface decay. Intuitively it gives a lengthscale for how far away effects will be 'felt'. Taking the case of a point vortex, far from the vortex the fluid velocity will decay

like $\exp(-r/a)$ if r is the distance to the vortex centre.

The limit $a \to \infty$ is known as the 'rigid-lid limit' as it is equivalent to the case where solid boundaries hold the free-surfaces flat. In this limit the PV is simply the relative vorticity $\nabla^2\eta$. This is a simpler case and, due to the conformal invariance of Laplace's equation, allows powerful techniques such as conformal mapping to be used to construct solutions analytically which aren't available in the corresponding problem for QG flow.

This thesis considers two main alternatives for the PV distribution: piecewise constant distributions of PV and PV which is identically zero apart from a finite number of singularities (point vortices).

1.3.2 Point vortex motion

Consider the case where the PV is zero throughout the flow except at the locations $\boldsymbol{x}_i(t)$ of a finite number of point vortices with strengths $\Gamma_i(t)$, giving the nondimensional equation for the streamfunction

$$\nabla^2\eta - \frac{1}{a^2}\eta = \sum_{i=1}^{m} \Gamma_i(t)\delta(\boldsymbol{x} - \boldsymbol{x}_i(t)) \tag{1.3}$$

at each instant, where t is time, and m is the number of point vortices. This two-dimensional partial differential equation (PDE) is an inhomogeneous modified Helmholtz equation.

The model is closed by inverting eq. (1.3) at each time to obtain η and hence the velocity field $\boldsymbol{u}$ from eq. (1.1). The precise solution depends on the the geometry of the flow field and the background flow determined by the boundary conditions. Subsequent sections discuss various forms of these boundary conditions and geometries in different oceanographic scenarios.

The propagation velocity of a vortex can be found from the non-singular part of the streamfunction

$$\widetilde{\eta}_i = \eta + \frac{\Gamma_i}{2\pi} K_0\left(\frac{|\boldsymbol{x} - \boldsymbol{x}_i|}{a}\right), \tag{1.4}$$

where K_n is the modified Bessel function of the second kind of order n, the open-domain Green's function for the modified Helmholtz operator. The tilde and sub-

script i notation denotes that this is the streamfunction felt by the i^{th} vortex. The velocity of a constant circulation vortex is then given by

$$\dot{\boldsymbol{x}}_i = \widetilde{\boldsymbol{u}}_i = \lim_{\boldsymbol{x}\to\boldsymbol{x}_i} \left(-\frac{\partial \widetilde{\eta}_i}{\partial y}, \frac{\partial \widetilde{\eta}_i}{\partial x} \right). \tag{1.5}$$

1.3.3 Piecewise constant potential vorticity

For piecewise constant distributions of PV the domain of interest is partitioned into a finite number of material sub-domains $\mathcal{D}_i$ which move with the fluid and have PV values Π_i giving

$$\nabla^2 \eta - \frac{1}{a^2}\eta = \Pi_i, \qquad \boldsymbol{x} \in \mathcal{D}_i, \tag{1.6}$$

as the equation for the streamfunction η. As the PV distribution is piecewise constant, given the initial distribution of PV $\mathcal{D}_i$ and Π_i, the evolution of the boundaries of the domains $\partial\mathcal{D}_i$ can be efficiently numerically computed with the method of contour dynamics with surgery [Dritschel, 1988].

1.3.4 The quasigeostrophic model - derivation

This section gives a full derivation of the $1\frac{1}{2}$-layer quasigeostrophic flow model. Take Cartesian axes $\mathcal{O}xyz$ with unit vectors $\boldsymbol{i}$, $\boldsymbol{j}$ and $\boldsymbol{k}$, where $\boldsymbol{k}$ points outward, normal to the Earth's surface. For oceanic flows the Reynolds number is very high and the Mach number very low. Therefore, assuming our flow is inviscid and incompressible, conservation of mass and momentum give the rotating Euler equations

$$\boldsymbol{\nabla} \cdot \boldsymbol{u} = 0, \tag{1.7}$$

$$\frac{\mathrm{D}\boldsymbol{u}}{\mathrm{D}t} + 2\boldsymbol{\Omega} \wedge \boldsymbol{u} = -\frac{1}{\rho}\nabla p - g\boldsymbol{k}, \tag{1.8}$$

where $\boldsymbol{u} = (u, v, w)$, ρ and p are the fluid velocity, density and pressure, $\boldsymbol{\Omega} = (\Omega_x, \Omega_y, \Omega_z)$ is the angular rotation vector, g is the gravitational acceleration and $\mathrm{D}/\mathrm{D}t$ is the material derivative defined as

$$\frac{\mathrm{D}}{\mathrm{D}t} = \frac{\partial}{\partial t} + \boldsymbol{u} \cdot \boldsymbol{\nabla}. \tag{1.9}$$

1.3.4.1 The rotating shallow water equations

Oceanic flows are typically shallow, with vertical lengthscales of tens to hundreds of metres and horizontal lengthscales of tens to hundreds of kilometres. Therefore let δ be the ratio of the typical vertical lengthscale to the typical horizontal lengthscale and rescale z and w by $\delta \ll 1$ giving $z = \delta z'$ and $w = \delta w'$ where z' and w' are $\mathcal{O}(1)$ variables. With this rescaling, and splitting the pressure into its hydrostatic and non-hydrostatic parts $p = p_0(x, y, z, t) - \rho g z$, the component form of (1.8) is

$$\frac{\partial u}{\partial t} + u\frac{\partial u}{\partial x} + v\frac{\partial u}{\partial y} + w'\frac{\partial u}{\partial z'} + 2(\delta\Omega_x w' - \Omega_z v) = -\frac{1}{\rho}\frac{\partial p_0}{\partial x}, \tag{1.10a}$$

$$\frac{\partial v}{\partial t} + u\frac{\partial v}{\partial x} + v\frac{\partial v}{\partial y} + w'\frac{\partial v}{\partial z'} + 2(\Omega_z u - \delta\Omega_x w') = -\frac{1}{\rho}\frac{\partial p_0}{\partial y}, \tag{1.10b}$$

$$\delta\left(\frac{\partial w'}{\partial t} + u\frac{\partial w'}{\partial x} + v\frac{\partial w'}{\partial y} + w'\frac{\partial w'}{\partial z'}\right) + 2(\Omega_x v - \Omega_y u) = -\frac{1}{\delta}\frac{1}{\rho}\frac{\partial p_0}{\partial z'}. \tag{1.10c}$$

The leading order terms in which are

$$\frac{\partial u}{\partial t} + u\frac{\partial u}{\partial x} + v\frac{\partial u}{\partial y} + w'\frac{\partial u}{\partial z'} - 2\Omega_z v = -\frac{1}{\rho}\frac{\partial p_0}{\partial x}, \tag{1.11a}$$

$$\frac{\partial v}{\partial t} + u\frac{\partial v}{\partial x} + v\frac{\partial v}{\partial y} + w'\frac{\partial v}{\partial z'} + 2\Omega_z u = -\frac{1}{\rho}\frac{\partial p_0}{\partial y}, \tag{1.11b}$$

$$0 = -\frac{1}{\delta}\frac{1}{\rho}\frac{\partial p_0}{\partial z'}. \tag{1.11c}$$

From these equations, with the shallow water approximation made, it can be seen that only the vertical component of the angular rotation vector is dynamically important: the traditional approximation. Equation (1.11c) shows that the horizontal pressure gradient is independent of z, i.e.

$$p = p_0(x, y, t) - \rho g z, \tag{1.12}$$

and cannot introduce vertical variation in the horizontal velocity. The system is therefore effectively two-dimensional with $u = u(x, y)$ and $v = v(x, y)$ so (1.11a) and

(1.11b) become

$$\frac{\mathrm{D}u}{\mathrm{D}t} - fv = -\frac{1}{\rho}\frac{\partial p_0}{\partial x}, \tag{1.13a}$$

$$\frac{\mathrm{D}v}{\mathrm{D}t} + fu = -\frac{1}{\rho}\frac{\partial p_0}{\partial y}, \tag{1.13b}$$

where $\mathrm{D}/\mathrm{D}t$ is, from here onward, the two-dimensional material derivative

$$\frac{\mathrm{D}}{\mathrm{D}t} = \frac{\partial}{\partial t} + u\frac{\partial}{\partial x} + v\frac{\partial}{\partial y}, \tag{1.14}$$

and the Coriolis parameter f is given by

$$f = 2\Omega_z = 2\|\boldsymbol{\Omega}\| \sin\lambda, \tag{1.15}$$

and varies with the latitude λ. However, over distances of less than many hundred kilometres, as considered in this work, the variation of λ is small and f may be taken to be constant: the f-plane approximation.

As the horizontal velocities are independent of height, (1.7) may be integrated with respect to z to giving

$$[w]_{z=h_\mathrm{l}}^{z=h_\mathrm{u}} = -H\left(\frac{\partial u}{\partial x} + \frac{\partial v}{\partial y}\right), \tag{1.16}$$

where h_l and h_u are the heights of the lower and upper material boundaries of the fluid under consideration and $H = h_\mathrm{u} - h_\mathrm{l}$. The kinematic boundary condition shows that, on a material surface $z = h(x, y)$

$$w(z = h) = \frac{\mathrm{D}h}{\mathrm{D}t}. \tag{1.17}$$

Substituting this into (1.16) gives

$$\frac{\mathrm{D}H}{\mathrm{D}t} = -H\boldsymbol{\nabla} \cdot \boldsymbol{u}, \tag{1.18}$$

where, from here onward, $\boldsymbol{\nabla}$ is the two-dimensional divergence

$$\boldsymbol{\nabla} = \left(\frac{\partial}{\partial x}, \frac{\partial}{\partial y} \right). \tag{1.19}$$

Equation (1.18), along with (1.13a), (1.13b) and the hydrostatic pressure (1.12) form the rotating shallow water equations. In vector format they are

$$\frac{\mathrm{D}H}{\mathrm{D}t} + H\boldsymbol{\nabla} \cdot \boldsymbol{u} = 0, \tag{1.20a}$$

$$\frac{\mathrm{D}\boldsymbol{u}}{\mathrm{D}t} + f\boldsymbol{k} \wedge \boldsymbol{u} = -\frac{1}{\rho}\boldsymbol{\nabla} p_0, \tag{1.20b}$$

$$p = p_0(x, y) - \rho g z. \tag{1.20c}$$

The function p_0 is determined by the dynamic boundary condition that the pressure must be continuous across the upper surface of the fluid.

1.3.4.2 $1\frac{1}{2}$-layer model

The scenarios considered in this work all consist of intense vortical features in a constant density, relatively thinner active layer with quiescent, constant (but different) density, relatively thicker layers either above or below. The two cases of surface or bottom active layers lead to the same equations (for a flat sea bed) and are contained within the more general case of quiescent layers both above and below the active layer. Let the active layer have density and pressure ρ and p and the upper and lower quiescent layers have density and pressures ρ_u, ρ_l, p_u and p_l respectively. As the upper and lower layers are far deeper than the active layer and therefore relatively quiescent there must be no horizontal pressure gradient so p_u and p_l are functions purely of z.

Taking, without loss of generality, the pressure in the upper quiescent layer to be $p_\mathrm{u} = -\rho_\mathrm{u} g z$, the dynamic boundary condition at the top of the active layer gives the active layer pressure as

$$p = (\rho - \rho_\mathrm{u}) g h_\mathrm{u} - \rho g z. \tag{1.21}$$

The dynamic boundary condition at the bottom of the active layer then gives the

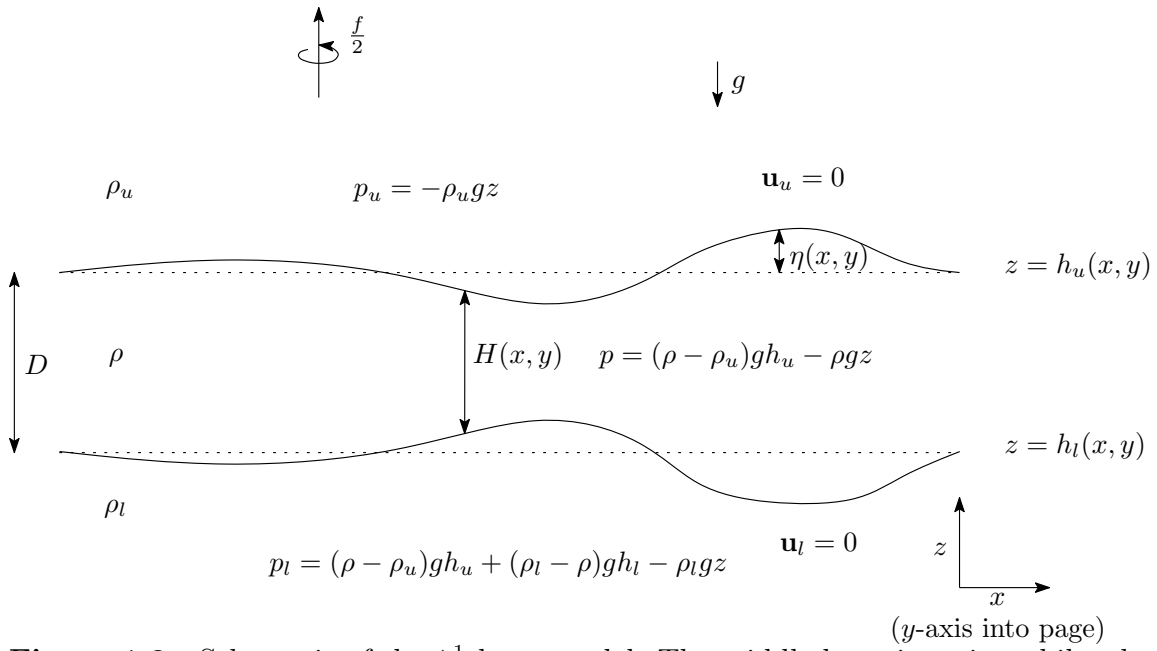

Figure 1.2: Schematic of the $1\frac{1}{2}$-layer model. The middle layer is active whilst the upper and lower layers are quiescent. Taking $\rho_u = 0$ (or $\rho_l \to \infty$) gives a surface (or bottom) active layer with a single quiescent layer below (or above).

lower quiescent layer pressure as

$$p_\mathrm{l} = (\rho - \rho_\mathrm{u}) g h_\mathrm{u} + (\rho_\mathrm{l} - \rho) g h_\mathrm{l} - \rho_\mathrm{l} g z. \tag{1.22}$$

For this lower layer to be quiescent, p_l must be independent of x and y, meaning that

$$(\rho - \rho_\mathrm{u}) g h_\mathrm{u} + (\rho_\mathrm{l} - \rho) g h_\mathrm{l} = \text{constant}, \tag{1.23}$$

and therefore giving the relationship between the upper and lower layer depths

$$h_\mathrm{l} = -\frac{\rho - \rho_\mathrm{u}}{\rho_\mathrm{l} - \rho} h_\mathrm{u} + \text{constant}, \tag{1.24}$$

where D is the undisturbed layer depth. The active layer depth can therefore be given in terms of just the upper surface height as

$$H = \frac{\rho_\mathrm{l} - \rho_\mathrm{u}}{\rho_\mathrm{l} - \rho} h_\mathrm{u} + \text{constant}, \tag{1.25}$$

or rewritten as

$$H = \frac{\rho_\mathrm{l} - \rho_\mathrm{u}}{\rho_\mathrm{l} - \rho} \eta + D, \tag{1.26}$$

where D is the undisturbed layer depth and η is the perturbation to the undisturbed depth of the upper surface i.e. $h_{\mathrm{u}} = \eta + \text{constant}$.

Taking $\rho_{\mathrm{u}} = 0$ represents an upper active layer above a denser quiescent layer with dynamically insignificant air above. Taking $\rho_{\mathrm{l}} \to \infty$ gives a model of an upper quiescent layer with a bottom active layer above a flat, solid bottom. Thus, this models enables three different situations of interest to be investigated: surface currents, undercurrents at mid-depth and dense bottom currents. The dynamics of these three situations are similar, with the situation of interest simply determining parameter values.

Substituting (1.26) and (1.21) into (1.20) gives the rotating shallow water equations for the $1\frac{1}{2}$-layer model

$$\frac{\mathrm{D}\eta}{\mathrm{D}t} + (c_1 D + \eta)\boldsymbol{\nabla} \cdot \boldsymbol{u} = 0, \tag{1.27a}$$

$$\frac{\mathrm{D}\boldsymbol{u}}{\mathrm{D}t} + f\boldsymbol{k} \wedge \boldsymbol{u} = -c_2 g \boldsymbol{\nabla}\eta, \tag{1.27b}$$

where $c_1 = (\rho_{\mathrm{l}} - \rho)/(\rho_{\mathrm{l}} - \rho_{\mathrm{u}})$ and $c_2 = (\rho - \rho_{\mathrm{u}})/\rho$.

1.3.4.3 The quasigeostrophic scaling

Consider the size of the terms in (1.20). Non-dimensionalising the equations with typical length, time, velocity and surface perturbation scales L, T, U and $[\eta]$ gives

$$\frac{[\eta]}{T}\frac{\partial \eta}{\partial t} + \frac{U[\eta]}{L}(\boldsymbol{u} \cdot \boldsymbol{\nabla})\eta + \frac{U}{L}(c_1 D + [\eta]\eta)\boldsymbol{\nabla} \cdot \boldsymbol{u} = 0, \tag{1.28a}$$

$$\frac{U}{T}\frac{\partial \boldsymbol{u}}{\partial t} + \frac{U^2}{L}(\boldsymbol{u} \cdot \boldsymbol{\nabla})\boldsymbol{u} + fU\boldsymbol{k} \wedge \boldsymbol{u} = -\frac{c_2 g[\eta]}{L}\boldsymbol{\nabla}\eta, \tag{1.28b}$$

where all variables are now non-dimensional. Rearranging (1.28b) gives

$$\varepsilon\frac{L}{TU}\frac{\partial \boldsymbol{u}}{\partial t} + \varepsilon(\boldsymbol{u} \cdot \boldsymbol{\nabla})\boldsymbol{u} + \boldsymbol{k} \wedge \boldsymbol{u} = -\frac{c_2 g[\eta]}{fUL}\boldsymbol{\nabla}\eta, \tag{1.29}$$

where $\varepsilon = U/Lf$ is the Rossby number, the non-dimensional number giving the ratio of the inertial to Coriolis terms. In the oceanic scenarios considered here, the Rossby number is small and the Coriolis acceleration dominates over the inertial forces. This work examines flows over the advective timescale so take $T = L/U$. This

choice, combined with the small Rossby number, filters out the relatively fast Kelvin and Poincaré waves and focusses on the longer timescale, adjusted motions. With this scaling and a small Rossby number ε it is clear from (1.29) that the dominant balance, known as geostrophic balance, is between the Coriolis acceleration and the horizontal pressure gradient. Therefore the appropriate scaling for the upper surface perturbation is $[\eta] = fUL/c_2 g$. Using this scaling, the advective timescale and rearranging gives the non-dimensional rotating shallow water equations.

$$\varepsilon \frac{\mathrm{D}\eta}{\mathrm{D}t} + (a^2 + \varepsilon\eta)\boldsymbol{\nabla} \cdot \boldsymbol{u} = 0, \tag{1.30a}$$

$$\varepsilon \frac{\mathrm{D}\boldsymbol{u}}{\mathrm{D}t} + \boldsymbol{k} \wedge \boldsymbol{u} = -\boldsymbol{\nabla}\eta, \tag{1.30b}$$

where $a = L_\mathrm{R}/L$ is the ratio of Rossby radius of deformation $L_\mathrm{R} = \sqrt{g'D}/f$ to the horizontal lengthscale, for the three-layer analogue of the reduced gravity

$$g' = \frac{(\rho_\mathrm{l} - \rho)(\rho - \rho_\mathrm{u})}{(\rho_\mathrm{l} - \rho_\mathrm{u})\rho} g, \tag{1.31}$$

which reduces to the usual two-layer expressions for reduced gravity by taking either $\rho_\mathrm{u} = 0$ or $\rho_\mathrm{l} \to \infty$, and will be simply referred to as the reduced gravity. In the case with $\rho_\mathrm{u} = 0$, the upper surface deformation will be much smaller than, but still proportional to, the lower surface deformation. The non-dimensional Rossby radius of deformation a will be referred to simply as the Rossby radius subsequently and is one of the key parameters of interest in this work.

As the Rossby number ε is small, take an asymptotic expansion of the form $\eta = \eta_0 + \epsilon\eta_1 + \cdots$, $\boldsymbol{u} = \boldsymbol{u}_0 + \varepsilon\boldsymbol{u}_1 + \cdots$. At leading order this gives

$$\boldsymbol{u}_0 = -\boldsymbol{\nabla} \wedge (\eta_0 \boldsymbol{k}), \tag{1.32}$$

and at $\mathcal{O}(\varepsilon)$

$$\frac{1}{a^2}\frac{\mathrm{D}_0\eta_0}{\mathrm{D}_0 t} + \boldsymbol{\nabla} \cdot \boldsymbol{u}_1 = 0, \tag{1.33a}$$

$$\frac{\mathrm{D}_0\boldsymbol{u}_0}{\mathrm{D}_0 t} + \boldsymbol{k} \wedge \boldsymbol{u}_1 = -\boldsymbol{\nabla}\eta_1, \tag{1.33b}$$

where $\mathrm{D}_0/\mathrm{D}_0 t = \partial/\partial t + (\boldsymbol{u}_0 \cdot \boldsymbol{\nabla})$. Equation (1.32) shows that the flow is in geostrophic

balance and that the leading order surface deformation η_0 is a streamfunction for the flow. Taking the curl of (1.33b) and substituting in (1.33a) gives

$$\frac{\mathrm{D}_0}{\mathrm{D}_0 t}\left(\nabla^2\eta_0 - \frac{1}{a^2}\eta_0\right) = 0. \tag{1.34}$$

Equation (1.34) shows that the potential vorticity $q_0 = \nabla^2\eta_0 - \eta_0/a^2$ is conserved following the leading order flow. From here onward, unless specifically stated, only the leading order flow will be considered and the subscript 0 notation will be dropped. Thus the equations governing quasigeostrophic flow (1.1) and (1.2),

$$\boldsymbol{u} = -\boldsymbol{\nabla} \wedge (\eta \boldsymbol{k}), \tag{1.35a}$$

$$\frac{\mathrm{D}}{\mathrm{D}t}\left(\nabla^2\eta - \frac{1}{a^2}\eta\right) = 0, \tag{1.35b}$$

have been derived.

Chapter 2

The quasigeostrophic Brown–Michael model

In this chapter a simple model for the formation of ocean eddies by flow separation from sharply curved horizontal boundary topography is developed. This is based on the Brown and Michael [1954] model for two-dimensional vortex shedding, which is adapted to more realistically model mesoscale oceanic flow by including a deforming free surface. With a free surface, the streamfunction for the flow is not harmonic so the conformal mapping methods used in the standard Brown–Michael approach cannot be used and the problem must be solved numerically. A numerical scheme is developed based on a Chebyshev spectral method for the streamfunction partial differential equation (PDE) and a second order implicit timestepping scheme for the vortex position ordinary differential equations (ODEs). This method is used to compute shed vortex trajectories for three background flows: (A) a steady flow around a semi-infinite plate, (B) a free vortex moving around a semi-infinite plate and (C) a free vortex moving around a right-angled wedge. In (A), the inclusion of surface deformation dramatically slows the vortex and changes its trajectory from a straight path to a curved one. In (B) and (C), without the inclusion of flow separation, free vortices traverse fully around the tip along symmetrical trajectories. With the effects of flow separation included, very different trajectories are found: for all values of the model parameter—the Rossby radius—the free and shed vortices pair up and move off to infinity without passing around the tip. Their final propagation angle depends strongly and monotonically on the Rossby radius.

2.1 Introduction

A simple approach modelling the formation of vortices by flow separation is the Brown and Michael [1954] model. Brown and Michael refined calculations of lift on an aeroplane delta wing by including the lift generated by the vortex sheet shed from the trailing edge. Their model replaces the spiral vortex sheet—both the shape and strength of which must be determined—by a single point vortex of variable circulation. This key step simplifies the problem dramatically from solving PDEs governing the vortex sheet evolution, which may have issues of ill-posedness and instability at arbitrarily small wavelengths and so require regularisation [Krasny, 1986]. The point vortex formulation inevitably leaves a pressure discontinuity across a branch cut connecting the vortex to the separation point, which is interpreted as being the infinitesimal connecting sheet along which vorticity is fed to the shed vortex. Brown and Michael derived a new equation of motion for the vortex—the Brown–Michael equation— which ensured the net force, on the cut and vortex combined, was zero.

Here, aiming to improve oceanic flow models, a new version of the Brown–Michael equation for QG flow is derived in section 2.2. With QG flow, complex variable methods enabling construction of the vortex Hamiltonian in conformally mapped domains are no longer available, so instead numerical techniques will be employed. In section 2.3 a numerical scheme based on a Chebyshev spectral method to solve the PDE for the streamfunction and a second order implicit scheme to integrate the Brown–Michael coupled ODEs is developed. In section 2.4 this method is applied to three background flows: (A) a steady flow around a semi-infinite plate, (B) a free vortex moving around a semi-infinite plate and (C) a free vortex moving around a right-angled wedge.

2.2 Derivation of a quasigeostrophic Brown–Michael equation

In the Brown–Michael model, the spiral vortex sheet formed from a separated flow is modelled by a single point vortex of variable circulation. The circulation of the shed vortex is set to ensure no velocity singularity at the separation point. This is known as the Kutta condition. However the model has the problem that, due to the varying circulation, there is an unphysical pressure discontinuity along some line (a branch cut) connecting the vortex to the separation point. Brown and Michael's solution to this problem is to require that the vortex move relative to the fluid around it, so that it experiences a lift force which cancels out the net force on the vortex and cut combined. Here this model will be adapted for QG flow using a new derivation based on the streamfunction instead of the complex potential.

2.2.1 Quasigeostrophic flow

As in the introduction, consider a shallow layer of fluid in a rotating reference frame with non-dimensional free surface deviation η. The asymptotic expansion of the non-dimensional rotating shallow water equations

$$\varepsilon\frac{\mathrm{D}\boldsymbol{u}}{\mathrm{D}t}+\boldsymbol{k}\wedge\boldsymbol{u}=-\nabla\eta, \tag{2.1a}$$

$$\varepsilon\frac{\mathrm{D}\eta}{\mathrm{D}t}+\left(a^2+\varepsilon\eta\right)\nabla\cdot\boldsymbol{u}=0, \tag{2.1b}$$

for small Rossby number ε, is reproduced here for convenience. These are equations in the (x,y)-plane where $\boldsymbol{u}$ is the horizontal velocity, $\boldsymbol{k}$ is the unit vector in the z-direction and $a=L_\mathrm{R}/L$ is the ratio of the Rossby radius $L_\mathrm{R}=\sqrt{g'D}/f$ (for reduced gravity g', typical fluid depth D and Coriolis parameter f) to the typical horizontal lengthscale L. An asymptotic expansion of the form $\eta=\eta_0+\epsilon\eta_1+\cdots$, $\boldsymbol{u}=\boldsymbol{u}_0+\epsilon\boldsymbol{u}_1+\cdots$ gives at leading order

$$\boldsymbol{u}_0=-\nabla\wedge(\eta_0\boldsymbol{k}), \tag{2.2}$$

and at $\mathcal{O}(\varepsilon)$

$$\frac{\mathrm{D}_0\boldsymbol{u_0}}{\mathrm{D}_0 t} + \boldsymbol{k} \wedge \boldsymbol{u}_1 = -\nabla\eta_1, \tag{2.3a}$$

$$\frac{1}{a^2}\frac{\mathrm{D}_0\eta_0}{\mathrm{D}_0 t} + \nabla \cdot \boldsymbol{u}_1 = 0, \tag{2.3b}$$

where $\mathrm{D}_0/\mathrm{D}_0 t = \partial/\partial t + (\boldsymbol{u}_0 \cdot \nabla)$. Taking the curl of (2.3a) and substituting in (2.3b) gives

$$\frac{\mathrm{D}_0}{\mathrm{D}_0 t}\left(\nabla^2\eta_0 - \frac{1}{a^2}\eta_0\right) = 0, \tag{2.4}$$

showing that the potential vorticity $q_0 = \nabla^2\eta_0 - \eta_0/a^2$ is conserved following the leading order flow. In the situations considered here any topography extends vertically throughout the entire fluid depth and the flow is initially irrotational so $q_0 = 0$, except at the positions of any point vortices which give delta function singularities of potential vorticity. That is, for a point vortex of strength Γ at position $\boldsymbol{x}_\mathrm{v}$,

$$\nabla^2\eta_0 - \frac{1}{a^2}\eta_0 = \Gamma\delta(\boldsymbol{x} - \boldsymbol{x}_\mathrm{v}). \tag{2.5}$$

2.2.2 The Brown–Michael correction

Consider a point vortex of time dependent circulation $\Gamma = \Gamma(t)$ at the origin. At leading-order the streamfunction satisfies (2.5) and is given by $\eta_0 = (-\Gamma/2\pi)K_0(r/a)$, where K_n is the modified Bessel function of the second kind of order n, and (r, θ) are polar coordinates with unit vectors $\hat{\boldsymbol{e}}_r$ and $\hat{\boldsymbol{e}}_\theta$. As the flow around the vortex is purely azimuthal, $\boldsymbol{u}_0 = u_{0\theta}\hat{\boldsymbol{e}}_\theta$ and $\boldsymbol{u}_1 = u_{1\theta}\hat{\boldsymbol{e}}_\theta$, so the azimuthal component of (2.3a) is

$$\frac{\partial u_{0\theta}}{\partial t} = -\frac{1}{r}\frac{\partial\eta_1}{\partial\theta}, \tag{2.6}$$

where subscript r or θ denotes the component of a vector in the radial or azimuthal directions respectively. The leading order azimuthal velocity is given by $u_{0\theta} = \partial\eta_0/\partial r = \Gamma/(2\pi a)K_1(r/a)$, as $K_0' = -K_1$. Substituting this into (2.6) and integrating with respect to θ gives

$$\eta_1 = -\frac{\dot{\Gamma}}{2\pi}\frac{r}{a}K_1\left(\frac{r}{a}\right)\theta + \hat{\eta}(r) \tag{2.7}$$

for some function $\hat{\eta}(r)$, where the dot denotes a time derivative. Therefore there is an $\mathcal{O}(\varepsilon)$ pressure discontinuity of size $(\dot{\Gamma}r/a)K_1(r/a)$ across some branch cut. In the rigid-lid problem considered by Brown and Michael, the pressure discontinuity was constant along the cut so the net force on the cut was independent of the cut shape. For quasigeostrophic dynamics this is not the case and the net force on the cut does depend on its shape. Here a straight line connecting the vortex to the separation point is used for the cut shape since, because the magnitude of the pressure discontinuity along the cut is a function only of the distance to the vortex, this minimises the total force exerted on the cut. Calculations using cuts with large perturbations of symmetric quadratic shape and maximum displacement as large as half of the cut length have been performed. These give net forces with less than a tenth maximum difference in magnitude and vortex trajectories with less than 4% difference in position. It is also worth noting that this correction term is not the main effect in the dynamics of the problem. In the original rigid-lid Brown–Michael problem the effect of the correction term is to reduce the shed vortex speed by a third and it has no effect on the final shape of the trajectory. With a linear cut and in the frame with the separation point at the origin and the shed vortex at $\boldsymbol{x}_\mathrm{s}$, the net $\mathcal{O}(\varepsilon)$ force on the cut is

$$\boldsymbol{F}_\mathrm{net} = -\dot{\Gamma} \int_0^{|\boldsymbol{x}_\mathrm{s}|} \frac{r}{a} K_1\left(\frac{r}{a}\right) \mathrm{d}r \, \boldsymbol{n} \tag{2.8}$$

where $\boldsymbol{n} = (\boldsymbol{k} \wedge \boldsymbol{x}_\mathrm{s})/|\boldsymbol{x}_\mathrm{s}|$ is the unit normal to the cut.

The Brown–Michael model requires the vortex to move such that its lift cancels the net pressure discontinuity. Treating the vortex as a cylinder with infinitesimal radius (equivalent to the rigid-lid limit), the Kutta–Joukowski lift theorem [Batchelor, 1967] shows that a vortex moving at velocity $\dot{\boldsymbol{x}}_\mathrm{s}$ in a flow with velocity $\widetilde{\boldsymbol{u}}_\mathrm{s}$ experiences the $\mathcal{O}(\varepsilon)$ lift force

$$\boldsymbol{F}_\mathrm{lift} = \Gamma \boldsymbol{k} \wedge (\widetilde{\boldsymbol{u}}_\mathrm{s}(\boldsymbol{x}_\mathrm{s}) - \dot{\boldsymbol{x}}_\mathrm{s}) \,. \tag{2.9}$$

$\widetilde{\boldsymbol{u}}_\mathrm{s}(\boldsymbol{x}_\mathrm{s})$ is the velocity a 'free' vortex would have i.e. the velocity due to the background flow and the interaction of the vortex with the domain boundary, but excluding the direct contribution from the vortex itself as given by (1.5). Balancing

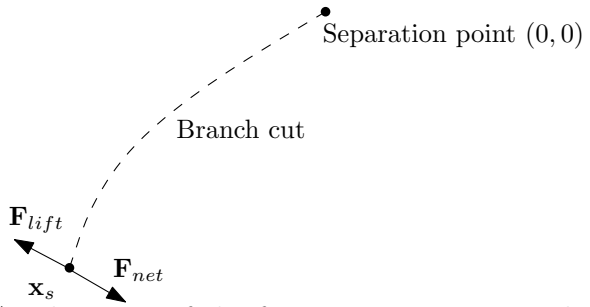

Figure 2.1: A schematic of the forces on a Brown-Michael shed vortex.

this lift force with the total pressure discontinuity, as shown in Fig. 2.1, gives the quasigeostrophic Brown–Michael (QGBM) equation

$$\dot{\boldsymbol{x}}_{\mathrm{s}} = \widetilde{\boldsymbol{u}}_{\mathrm{s}}(\boldsymbol{x}_{\mathrm{s}}) - \frac{\dot{\Gamma}}{\Gamma}\boldsymbol{x}_{\mathrm{s}}F(|\boldsymbol{x}_{\mathrm{s}}|), \tag{2.10}$$

where the function $F(s)$ is given by

$$F(s) = \frac{1}{s}\int_0^s \frac{r}{a}K_1\left(\frac{r}{a}\right)\,\mathrm{d}r. \tag{2.11}$$

This function monotonically decreases from $\lim_{s\to 0} F(s) = 1$ to $\lim_{s\to\infty} F(s) = 0$. The system is closed by the Kutta condition, which requires that the vortex circulation Γ is such that there is no velocity singularity at the separation point.

The equation of motion of a free vortex (i.e. a vortex with constant circulation) with position $\boldsymbol{x}_{\mathrm{f}}$ is

$$\dot{\boldsymbol{x}}_{\mathrm{f}} = \widetilde{\boldsymbol{u}}_{\mathrm{f}}(\boldsymbol{x}_{\mathrm{f}}). \tag{2.12}$$

This is equal to the QGBM equation (2.10) with $\dot{\Gamma} = 0$. In the rigid-lid limit $a \to \infty$, $K_1(r/a) \to a/r$, so $\lim_{s\to\infty} F(s) = \pi/2$ and the QGBM equation reduces to the original Brown–Michael equation

$$\dot{\boldsymbol{x}}_{\mathrm{s}} = \widetilde{\boldsymbol{u}}_{\mathrm{s}}(\boldsymbol{x}_{\mathrm{s}}) - \frac{\dot{\Gamma}}{\Gamma}\boldsymbol{x}_{\mathrm{s}}. \tag{2.13}$$

Here $\widetilde{\boldsymbol{u}}_{\mathrm{s}}(\boldsymbol{x}_{\mathrm{s}})$ is again the velocity a free vortex would have but now in rigid-lid flow.

From here onward, only the leading order motion will be considered so subscripts are dropped e.g. η is written for η_0. The streamfunction will be split into two components $\eta = \widetilde{\eta} + \eta_{\mathrm{v}}$ where η_{v} is the direct contribution from any vortices ignoring

boundaries and is known and $\widetilde{\eta}$ is the rest of the solution which is to be found. $\widetilde{\eta}$ has zero potential vorticity and ensures that the no flux boundary condition for η is satisfied. It satisfies the homogeneous modified Helmholtz equation

$$\nabla^2\widetilde{\eta} - \frac{1}{a^2}\widetilde{\eta} = 0. \tag{2.14}$$

2.3 Numerical scheme

2.3.1 Physical problem and numerical procedure

The physical problems considered in this chapter all feature a wedge of angle α ($0 \leq \alpha < 2\pi$) with the tip at the origin (as shown in Fig. 2.2a) and some background flow. Without shedding, and for $\alpha < \pi$, a general background flow would give a velocity singularity at the wedge tip. This is unphysical so, instead, a vortex is shed to ensure there is no velocity singularity at the tip. This shed vortex will start from the tip and move according to (2.10). Three specific examples will be considered here. The first two are for a semi-infinite plate (a wedge of angle $\alpha = 0$), first with a steady background flow (a flow with boundary condition $\eta =$ constant on the plate) and second with a free vortex as the background flow. The third example is a wedge of angle $\alpha = \pi/2$ and a free vortex as the background flow.

The positions of the shed vortex and any free vortices evolve according to the simple ODEs (2.10) and (2.12), which can be solved using standard finite difference methods. A greater challenge is finding the value of the terms in these ODEs. In particular $\widetilde{\boldsymbol{u}}_{\mathrm{s}}(\boldsymbol{x}_{\mathrm{s}})$ and Γ in (2.10) and the velocity of the free vortex $\widetilde{\boldsymbol{u}}_{\mathrm{f}}(\boldsymbol{x}_{\mathrm{f}})$ in (2.12). These all depend on the streamfunction $\widetilde{\eta}$, which is the solution of the modified Helmholtz equation (2.14), a second order elliptic PDE. The numerical procedure employed here will be, at each point in time, to solve the PDE for the streamfunctions for the background flow and the flow due to the shed vortex and use these to compute $\widetilde{\boldsymbol{u}}_{\mathrm{s}}(\boldsymbol{x}_{\mathrm{s}})$, Γ and the velocity of any free vortices. This gives all the terms in the ODEs, which can then be solved using an implicit finite difference scheme.

A good first choice for solving the PDE (2.14) with boundary conditions only specified on the wedge boundaries and at infinity is a boundary integral method

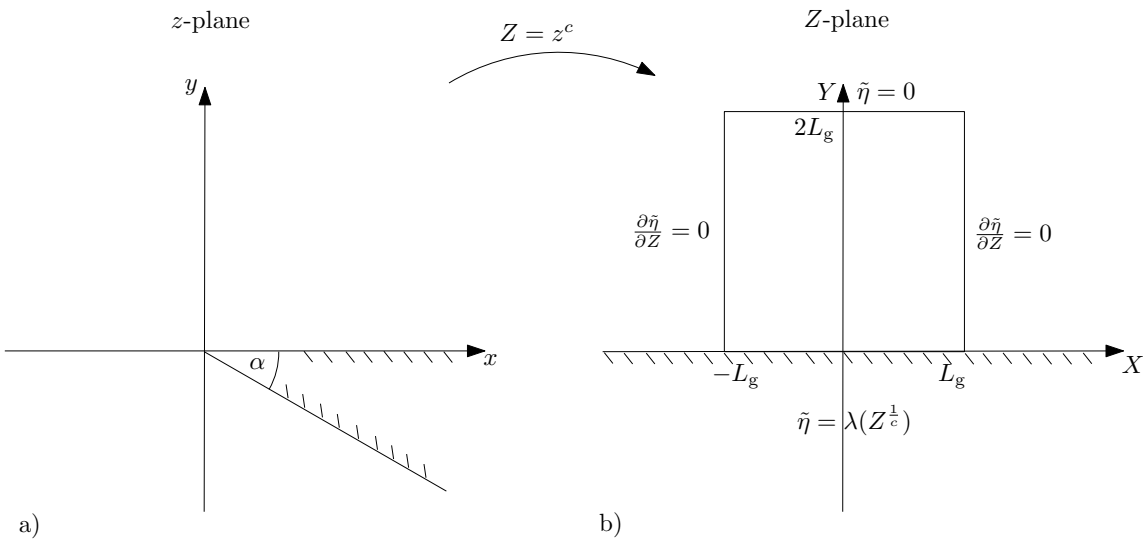

Figure 2.2: Schematic of a) the physical domain outside a wedge of angle α and b) the mapped plane showing the extent of the computational domain containing the Chebyshev grid (for $\alpha \neq 0$) and showing the boundary conditions applied in the numerical scheme. The mapping coefficient is $c = \pi/(\pi - \alpha)$.

[Nilawar et al., 2012]. However, derivatives of the streamfunction near the origin have a $|\boldsymbol{x}|^{(\alpha-\pi)/(2\pi-\alpha)}$ singularity and the implementation of the Kutta condition requires the coefficient of this singularity to be computed accurately. This is a significant challenge for the boundary integral method. An alternative, which deals effectively with the singularity problem, is to conformally map the problem to the upper half plane as shown in Fig. 2.2. Now the singularity is contained explicitly in the mapping and derivatives are bounded. However the mapping has changed the form of the PDE, and the open domain Green's function is not known, so a boundary integral method cannot be used. The half-plane geometry in the mapped plane suggests using a grid based method e.g. a finite difference or Chebyshev spectral method. Both of these methods using mapping had improved accuracy at the tip compared to the boundary integral method. The spectral method had the highest accuracy and the strongest convergence of all three methods for comparable computation times, so was selected.

2.3.2 Spectral method for finding $\widetilde{\eta}$

The leading order surface deformation $\widetilde{\eta}$ is the solution of the problem

$$\nabla^2\widetilde{\eta} - \frac{1}{a^2}\widetilde{\eta} = 0, \tag{2.15}$$

with boundary conditions

$$\widetilde{\eta} = \widetilde{\eta}_{\mathrm{b}}(\boldsymbol{x}), \qquad \text{for } \theta = 0,\ 2\pi - \alpha, \tag{2.16a}$$

$$\widetilde{\eta} \to 0, \qquad \text{as } r \to \infty, \tag{2.16b}$$

for some function $\widetilde{\eta}_{\mathrm{b}}(\boldsymbol{x})$, where (r, θ) are the polar coordinates of $\boldsymbol{x}$. (2.16a) ensures that the wedge is bounded by a streamline, so there is no flow through it. The physical problem being considered determines $\widetilde{\eta}_{\mathrm{b}}(\boldsymbol{x})$. For a steady flow anti-clockwise around the wedge $\widetilde{\eta}_{\mathrm{b}}(\boldsymbol{x}) = -1$ and for a vortex of unit strength at position $\boldsymbol{x}_{\mathrm{s}}$ the boundary condition on the wedge is $\widetilde{\eta}_{\mathrm{b}}(\boldsymbol{x}) = K_0(|\boldsymbol{x}-\boldsymbol{x}_{\mathrm{s}}|)/2\pi$. Derivatives of the solution to this problem have a $|\boldsymbol{x}|^{(\alpha-\pi)(2\pi-\alpha)}$ singularity at the origin, the coefficient of which must be found to satisfy the Kutta condition. This singularity is treated separately—avoiding its numerical difficulties—by conformally mapping to the upper half plane with the map $Z = z^c$, where $c = \pi/(2\pi-\alpha)$, for physical domain coordinates $z = x+\mathrm{i}y = r\mathrm{e}^{\mathrm{i}\theta}$ and mapped plane coordinates $Z = X + \mathrm{i}Y = R\mathrm{e}^{\mathrm{i}\Theta}$. Now derivatives in the physical domain are related to those in the mapped domain by

$$\begin{pmatrix} \frac{\partial\widetilde{\eta}}{\partial x} \\ \frac{\partial\widetilde{\eta}}{\partial y} \end{pmatrix} = \frac{c}{R^m} \begin{pmatrix} \cos m\Theta & -\sin m\Theta \\ \sin m\Theta & \cos m\Theta \end{pmatrix} \begin{pmatrix} \frac{\partial\widetilde{\eta}}{\partial X} \\ \frac{\partial\widetilde{\eta}}{\partial Y} \end{pmatrix}, \tag{2.17}$$

where $m = (\pi - \alpha)/\pi$, so the singularity is contained explicitly in the mapping and mapped plane derivatives are bounded at $X = Y = 0$. The modified Helmholtz equation (2.15) in the mapped plane is

$$\nabla^2\widetilde{\eta} - \frac{|Z^{2m}|}{c^2a^2}\widetilde{\eta} = 0 \tag{2.18}$$

where $\nabla^2 = \partial^2/\partial X^2 + \partial^2/\partial Y^2$, with boundary conditions appropriately changed as follows.

The PDE is solved using a Chebyshev spectral method with N^2 grid points. For general α it is solved on the square $-L_{\mathrm{g}} < X < L_{\mathrm{g}}$, $0 < Y < 2L_{\mathrm{g}}$ as shown in Fig. 2.2b), but for $\alpha = 0$, the symmetry across the Y-axis can be exploited and the

domain $0 < X < L_\mathrm{g}$, $0 < Y < 2L_\mathrm{g}$ is used. The boundary condition on the X-axis is

$$\widetilde{\eta} = \widetilde{\eta}_\mathrm{b}(Z^{\frac{1}{c}}), \qquad \text{for } Y = 0. \tag{2.19}$$

The far-field boundary conditions are imposed on the other sides of the square. These are approximate for a finite numerical domain so introduce an error exponentially small in L_g/a. The boundary conditions become exact in the limit $L_\mathrm{g}/a \to \infty$ and the effect of the error introduced decays exponentially away from the boundary. On the top this gives

$$\widetilde{\eta} = 0, \qquad \text{for } Y = 2L_\mathrm{g}, \tag{2.20}$$

and on the sides it is

$$\frac{\partial \widetilde{\eta}}{\partial X} = 0, \qquad \text{for } X = \pm L_\mathrm{g}, \tag{2.21}$$

for general α, or

$$\frac{\partial \widetilde{\eta}}{\partial X} = 0, \qquad \text{for } X = 0,\ L_\mathrm{g}, \tag{2.22}$$

for $\alpha = 0$. When $\alpha = 0$ the boundary condition on $X = 0$ is in fact exact, by symmetry.

Solving (2.18) with the boundary conditions (2.19), (2.20) and (2.21) or (2.22) with a spectral method yields a solution on the grid from which derivatives can be calculated spectrally at any point and used to find derivatives in the physical plane via (2.17). The Kutta condition can be implemented by finding $\partial\widetilde{\eta}/\partial Y(0,0)$ both for the background flow and for a vortex of unit strength. For the special case of a semi-infinite plate ($\alpha = 0$) and constant boundary condition, say $\widetilde{\eta}_\mathrm{b}(x) = -1$, the numerical results indicate that the solution along the Y-axis is $\widetilde{\eta}(0, Y) = -\operatorname{erfc}(Y/\sqrt{a})$, the complementary error function, as demonstrated in appendix A.1 and confirmed by the analytical solutions in appendix A.5 and in Johnson and Southwick [2016]. This simplifies the implementation of the Kutta condition in this case.

2.3.3 Timestepping scheme for the QGBM equation

The $\dot{\Gamma}$ term in the QGBM equation suggests an implicit scheme over an explicit one, since the latter can only calculate $\dot{\Gamma}$ with a lag. For convenience rewrite the QGBM equation (2.10) as

$$\dot{x} = u + f\dot{\Gamma}, \tag{2.23a}$$

$$\dot{y} = v + g\dot{\Gamma} \tag{2.23b}$$

where $\boldsymbol{x}_\mathrm{s} = (x_\mathrm{s}, y_\mathrm{s})^\top$ and $\widetilde{\boldsymbol{u}}_\mathrm{s}(\boldsymbol{x}_\mathrm{s})$ are rewritten as $\boldsymbol{x} = (x, y)^\top$ and $(u, v)^\top$ respectively and

$$(f, g)^\top = -\frac{\boldsymbol{x}}{|\boldsymbol{x}|\Gamma} \int_0^{|\boldsymbol{x}|} \frac{r}{a} K_1\left(\frac{r}{a}\right) \mathrm{d}r. \tag{2.24}$$

Given the shed vortex position, the spectral method can be used to compute u, v and Γ (via the Kutta condition), then f and g follow straightforwardly from (2.24). The QGBM equation is discretised using a second order central difference scheme

$$\frac{x_{n+1} - x_n}{h} = \frac{u_{n+1} + u_n}{2} + \left(\frac{f_{n+1} + f_n}{2}\right)\left(\frac{\Gamma_{n+1} - \Gamma_n}{h}\right), \tag{2.25a}$$

$$\frac{y_{n+1} - y_n}{h} = \frac{v_{n+1} + v_n}{2} + \left(\frac{g_{n+1} + g_n}{2}\right)\left(\frac{\Gamma_{n+1} - \Gamma_n}{h}\right), \tag{2.25b}$$

with timestep h. This is a widely used implicit finite difference method with good accuracy and improved stability over an explicit scheme. This gives a non-linear root finding problem, $\boldsymbol{F}(x_{n+1}, y_{n+1}) = 0$, for x_{n+1}, y_{n+1} which is solved with Broyden's method [Broyden, 1965]. In the Broyden's method calculation a first order explicit approximation is used for the initial guess of (x_{n+1}, y_{n+1}), the known rigid-lid solution (obtained via conformal mapping) for $\dot{\Gamma}$ is used at the first timestep and a first order approximation is used for the Jacobian matrix of $\boldsymbol{F}(x_{n+1}, y_{n+1})$ on the first iteration.

2.3.4 Practicalities for the numerical scheme

In addition to a description of the main scheme, there are some practical details that merit description. First, in the case with a free vortex present as well as the shed

vortex, there is a second pair of ODEs, $\dot{\boldsymbol{x}}_\mathrm{f} = \boldsymbol{u}_\mathrm{f}$, to solve. These are also discretised using a central difference scheme and there are now four unknowns to be found using Broyden's method. Second, in the numerical scheme, it is not possible for a vortex to be exactly at the tip of the wedge as this would give a singularity in $\widetilde{\eta}_\mathrm{b}(\boldsymbol{x})$ at the tip. Therefore an initial shed vortex position very close to the tip is used instead. Being close to the tip (i.e. much less than the lengthscale a) is equivalent to the rigid-lid limit so the initial condition used for the shed vortex position $(x_{\mathrm{s}_0}, y_{\mathrm{s}_0})$ is a point along the rigid-lid trajectory. For a small distance from the tip (typically $\sim 10^{-2}a$ is used) this introduces a small error in the initial trajectory, of magnitude less than a tenth of the distance of the tip from the starting point. Furthermore, tests with vortices with various initial positions relax quickly to the same solution as shown in Fig. 2.3. That is, the vortex trajectory is insensitive to the choice of the initial location of the shed vortex. The test trajectories start evenly spaced on a circle surrounding the point $(0, -0.01)$ and are all therefore in the lower half plane, consistent with the rigid-lid trajectory where the vortex is shed in the negative y-direction. In the tests the initial error decreases very rapidly, dropping several orders of magnitude very quickly, then settling on a slower but still exponential decrease. Physically this is primarily due to the restorative effect of the Kutta condition. Displacing a vortex from its trajectory changes its strength. This changes the size of the component of the vortex velocity due to the interaction between the vortex and the physical boundaries, which acts against the displacement. Overall the error caused by the initial position is insignificant in determining the ultimate trajectory of the shed vortex. The speed of the vortices may change significantly over a trajectory so a variable timestep is used. The velocity scale is approximated by

$$\text{velocity scale} = \frac{1}{a}\max\left(K_1\left(\frac{2y_\mathrm{f}}{a}\right), \Gamma K_1\left(\frac{2y_\mathrm{s}}{a}\right), K_1\left(\frac{|\boldsymbol{x}_\mathrm{s} - \boldsymbol{x}_\mathrm{f}|}{a}\right)\right) \tag{2.26}$$

i.e. as the maximum of the image velocity of the free or shed vortex or as the direct velocity exerted by the free vortex on the shed vortex. In the case of no free vortex, just the image of the shed vortex is used. The timestep is then scaled on 1/velocity scale. The size, L_g, of the spectral grid in the mapped plane is chosen such that the solution is always closer to the plate than to the boundaries with approximate

boundary conditions.

2.3.5 Validation of the numerical scheme

A number of tests were used to validate the numerical scheme. In all cases the results converge with increasing grid resolution N or grid size L_g (for constant N/L_g) and decreasing timestep h. For large a the scheme is able to closely reproduce several rigid-lid results: a shed vortex trajectory for a steady background flow, close to the plate (Fig. 2.4); a free vortex trajectory around a semi-infinite plate (Fig. 2.6) or wedge; the velocity $\partial\widetilde{\eta}/\partial x(0,0)$ (as required for the Kutta condition) for both a steady flow and a vortex around a semi-infinite plate; and the trajectories of a free and shed vortex around a semi-infinite plate (Fig. 2.7) and a wedge (Fig. 2.10). For a wedge with angle $\alpha = \pi$ (i.e. an infinite plate with a separation point specified at the origin) in QG flow, the ODEs for the vortex positions can be found exactly using the method of images. Integrating these using standard accurate Runge–Kutta methods gives a solution that matches that of the numerical scheme described here and also the rigid-lid solution when the free vortex is initially close to the plate. There are few analytical results to compare with in the limit $a \to 0$, aside from the trajectory of a free vortex around a semi-infinite plate which can also be closely reproduced (Fig. 2.6, the trajectory for $a = 0.01$ is barely distinguishable from the analytical result).

Although the convergence of the spectral method is good, a large number of grid points are needed in both the large a limit, where a large grid is needed to avoid the influence of the approximate boundary conditions; and in the small a limit, where many grid points are needed to resolve a sharply varying streamfunction. Hence—as well as for oceanographic relevance—the results considered will typically fall in the range $10^{-1} < a < 10^2$. All numerical results in this work have been run at a range of numerical parameters and compared with each other to ensure accuracy.

2.4 Results

2.4.1 Steady flow around a semi-infinite plate

The first example considered is vortex shedding owing to a steady background flow around a semi-infinite plate with boundary conditions $\eta = -1$ on the plate (all time-dependent cases can be collapsed on to this through scaling time), $\eta \to 0$ at infinity and with no singularities (other than the shed vortex) in the flow. The exact solution [Cortelezzi, 1995] to the Brown-Michael vortex shedding problem in the rigid-lid limit (a flow with free-stream speed $-2/\sqrt{\pi}$ along the top of the plate) is a vortex shed perpendicular to the plate with trajectory

$$(x_\mathrm{s}, y_\mathrm{s}) = \left(0, -\frac{t^{\frac{2}{3}}}{2\pi^{\frac{1}{3}}}\right). \tag{2.27}$$

For the QG problem there is no lengthscale other than the Rossby radius, so lengths can be scaled on the Rossby radius to collapse all cases on to the $a = 1$ solution. To demonstrate the insensitivity of the trajectories to the initial position, Fig. 2.3 shows shed vortex trajectories for vortices with different initial conditions which are far further apart than the possible initial error caused by starting along the rigid-lid trajectory. These rapidly relax to the same trajectory. The numerical solution for the vortex trajectory is shown in Fig. 2.4. Initially the solution follows the rigid-lid trajectory as predicted. As it moves further from the plate tip it starts to deviate to its left and continues along a curved trajectory away from the plate tip. The largest difference, however, is the speed of the two solutions. While the distance of the rigid-lid vortex from the plate tip increases like $t^{\frac{2}{3}}$, the distance of the QG vortex from the tip increases like $\log t$. More precisely, Fig. 2.5 shows that for large time, $1/K_1(\boldsymbol{x}_\mathrm{s}) \sim t \sim \Gamma \sim 1/|\dot{\boldsymbol{x}}_\mathrm{s}|$, consistent with the QGBM equation (2.10). This slower motion is a consequence of the deforming free surface meaning image effects are felt much more weakly.

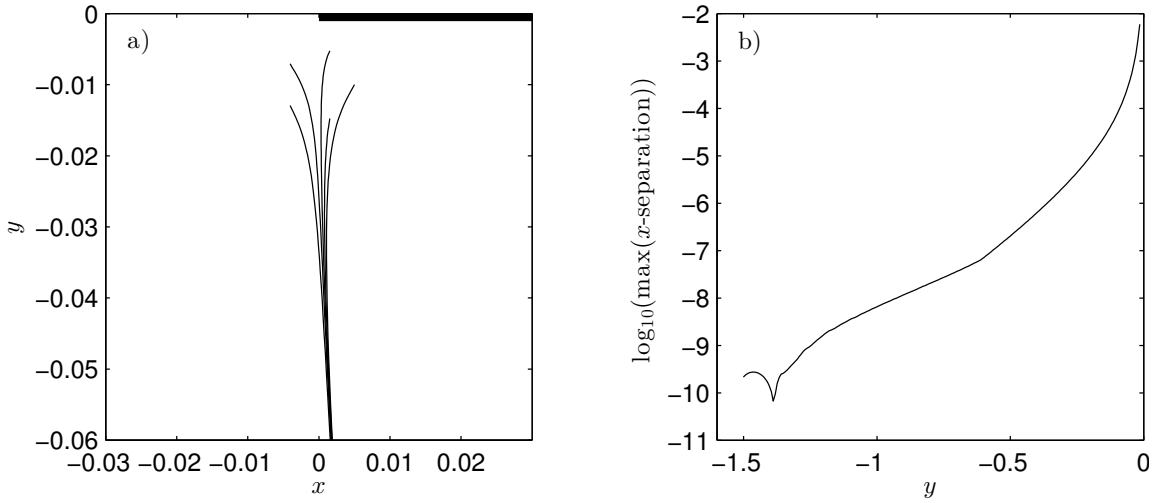

Figure 2.3: a) Trajectories for shed vortices starting at five different points then advancing following the quasigeostrophic Brown–Michael equation for a vortex shed from the tip of a semi-infinite plate under a steady flow. The five initial conditions are points equally spaced around a circle of radius 0.005 surrounding the point $(0, -0.01)$, which will be used as the initial condition for later runs. b) The base 10 logarithm of the maximum x-separation at fixed y of the five trajectories as a function of y. The trajectories differ by less than 10^{-8} at distances further than one Rossby radius from the plate.

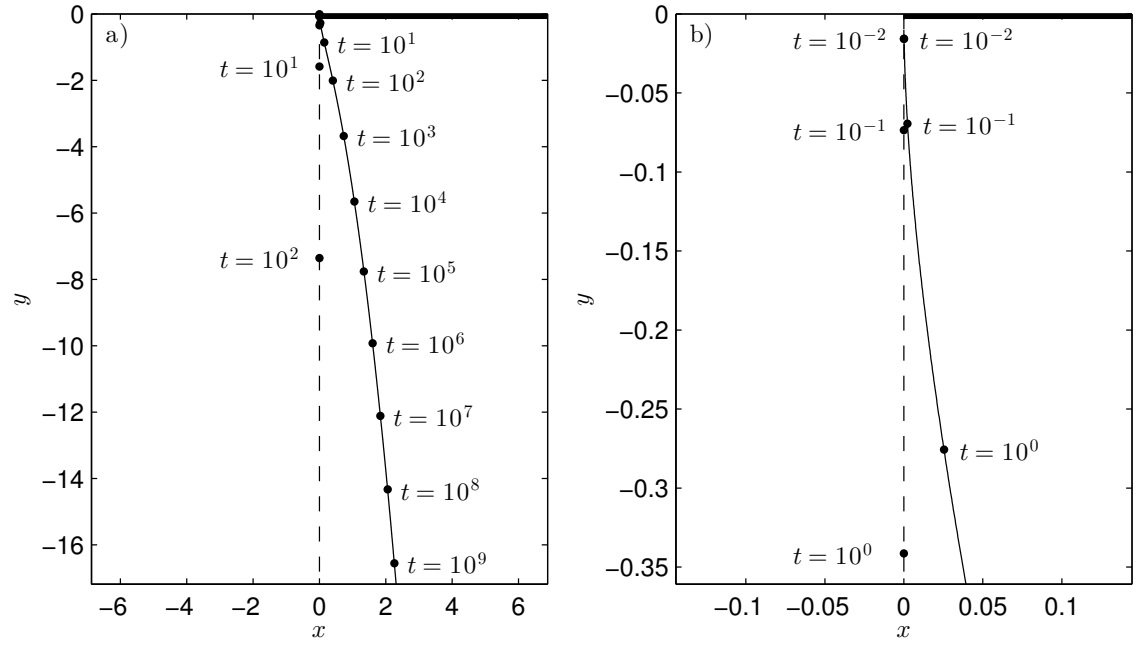

Figure 2.4: Trajectories of Brown–Michael shed vortices for a steady flow around a semi-infinite plate. The QG ($a \neq 0$) solution (solid line) is computed numerically and the rigid-lid ($a \to \infty$) solution (dashed) is exact. The plate is shown in dark along the positive x-axis. The two views are a) the full solution and b) a view focused on the origin, showing that the solutions are initially identical. The solution at various time points has been marked, demonstrating how much slower the QG vortex is. The initial position of the QG vortex was $(x_{s_0}, y_{s_0}) = (0, -0.01)$.

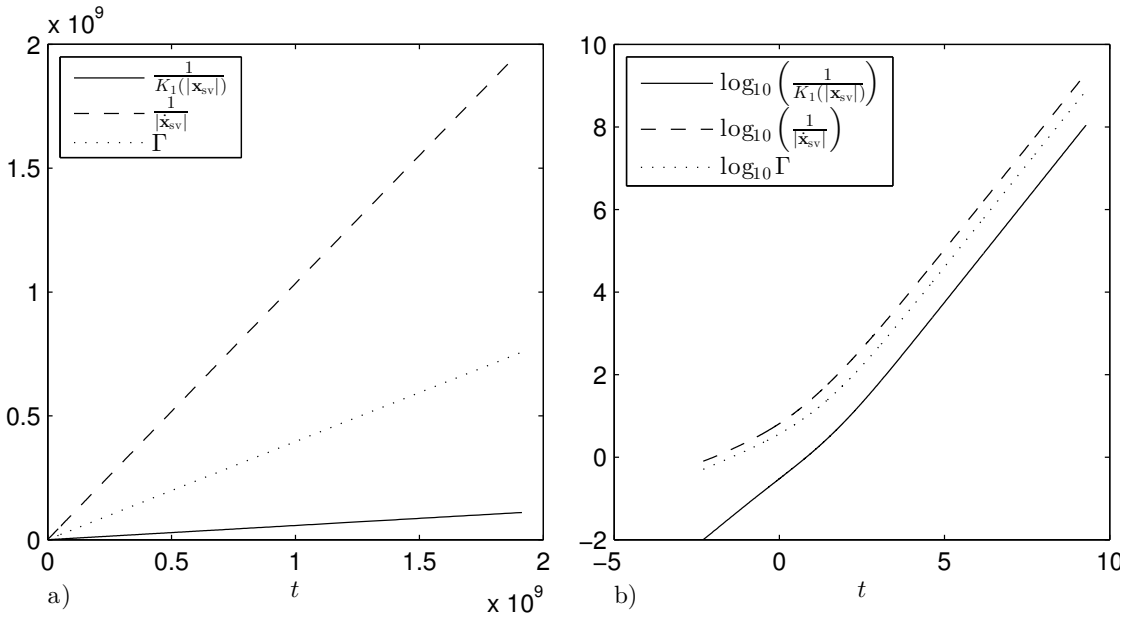

Figure 2.5: a) Standard and b) log–log plots of $1/K_1(|\boldsymbol{x}_s|)$ (solid), $1/|\dot{\boldsymbol{x}}_s|$ (dashed) and Γ (dotted) against t showing the large time position, velocity and circulation of a shed vortex in a steady flow around a semi-infinite plate.

2.4.2 Free vortex around a semi-infinite plate

The second example considered is a background flow consisting of a free vortex of negative unit circulation (more general circulations can be recovered through scaling time) moving around a semi-infinite plate, starting at some finite normal distance from the plate but a large distance from the plate tip. Here, the initial distance between the plate and the vortex provides a natural lengthscale so the parameter a stays in the problem and will parametrise a family of solutions.

Fig. 2.6 shows vortex trajectories for a single free vortex around a semi-infinite plate for various a with no vortex shedding. The vortex is initially far upstream and at unit distance from the plate i.e. $x_{f0} \gg a$, $y_{f0} = 1$. The solutions for $a \to 0$ and $a \to \infty$ are exact and the other solutions are computed using a boundary integral method (the spectral scheme described here reproduces the same results). The rigid-lid solution ($a \to \infty$) can be found by constructing the vortex Hamiltonian in the upper half plane, then conformally mapping to the semi-infinite plate domain using the known transformation properties of the Hamiltonian under mapping [Saffman, 1992]. The trajectory in the limit $a \to 0$ is new and is derived in Appendix A.2. It is a straight line parallel to the wall from infinity to $x = 0$, then a semi-circular arc

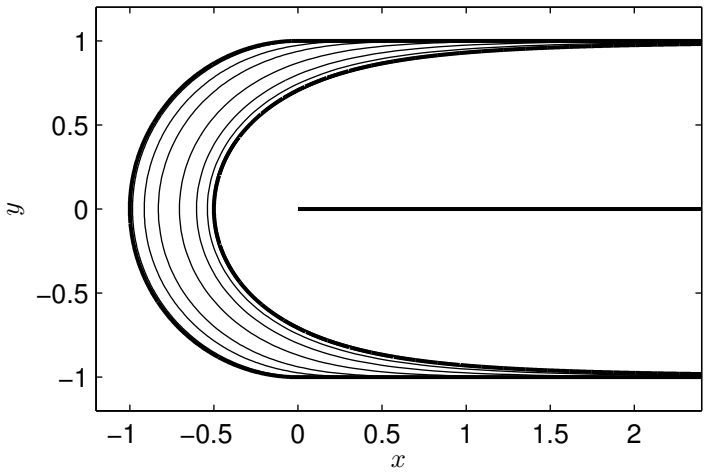

Figure 2.6: Free vortex trajectories around a semi-infinite plate, starting from $(x_{f_0}, 1)$ for $x_{f_0} \gg a$, without vortex shedding for (left to right) $a \to 0$ (bold), a= 0.01, 0.1, 0.3, 1, 3, 10 and $a \to \infty$ (bold). Bold solutions are exact and non-bold are computed with a boundary integral method and Runge–Kutta timestepping.

around the plate tip then a straight line parallel to the wall again from $x = 0$ back toward infinity, all at constant speed $(\Gamma/2\pi a)K_1(2/a)$, which is exponentially small in $1/a$. All of these solutions pass around the plate tip and get closest to it as they cross the x-axis. The distance of closest approach depends monotonically on a and varies from 0.5 for $a \to \infty$ up to 1 for $a \to 0$.

If flow separation is included then a second vortex is shed from the plate tip and the two interact. Trajectories for the free and shed vortices are computed for QG flow as before using the spectral method and implicit timestepping described in Sec. 2.3. The coupled ODEs governing the rigid-lid trajectories are found by conformally mapping to the upper half plane (described in Appendix A.3) and then integrated using Runge–Kutta timestepping. Fig. 2.7 shows the trajectories of pairs of free and shed vortices for various a including the rigid-lid limit. For all values of a, instead of the free vortex moving symmetrically around the plate, the two vortices pair up and move off to infinity along parallel straight trajectories in the upper half plane. The straight line trajectory is worth remark and implies that the circulation of the shed vortex tends to equal, and opposite sign, that of the free vortex. The eventual angle of propagation (defined as the angle between the ultimate trajectory and positive x-axis) of the pair of vortices increases monotonically with increasing a. The inclusion of flow separation has made a dramatic change to the trajectory: without flow separation the free vortex moves around the plate

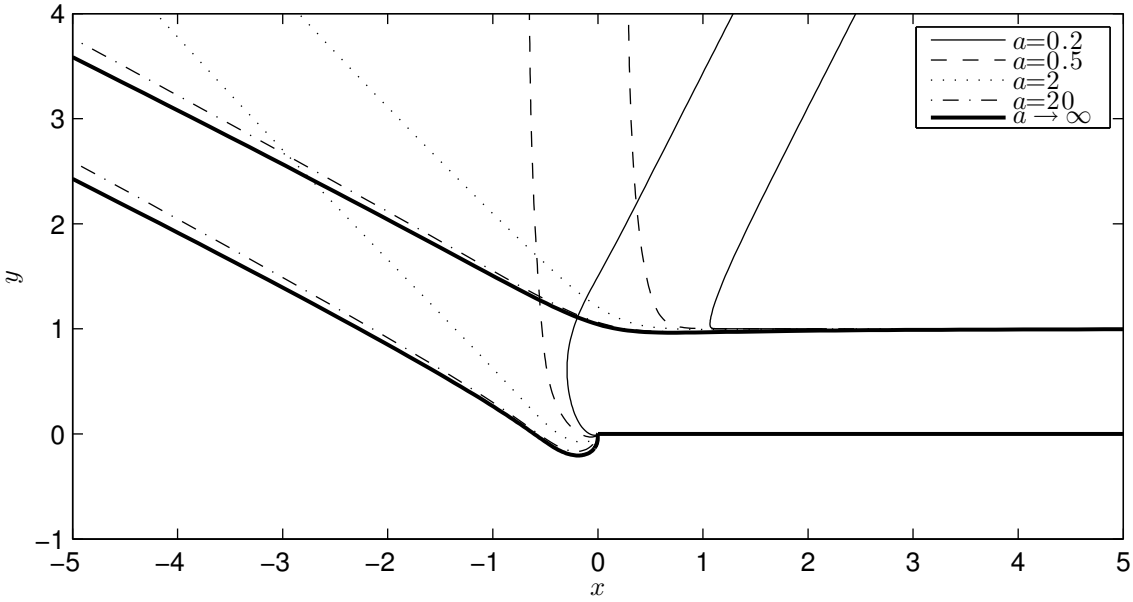

Figure 2.7: Trajectories of a free vortex starting from $(x_{\mathrm{f}_0}, 1)$ (for $x_{\mathrm{f}_0} \gg a$) and a vortex shed from the tip of a semi-infinite plate along the positive x-axis (shown in bold) for $a = 0.2$ (solid), 0.5 (dashed), 2 (dotted), 20 (dash dotted) and $a \to \infty$ (bold). The solution for $a \to \infty$ was computed by integrating the analytically obtained ODEs for the vortex positions with a Runge–Kutta scheme (Appendix A.3). For finite a, the solutions were computed using the spectral method and implicit timestepping scheme described in Sec. 2.3. The final propagation angle increases monotonically with increasing a.

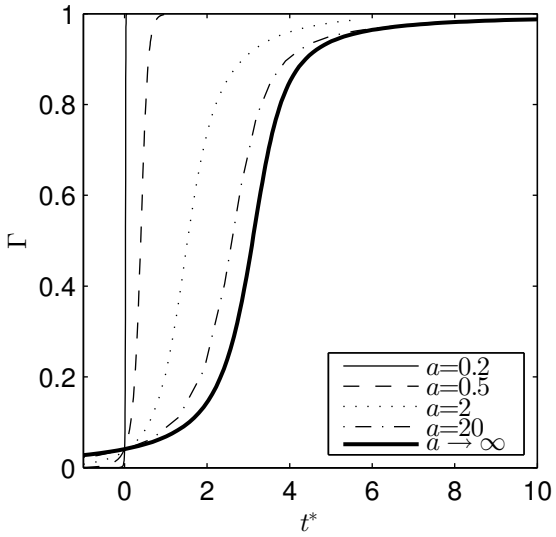

Figure 2.8: The circulation Γ of vortices shed from the tip of a semi-infinite plate as a free vortex of unit strength approaches from $(x_{f_0}, 1)$ where $x_{f_0} \gg a$, for various values of a. The circulation is plotted over time t^*, scaled so that in each case the free vortex is initially moving at unit speed i.e. the scaled time t^* relates to physical time t via $t^* = (2\pi a/K_1(2/a))t$, using the initial speed given by the image of the free vortex in the plate. The curves have been translated so that at $t^* = 0$ they all have the same, small circulation. Therefore, the crossing point of the curves is arbitrary and of no physical importance.

symmetrically and ultimately propagates parallel to the plate on the far side and in the opposite direction for all a. With flow separation, the symmetry is broken and the free vortex does not pass around the plate tip and instead ultimately propagates away from the plate in the upper half plane, with the angle of propagation strongly dependent on a.

The circulation of shed vortices for various values of a are plotted over time in Fig. 2.8. For all a, the circulation grows from zero to unity, the strength of the free vortex. Fig. 2.8 shows that, for large a, the circulation grows over the same timescale as the initial movement of the free vortex while, for small a, it grows far quicker. The final separation distance between each pair of vortices and their final angle of propagation is shown in Fig. 2.9. While the angle is monotonically increasing with a, the separation distance has a less obvious relationship with a, but is always $\mathcal{O}(1)$ and less than the initial separation between the free vortex and its image in the plate.

The limit $a \to 0$ is very demanding on the numerical scheme as surface deformations decay over short length scales so high resolution is required, but some progress can be made analytically. According to the method of images, far from the tip the

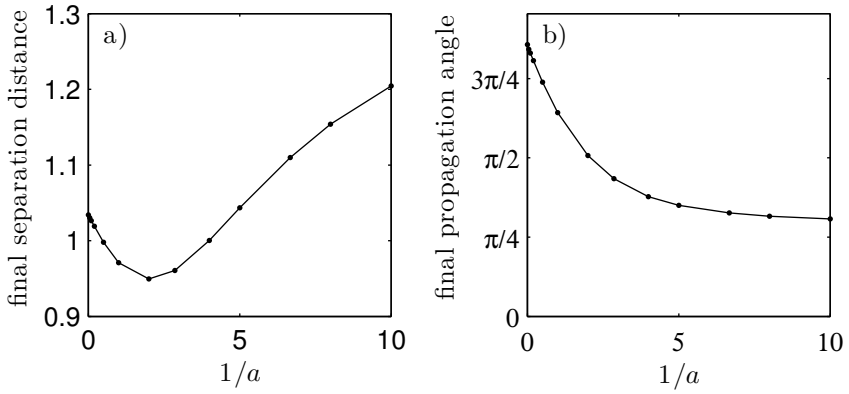

Figure 2.9: a) The final separation distance between each pair of free and shed vortices and b) their final angle of propagation for varying $1/a$ (to include the $a \to \infty$ result). The separation distance is always significantly smaller than 2—the original separation between the free vortex and its image—so the free vortices are accelerated by shedding. The final propagation angle varies significantly and increases monotonically with increasing a.

free vortex moves parallel to the wall at speed $K_1(2/a)/2\pi a$ which is exponentially small for small a. Rescaling the vortex strength on $K_1(2/a)/2\pi a$ gives a vortex moving at unit speed. It will have an $\mathcal{O}(\mathrm{e}^{(2-|\boldsymbol{x}_\mathrm{f}|)/a})$ effect on the flow at the plate tip. So, in the limit $a \to 0$ the effect at the tip is infinitely small for $|\boldsymbol{x}_\mathrm{f}| > 2$, $\mathcal{O}(1)$ for $|\boldsymbol{x}_\mathrm{f}| = 2$, then infinitely large for $|\boldsymbol{x}_\mathrm{f}| < 2$. Thus, it is expected that the shedding will abruptly begin when $|\boldsymbol{x}_\mathrm{f}| = 2$. The shed vortex has negligible effect on the free vortex until it reaches a distance 2 from the plate tip and therefore has comparable strength to the free vortex. At this point, if the vortices are a distance 2 or less from each other they pair up and move off to infinity on a straight line. Balancing this analysis against the numerical results suggests that the free vortex moves parallel to the wall until it reaches a distance 2 from the tip, at which point the shed vortex is almost instantaneously shed and moves until it reaches a distance 2 from the plate. Then the two move off as a pair at a shallower angle than the $a = 0.1$ solution already computed. Therefore the free vortex trajectory in the limit $a \to 0$ is expected to be a straight line parallel to the wall up to $|\boldsymbol{x}_\mathrm{f}| = 2$, a sharp turn, then a straight line away again at some angle, conjectured to be around $\pi/4$ based on Fig. 2.9.

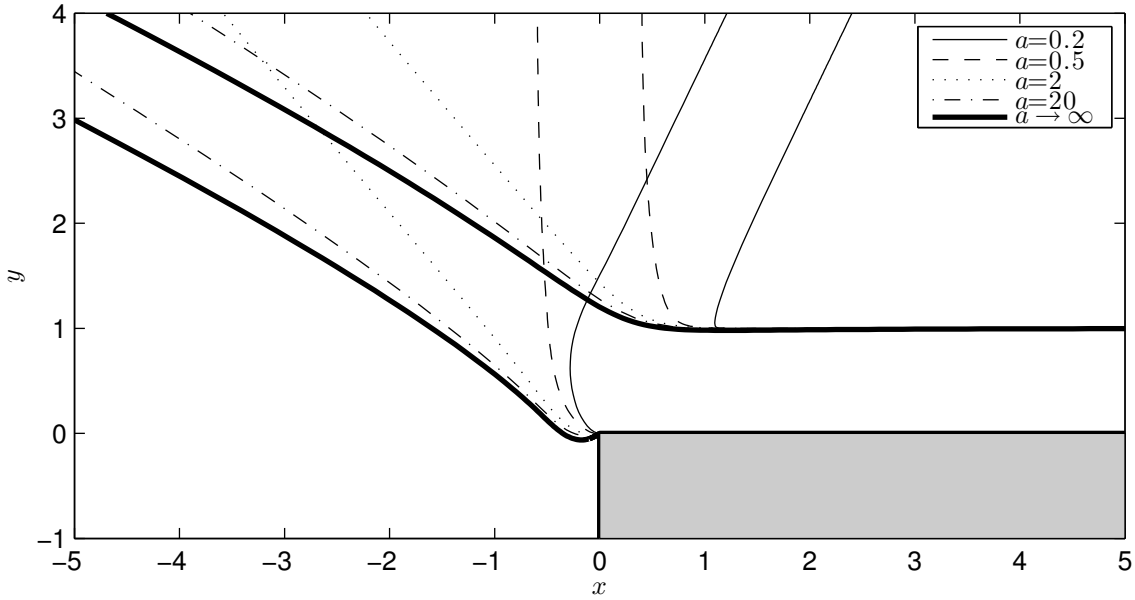

Figure 2.10: Trajectories for a free vortex starting at $(x_{f_0}, 1)$ (for $x_{f_0} \gg a$) and a Brown-Michael vortex shed from the tip of a wedge of angle $\alpha = \pi/2$ (shown in grey) for $a = 0.2$ (solid), 0.5 (dashed), 2 (dotted), 20 (dash dotted) and $a \to \infty$ (bold). The rigid-lid solution ($a \to \infty$) was computed by numerically integrating the analytically obtained ODEs for the vortex motions as described in Appendix A.3 and the QG solutions were computed using the method of Sec. 2.3.

2.4.3 Free vortex around a right-angled wedge

The third example considered has background flow of a free vortex moving around a right-angled wedge ($\alpha = \pi/2$), starting a finite normal distance from the upper side of the wedge, far from the wedge tip. As it moves around the wedge, a Brown–Michael vortex is shed from the tip of the wedge. Numerically computed solutions (as in Sec. 2.4.2) for the trajectories of the two vortices for various values of a (including the limit $a \to \infty$) are shown in Fig. 2.10. Similar to the case of a free vortex around a semi-infinite plate, for all a, the free and shed vortices pair up and move away to infinity. Thus separation has again had a significant effect: the trajectories found are very different to the trajectories of a free vortex around a wedge without the effects of shedding included, which would be symmetrical about a line bisecting the wedge.

The trajectories of a free and shed vortex around a wedge are compared to those around a semi-infinite plate in Fig. 2.11. For small a, when the trajectories do not pass the wedge tip, the results are very similar. For larger a, when the trajectories do pass the plate tip and therefore are a similar distance from both sides of the wedge,

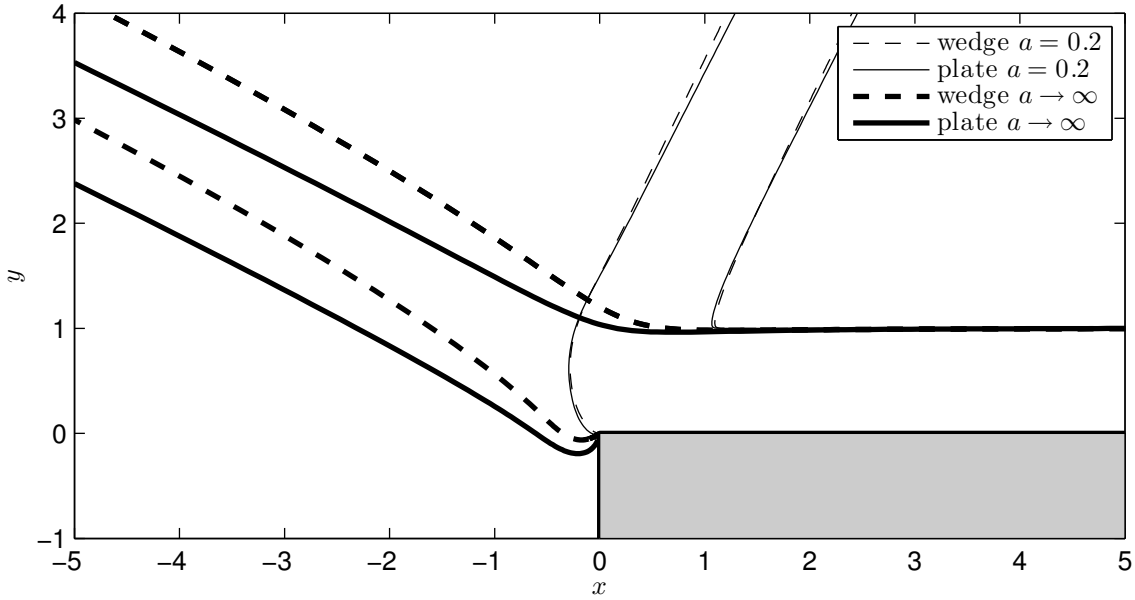

Figure 2.11: Comparison of trajectories around a semi-infinite plate and a wedge. Shown are the trajectories of a free and shed vortex around a semi-infinite plate for $a = 0.2$ (solid) and $a \to \infty$ (solid bold) and around a wedge for $a = 0.2$ (dashed) and $a \to \infty$ (dashed bold). For $a = 0.2$ the trajectories for a semi-infinite plate and wedge are very similar whereas for $a \to \infty$ they differ markedly.

the results differ more significantly. The final propagation angle for the semi-infinite plate trajectory is larger than for the wedge and the large time trajectory is flatter.

2.5 Conclusions

In this chapter the effects of vortex shedding and the effect of the Rossby radius are considered for three background flows: a steady flow around a semi-infinite plate (A), a free vortex moving around a semi-infinite plate (B) and a free vortex moving around a right-angled wedge (C). For the steady flow, a vortex is shed from the plate in a similar fashion to rigid-lid flow, but slows down exponentially with increasing distance from the tip. This would suggest that, in the ocean, shed eddies are more likely to be found closer to the topography they are shed from than would have been predicted with the original rigid-lid theory. These eddies may be moving slowly enough to appear trapped. The trajectory of the shed eddy is initially the same as in rigid-lid flow but then deflects away and follows a curved path.

For a free vortex moving around a semi-infinite plate, the inclusion of flow sep-

aration significantly changed the vortex trajectory. With no shedding, free vortices for all values of the Rossby radius move around the plate symmetrically, returning in the opposite direction and on the opposite side of the plate from which they approached. With shedding included, and again for all values of the Rossby radius, the shed vortex grew to comparable strength to the free vortex before the free vortex could round the tip and the two moved off as a pair to infinity in the upper half plane. This result is of significant interest and could merit further investigation. The first step of this should be to test this conclusion against other models such as a vortex sheet method or a model with viscosity explicitly included. If the conclusion is robust then it would be worth bearing in mind in studies of oceanic flow where there is sharply curved boundary topography but no inclusion of flow separation explicitly or via viscosity.

The Rossby radius has a significant effect on the final propagation direction of the vortex pair. This direction varied by as much as approximately $\pi/2$ between the rigid-lid limit and small Rossby radius results. It is also worth noting that, as for the steady flow, the inclusion of surface deformation slows the vortex but that the vortex pair move significantly faster than the free vortex moves initially. This acceleration is strongest for the lowest Rossby radius flows. Thus, the inclusion of flow separation not only significantly effects the free vortex trajectory but also accelerates it.

In the case of a free vortex moving around a right-angled wedge, similar results to the semi-infinite plate are found. For all values of a, the free and shed vortices pair up and move off to infinity in the upper half plane. As with the semi-infinite plate, their final angle of propagation depends monotonically on a. Comparison of trajectories around the wedge and the semi-infinite plate reveals very similar results for low a where the trajectories do not pass the plate tip and therefore are always much closer to the near side of the wedge than the far side. For higher a where the trajectories do pass the plate tip, the results are more different, with the trajectories for the wedge being deflected into the upper half plane more strongly.

Chapter 3

Applications of the quasigeostrophic Brown–Michael model to "sheddies" – ocean eddies formed from shed vorticity

In this chapter the quasigeostrophic Brown–Michael (QGBM) model is applied to a number of well known examples of sheddy formation, including the Agulhas Cyclones, California Undercurrent and Canary Eddy Corridor, and also to investigate the effects of shed vorticity in the growth of the Cook Strait Eddy and the interaction of the North Brazil Current Rings with the islands of the Lesser Antilles. The model shows good qualitative agreement with observations and experimental and numerical results. A detailed discussion of the vorticity fluxes in the model is also given.

3.1 Introduction

Sheddies are commonly found near islands e.g. the Canaries, Seychelles or Izu Islands [Heywood et al., 1996, Isoguchi et al., 2009, Sangrà et al., 2007], all of which lie in the path of strong currents. The Canaries, for example, form a barrier disrupting the southwestward flow of the Canary Current, and shed eddies continuously. These eddies initially move southwestward with the current before turning west under the influence of the β-effect. The chain of mesoscale eddies this produces, known as the

Canary Eddy Corridor, has been estimated to be responsible for around a quarter of the mass transport and half of the kinetic energy transport of the Canary Current [Sangrà et al., 2009].

Another common origin for sheddies are sharply varying coastlines such as capes [Jiang et al., 2011]. An example of this are the sheddies formed on the leeward side of the Agulhas bank [Penven et al., 2001]. These sheddies play an important role in triggering the formation of the Agulhas Rings [Lutjeharms et al., 2003]—the main interchange mechanism between the Indian and Atlantic Oceans. Sheddies can also be formed from both eastern [Molemaker et al., 2015] and western [Gula et al., 2015] boundary currents. Here highly asymmetric distributions of cyclonic and anticyclonic eddies are observed when the boundary layer separates at points along the coast with particularly high curvature.

The separation of shear layers may have impacts on other ocean processes as well. A potentially important example is the impact of sheddies on other eddies encountering topography such as the North Brazil Current rings (NBC rings) meeting the islands of the Lesser Antilles [Fratantoni and Richardson, 2006]. Numerical [Simmons and Nof, 2002] and experimental [Duran-Matute and Velasco Fuentes, 2008, Tanabe and Cenedese, 2008] investigations have seen flow separation around the Lesser Antilles as a NBC ring approaches. Additionally many smaller eddies which may have separation of shear layers as their origin have been observed in the paths of buoys to the west of the islands [Richardson, 2005]. The QGBM model enables an investigation of the role of sheddies in determining the trajectories and survival rate of the NBC rings. There are also cases of eddies, such as the Cook Strait eddy, whose origin is unknown [Barnes, 1985]. It is suggested here that vorticity ejected from a boundary shear layer could be the source of these eddies.

Section 3.2 introduces the model and techniques. Section 3.3 discusses a boundary current along a stepped coastline in relation to the California Undercurrent passing Point Sur, modelled here as a backwards facing step. The model allows a straightforward discussion of the rate of expulsion of vorticity into the fluid and its subsequent rolling up into an eddy. Section 3.4 models the sheddies formed in the lee of the Agulhas bank as flow around a wedge. Section 3.5 examines eddies formed at gaps in barriers and is split into three subsections, each considering a different oceano-

graphic scenario. Section 3.5.1 models the flow through Cook Strait and investigates whether flow separation could explain the large trapped eddy found at the mouth of the gap. Section 3.5.2 investigates the interaction of North Brazil Current Rings with the islands of the Lesser Antilles. Section 3.5.3 discusses the Canary Eddy Corridor, a chain of sheddies formed at the Canary Islands but extending far out into the Atlantic. Section 3.6 presents conclusions.

3.2 The quasigeostrophic Brown–Michael model

As derived earlier, the evolution of shed vortices is given by the quasigeostrophic Brown–Michael (QGBM) equation

$$\dot{\boldsymbol{x}}_i = \widetilde{\boldsymbol{u}}_i - \frac{\dot{\Gamma}_i}{\Gamma_i}\frac{\boldsymbol{x}_i}{|\boldsymbol{x}_i|}a\int_0^{\frac{|\boldsymbol{x}_i|}{a}} sK_1(s)\,\mathrm{d}s. \tag{3.1}$$

A commonly used and physically realistic additional condition, first applied by Graham [1980], is that the circulation of any shed vortex may only increase (and not decrease) in time as it is 'fed' by the continuous shedding of vorticity from the separation point. If $\dot{\Gamma}_i$ changes sign, the vortex is cut off, its circulation is frozen and it continues as a free vortex with a new shed vortex created at the separation point. This new vortex necessarily has opposite signed circulation to the cut-off vortex. In practice it is computationally simpler to limit the number of new vortices when adding vortices would do little to change the overall dynamics. Therefore a practical amendment to the Graham [1980] condition is to introduce a new vortex only when the decrease in circulation is significant, avoiding introducing a large number of new vortices when the shed vorticity fluctuates rapidly with small amplitude. The computations here introduce a new vortex if the sheddy circulation decreases by 5% from its maximum value.

For very large shed eddies, far from the separation point, instabilities in the vortex sheet connecting the sheddy to the separation point start to dominate, destroying the vortex sheet and stopping the growth process. This can be represented in the

QGBM model by cutting off a shed vortex and starting a new vortex if the shed vortex meets some condition. Appropriate choices could be some maximum circulation or a maximum distance from the separation point. This is particularly relevant for vortices shed from the edges of a gap, which form pairs and then propagate as a single entity. At this point they are no longer being fed by the separation point vorticity. These pairs are thus modelled here as free vortices when the distance between the two vortices forming the pair is shorter than the distance from the vortices to their separation points. Subsection 3.5.3 discusses these criteria and their effects.

Chapter 2 describes a scheme based on conformally mapping the flow domain to the upper half plane to eliminate velocity singularities, and solving with a Chebyshev spectral method. If a map from the physical domain (coordinates $z = x + \mathrm{i}y$) to a simpler computational domain (coordinates $Z = X + \mathrm{i}Y$) is known, then the problem can be solved in this computational domain. The open-domain solution of the inhomogeneous part of (1.3) (the direct contribution from the point vortices) is

$$\eta_{\mathrm{v}} = -\sum_{i=1}^{m} \frac{\Gamma_i}{2\pi} K_0 \left(\frac{|\boldsymbol{x} - \boldsymbol{x}_i|}{a} \right). \tag{3.2}$$

Under the mapping, the homogeneous part of (1.3) (which enforces the boundary conditions) becomes

$$\nabla_Z^2 \widetilde{\eta} - \frac{1}{a^2} \left| \frac{\partial z}{\partial Z} \right|^2 \widetilde{\eta} = 0, \tag{3.3}$$

where ∇_Z^2 denotes the Laplacian $\partial^2/\partial X^2 + \partial^2/\partial Y^2$. This can be solved in the computational domain and derivatives (and therefore velocities) can be found in the physical domain using the Jacobian $\partial(X, Y)/\partial(x, y)$, as in (2.17). The ordinary differential equations for the vortex positions are integrated either using standard Runge–Kutta schemes or the implicit timestepping scheme described in section 2.3.3.

3.3 Flow over a backward facing step – eddy formation in the California Undercurrent

Boundary currents such as the California Undercurrent are a ubiquitous feature in the oceans. The California Undercurrent is a northward flowing subsurface current extending 100 km from the coast, reaching speeds of more than 0.1 ms^{-1} between depths of 100 m and 400 m [Collins et al., 2000] and is part of a typical subtropical eastern boundary current. It develops a narrow strip of negative vorticity due to the turbulent bottom boundary layer and bottom stress. At several points along the coast this shear layer separates and the vorticity is ejected into the main flow, forming eddies. This can be seen in the numerical results of Molemaker et al. [2015] reproduced in fig. 3.1. Here the headland of Point Sur is the catalyst for the separation of the shear layer detaching from the coast. The shear is unstable and rolls up into a number of smaller eddies before being wound into a single large core of vorticity. These strong anticyclonic eddies, known as "cuddies", have been frequently observed in the region [Dewar et al., 2015]. Downstream of Point Sur there is a return flow along the coast which generates positive vorticity, seen in red in fig. 3.1. This shear layer is not as large or strong as it has had less time to develop and the return flow is weaker than the upstream current. A small eddy of positive circulation can be seen just past Point Sur in fig. 3.1. This could have been formed in a secondary separation of this positive vorticity layer, a common feature observed in separated flows. Both the 'height' of the backward facing step and the Rossby radius are around 30 km here [Chelton et al., 1998], giving a value of a of roughly unity. The California Undercurrent serves as an illustrative example of the formation of sheddies in a boundary current. In general the number of eddies formed may depend sensitively on details of the shape of the coastline which may be below the gridscale in some large scale models. Simple models thus have an important role in describing these local processes for global models.

To apply the QGBM model to the California Undercurrent at Point Sur the

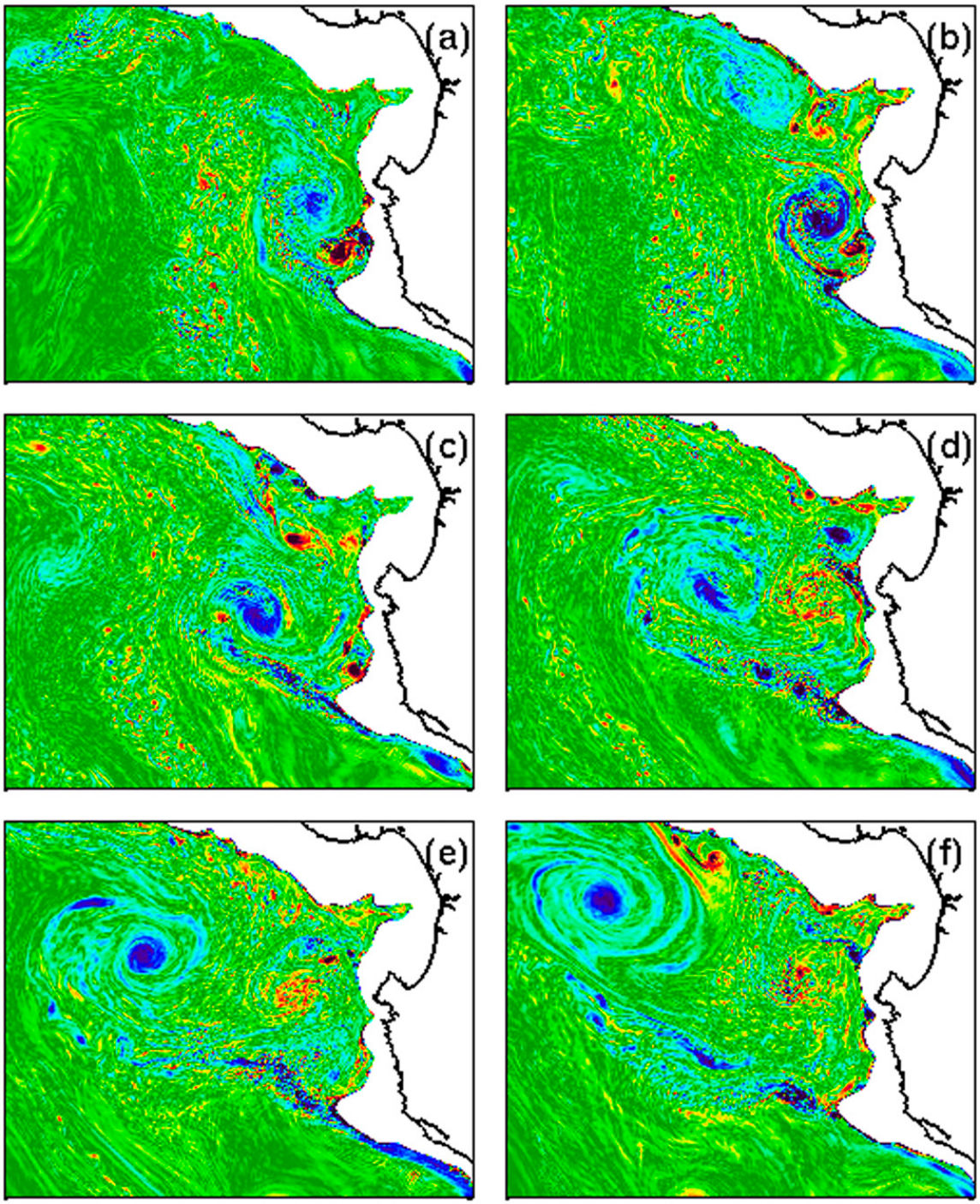

Figure 3.1: Normalised relative vorticity showing the evolution of the detached shear layer, its instabilities and roll up into a sheddy over the course of a month from the ROMS simulations of the California Undercurrent past Point Sur reproduced from Molemaker et al. [2015].

coastline is represented as a backward facing step formed by three sections of coast: $x_\mathrm{w} < 0$, $y_\mathrm{w} = 1$; $x_\mathrm{w} = 0$, $0 < y_\mathrm{w} < 1$; and $x_\mathrm{w} > 0$, $y_\mathrm{w} = 0$, with flow in $y > y_\mathrm{w}$, as can be seen in fig. 3.2 (which has been rotated for comparison with fig. 3.1). A suitable choice of mapping between this physical domain and a computational domain is

$$z = \frac{\sinh Z - Z}{\pi}, \tag{3.4}$$

which takes the three lines comprising the physical coast to the three sides of the semi-infinite strip $0 < X$, $-\pi < Y < 0$, which can then be truncated for computational purposes to a rectangle by choosing $0 < X < L_\mathrm{g}$. The truncation distance in the physical domain increases exponentially with L_g. Care must be taken near the corner at $(0, 1)$, which is mapped from an angle of $3\pi/2$ to $\pi/2$. Near the image of this point in the mapped domain

$$\eta \sim \text{const.} + cZ^2 + \mathcal{O}(Z^3). \tag{3.5}$$

The constant c is required to satisfy the Kutta condition but, unlike in chapter 2, cannot be found from the derivative of η at the origin: instead, the values of η near the origin must be used to find c, using the form (3.5). Since η is a streamfunction for the flow, a steady flow of flux Q can be set up by requiring that $\eta \to 0$ far from the boundary and that $\eta = Q$ on the boundary.

The results of a simulation in which (3.1) and (3.3) are solved to find the evolution of an eddy shed by a steady flow ($Q = 1$, $a = 1$) as it passes the corner of a backwards facing step are given in fig. 3.2, which shows the surface perturbation and shed vortex trajectory at four times. The centre of the eddy can be seen as the deepest surface depression, the depth of which grows over time, showing the increasing strength of the eddy. To show the path of the shed vorticity, passive tracers are continuously released and their positions are shown in the first two panels. These are streaklines for the flow and show the shed vorticity winding up around the vortex. The shed vortex initially grows and drifts downstream in a similar way to the sheddy in fig. 3.1. Over longer time the shed eddy slows and settles to a stationary state with a fixed location and constant circulation. Comparing figs. 3.1 and 3.2 shows that the QGBM model captures, at least qualitatively, the growth of the shed eddy.

The model allows discussion of the shedding of vorticity and its passage into

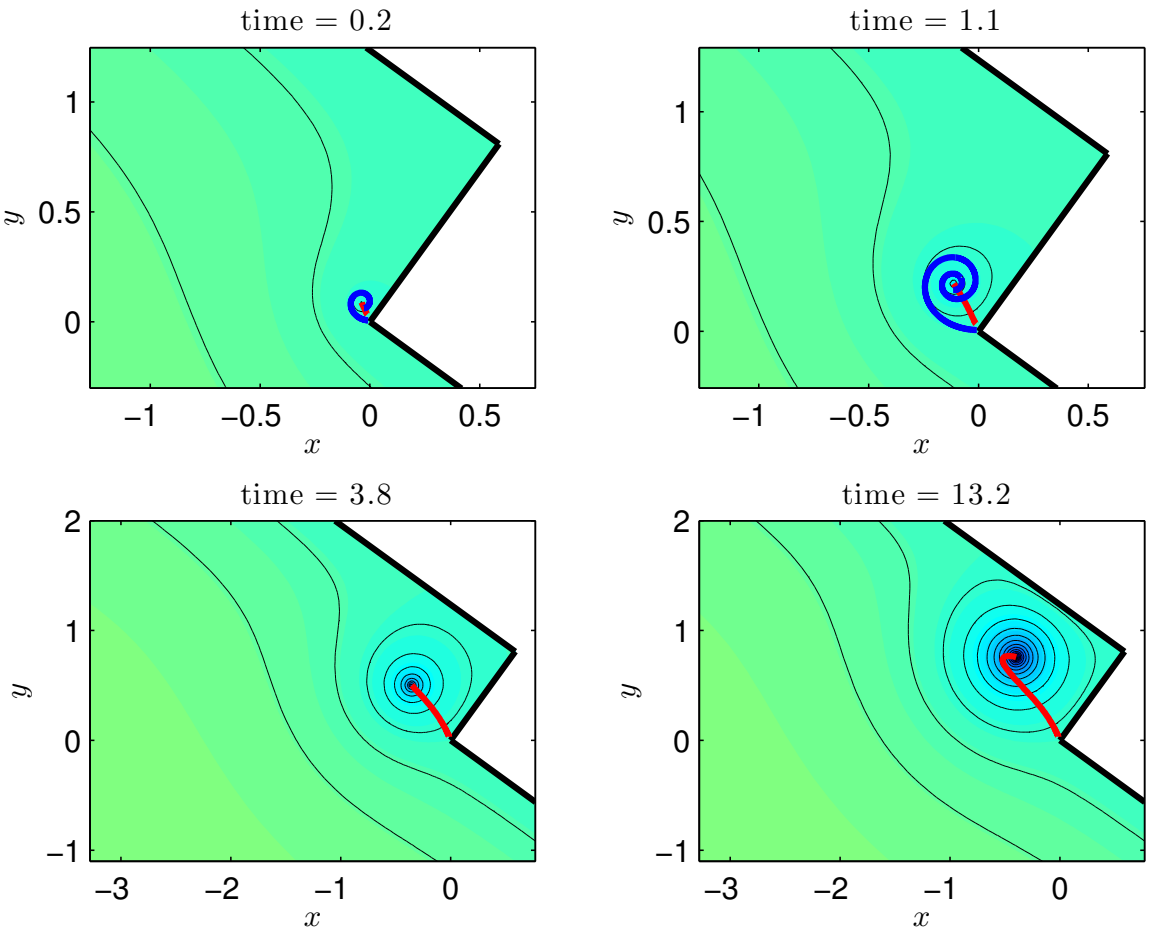

Figure 3.2: The surface perturbation from a QGBM simulation showing the evolution of a sheddy forming in the lee of a backward facing step. In this and all subsequent figures red and blue shows surface elevation and depression respectively. The black lines mark contours of the surface perturbation, which are streamlines for the flow and the vortex trajectory is shown in red. The first two panels show streaklines in blue showing the shed vorticity winding up into the vortex. In the final panel the eddy has evolved to a steady state with fixed location and constant circulation.

the shed vortex in terms of the various vorticity fluxes. Vorticity is held in the boundary layer, separates at the headland and rolls up into a core. The vorticity in the separated sheet has two contributing components. One component is negative vorticity held in the boundary layer at the edge of the oncoming flow. The other component is positive vorticity held in the edge of the recirculating current on the lee-side of the separation point.

The negative upstream vorticity and positive recirculation vorticity are shed at the separation point and begin to cancel through cross diffusion. Dewar et al. [2015] discuss the details of this process and the associated instabilities in the shed flow.

This process can be quantified in the QGBM model. Suppose that the boundary layer has thickness $\mathcal{O}(\delta)$ and a velocity profile $\boldsymbol{u}'_{\mathrm{I}}(x', y')$ matching an outer solution with speed $\boldsymbol{u}'(x', 0) = (U, 0)$ to zero velocity on the wall, where $\boldsymbol{x}' = (x', y')$ and $\boldsymbol{u}' = (u', v')$ are local coordinates and velocities tangential and normal to the wall respectively. As the layer is thin, the leading order vorticity in the layer is

$$\omega_{\mathrm{I}} = \frac{\partial u_{\mathrm{I}}}{\partial y} - \frac{\partial v_{\mathrm{I}}}{\partial x} \approx \frac{\partial u_{\mathrm{I}}}{\partial y}. \tag{3.6}$$

Therefore the flux of vorticity along the boundary layer is

$$\int_0^\delta \omega u_{\mathrm{I}} \,\mathrm{d}y' \approx \int_0^\delta \frac{\partial u_{\mathrm{I}}}{\partial y} u_{\mathrm{I}} \,\mathrm{d}y' \tag{3.7}$$

$$= \int_0^U u_{\mathrm{I}} \,\mathrm{d}u'_{\mathrm{I}} \; = \frac{U^2}{2}, \tag{3.8}$$

and depends only on the speed of the outer solution at the boundary. Thus the vorticity fluxes at the separation point can be obtained and related to the growth of the shed eddy. The rate of change of sheddy circulation and the upstream, recirculation and net vorticity fluxes are shown in fig. 3.3. The boundary layer vorticity fluxes are evaluated away from the separation point as the velocity vanishes there. For the recirculation vorticity flux the average of the vorticity fluxes from the reattachment point (the point where $v(0, y) = 0$) to the separation point is used and for the upstream vorticity flux the far upstream values are used. Equation (3.8) models a shear layer that is quasi-steady, which in the early stages of the evolution here may not be the case. Initially the recirculation flux may carry negative vorticity formed at

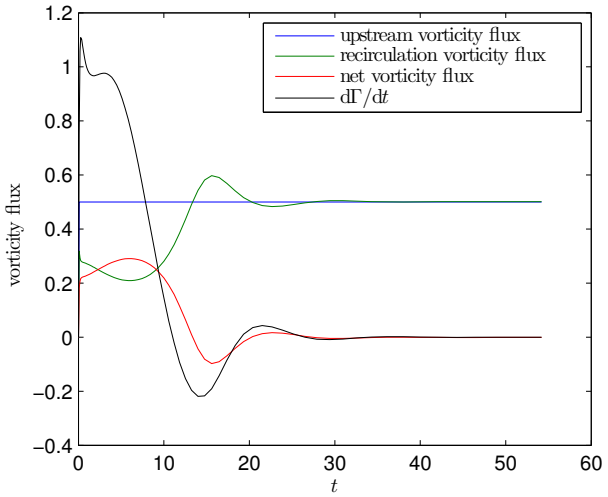

Figure 3.3: The evolution of vorticity fluxes at the separation point and shed vortex for a QGBM simulation of a sheddy forming in the lee of a backward facing step.

earlier times back to the separation point.

Figure 3.3 shows that once the sheddy has evolved to its steady state, the vorticity fluxes balance perfectly: the fluxes of negative vorticity from upstream and positive recirculation vorticity are equal and opposite so the shed vortex grows no further. Earlier on in the evolution of the vortex the increase in vortex circulation and the net vorticity flux follow the same pattern qualitatively but do not match exactly. As noted above, for early times the quasi-steady layer formulation of (3.8) may not be appropriate. Taking the vorticity in the recirculation shear layer at early times to be the upstream value of $-1/\delta$ gives an initial net vorticity flux of approximately 0.9, close to the rate of change of sheddy circulation of approximately 1.

It appears that the QGBM model accurately represents the separated flow over a stepped coastline. Comparing the results here to simulations of the California Undercurrent [Molemaker et al., 2015] shows a strong qualitative resemblance in the shedding of the shear layer and its roll up into a concentrated core, although the QGBM model doesn't explicitly represent all the details present in the ROMS simulations, for example the small-scale instabilities. At later times the fluxes of vorticity come into balance, the sheddy settles to a steady position and ceases to grow in strength. This steady state suggests that it may be possible to have an area of high vorticity trapped on the leeward side of a stepped coastline.

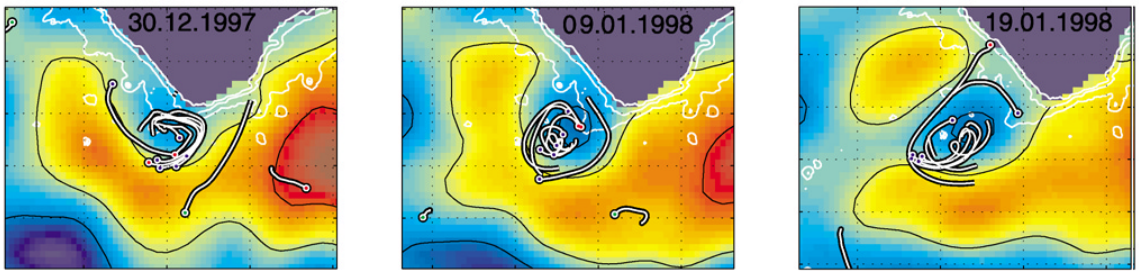

Figure 3.4: An Agulhas cyclone shown in sea surface height data from MODAS-2D. Trajectories of several RAFOS floats are shown in white with circles denoting their initial positions. Reproduced from Lutjeharms et al. [2003].

3.4 Flow around a cape - Agulhas Cyclones

The Agulhas current is an intense western boundary current carrying a flux of 70 Sv (1 Sv = $10^6\,\mathrm{m^3 s^{-1}}$) southwest along the east coast of Africa. As the Agulhas enters the south Atlantic, interaction with the Antarctic Circumpolar Current forces it to bend and flow eastward: the Agulhas Retroflection. This retroflection is unstable and periodically produces large anticyclonic eddies known as the Agulhas Rings. Transport by these eddies is the main mechanism of inter-ocean exchange between the Indian and South Atlantic oceans, with estimates of their flux typically of the order of 10 Sv. They are a significant source of salt and heat in the South Atlantic Gyre.

Although the large scale behaviour is well documented, many details contribute to the inter ocean exchange between the Indian and Atlantic oceans [Boebel et al., 2003]. For example, cyclonic eddies formed by separation in the lee of the Agulhas Bank are found in both observational [Lutjeharms et al., 2003] and numerical [Penven et al., 2001] studies. Figure 3.4 shows one of these eddies observed in satellite sea surface height data from Lutjeharms et al. [2003] who note that these eddies are often important in the formation of the larger, anticyclonic Agulhas Rings.

The initial growth of an Agulhas Cyclone is modelled here as a representative example of an eddy formed from a detached flow at a cape. The Agulhas Bank is represented as a right-angled wedge (the solution for arbitrary angle follows similarly). The current is taken to be a simple steady westward flow around the cape tip of flux Q, imposed with the boundary conditions $\eta = Q$ on the coast and $\eta \to 0$

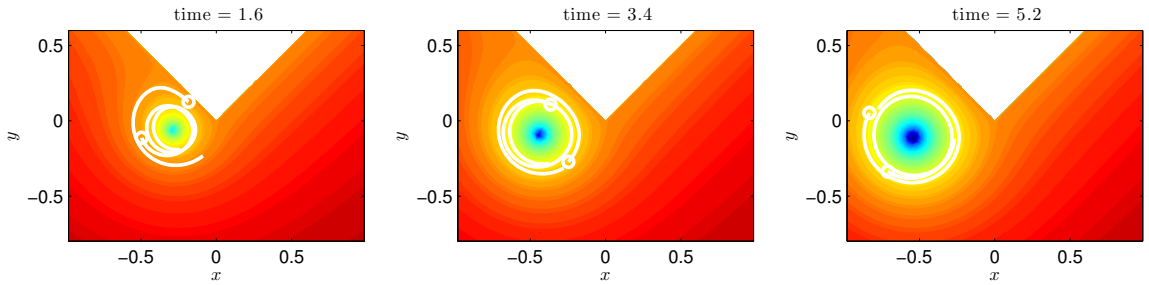

Figure 3.5: The surface perturbation for a QGBM vortex growing from the tip of a right-angled wedge at three times for $Q = 1$, $a = 1$. Trajectories of two passive marker floats are shown in white with circles denoting their initial positions.

far from it, similarly to section 2.4.3. The results of this simulation with $Q = 1$ are shown in fig. 3.5. Here the Rossby radius L_R can be used as the lengthscale L so all solutions are a rescaling of the $a = 1$ solution. The surface height is displayed at three times and the trajectories of two passive markers are included. The marker trajectories over each time period are shown as white lines with a white circle indicating their initial position. The eddy drifts away from the coast as it grows on the leeward side of the bank. Both the evolving location and increasing strength of this eddy bear strong qualitative resemblance to the observations shown in fig. 3.4. The paths of the passive tracers in figs. 3.4 and 3.5 also appear qualitatively similar, suggesting that passively advected particles around a growing shed vortex may be a good model for the dynamics of these buoys even though the point vortex simulations cannot capture the full variability present in fig. 3.4.

3.5 Flow through a gap

3.5.1 Unidirectional flow through a gap - the Cook Strait

The two largest islands of New Zealand form a 1400 km north-south barrier to the prevailing winds and currents. The only gap in this barrier is Greater Cook Strait, just 24 km across at its narrowest point. As Walters et al. [2010] note, the flow in the Greater Cook Strait region is complex with many influencing factors: the meeting of several currents; complex and dramatic topography and bathymetry; wind forcing;

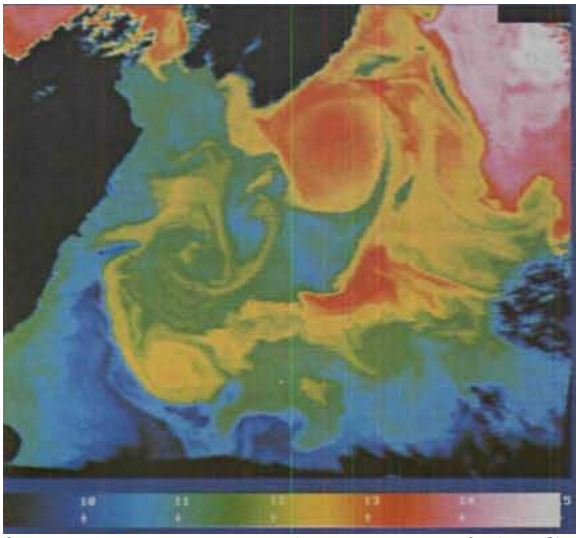

Figure 3.6: Sea surface temperature in the vicinity of the Cook Strait reproduced from Barnes [1985].

tidal stresses; density variations; sea level differences and river discharges. Different factors dominate in different areas of the strait and so building a full understanding of the currents in the region requires piecing together many factors.

Walters et al. [2010] performed a comprehensive study of the region by combining current and wind data with an unstructured-grid model including accurate topography to examine the leading mechanisms across Greater Cook Strait. By running their model with, and without, several of the important forcing factors they were able to estimate the significance of these factors in different areas. The model of Walters et al. [2010] shows flow separation at the northern edge of Cook Strait forced by the eastward flux through the gap with their fig. 7 showing residual currents along the northern side of Cook Strait, just to the west of Cape Palliser and Palliser Bay. As the flow passes Baring Head the surface velocities intensify and the current detaches. A recirculating current can be seen on the downstream side of the head showing that flow separation occurs here.

One of the most striking observed features in the area is a large warm core eddy to the East of the strait, as shown in figure 3.6 (from Barnes [1985]). This eddy appears to be a stable feature fixed in position even though there is no obvious explanatory bathymetric feature. The origin of this eddy and the reason for its apparent stability are not known but it is suggested here that the eddy is formed as the current through the strait separates at Cape Palliser, on the northern edge of the gap.

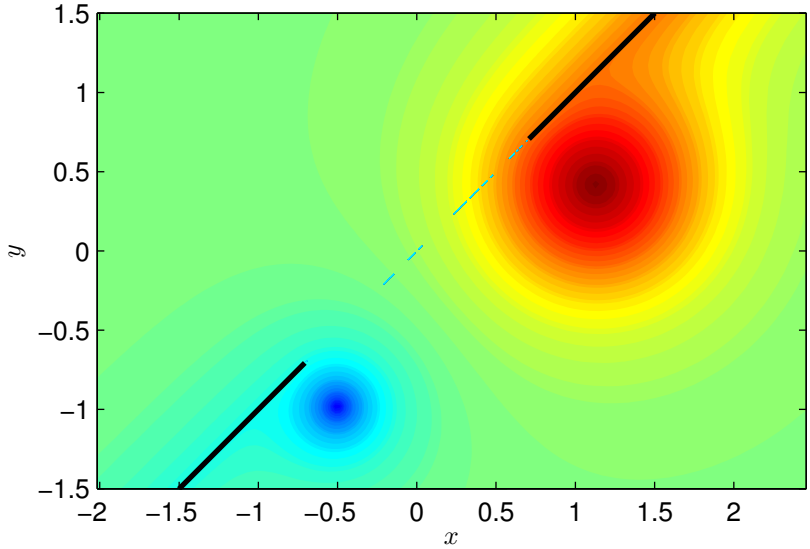

Figure 3.7: The surface perturbation for QGBM vortices shed from the edges of a gap for $a = 0.4$ at time $t = 4$ in the simulation. There is unit flux along the upper wall and flux of $1/3$ along the lower wall.

The volumetric flux through the strait is approximately 0.6 Sv which dominates the residual currents, although tidal stresses are also important around headlands. The currents concentrate on the northern side as they pass through the strait. The Cook Strait is thus modelled here as a gap in a wall representing the North and South Islands with a flux through the gap of strength $Q_2 + Q_1$ where Q_1 is the flux northward up the west coast of the South Island and Q_2 is the flux southward down the west coast of the North Island, given by applying the boundary conditions $\eta = Q_1$ on the lower wall, $\eta = Q_2$ on the upper wall and $\eta \to 0$ at infinity. The strengthening of the current on the northern side of the strait is modelled by taking $Q_1 < Q_2$. Here, the parameter $a = L_\mathrm{R}/L$ is the ratio of the Rossby Radius L_R to the gap half-width L, which is used as the non-dimensional lengthscale in all the gap problems here. Two sheddies are formed, one from either edge of the gap. The streamfunction can be computed numerically using the spectral method described in chapter 2 and the mapping

$$z = \cosh Z, \tag{3.9}$$

which takes the strip $0 < Y < \pi$ in the computational domain (coordinates $Z = X + \mathrm{i}Y$) to the physical domain (coordinates $z = x + \mathrm{i}y$) with the top and bottom boundaries of the strip mapping to the left and right walls respectively.

The width of the gap where the eddy is formed is approximately 125 km and the Rossby Radius is around 25 km [Chelton et al., 1998] giving $a = 0.4$. Figure 3.7 shows the surface height from a simulation with this value of a, $Q_2 = 1$ and $Q_1 = 1/3$ at time $t = 4$. Two shed eddies of opposite signed circulations are clearly visible with a much larger eddy on the northern edge of the strait, matching well with the observations in fig. 3.6. As discussed in section 2.4.1 (see figs. 2.4 and 2.5) after an initial period, QGBM vortices grow slowly, particularly when a is small. This slow growth could be an explanation for the unchanging position of the observed Cook Strait eddy.

This eddy formation mechanism could cause eddies to form anywhere where there is significant flow through a gap. In many places the dynamics are complicated however by other factors. It is often the case that there are significant differences in important properties such as sea surface height, ocean depth or salinity across gaps. These differences can also provide a mechanism for the formation of eddies such as Mediterranean outflow eddies "meddies" [Serra et al., 2005] and Indonesian throughflow eddies "teddies" [Nof et al., 2002].

3.5.2 Eddies encountering gaps - the interaction of North Brazil Current Rings with the Lesser Antilles

There are many examples of eddies encountering either single gaps in topography, such as Caribbean cyclones entering the Yucatan Channel [Richardson, 2005], or multiple gaps, such as meddies encountering an underwater ridge [Dewar, 2002] with the eddy trajectory differing significantly depending on whether it passes through or across the gap. The dynamics of this process are sensitive to the details of the local topography and bathymetry and, as these details may not be sufficiently resolved in large scale ocean models, have been the focus of much attention.

A particularly important example concerns the fate of the North Brazil Current (NBC) rings. As the NBC retroflects, large eddies (known as the NBC rings) are periodically shed at the rate of 6-9 per year with each eddy carrying a flux of around 1 Sv [Goni and Johns, 2001]. The large size of the NBC rings and their shedding

frequency represents a significant transport mechanism of warm South Atlantic surface water into the Northern Hemisphere. They travel northwest until they meet the island chain of the Lesser Antilles which blocks their path.

Whether the NBC rings pass through gaps between the Lesser Antilles, disintegrate upon collision with the islands or continue northward past them is of key interest. Some observations suggest that they rarely pass through the southern Lesser Antilles intact [Johns et al., 2003] but that in many cases they may disintegrate with their mass passing through the gaps and into the Caribbean sea [Fratantoni and Glickson, 2002, Fratantoni and Richardson, 2006]. It may be possible for NBC rings to enter through the northern Lesser Antilles as "quasi-coherent" structures [Gómez and Bulgakov, 2007]. Additionally, drifter studies suggest that anticyclones to the west of the Lesser Antilles may be formed from NBC ring anticyclonic vorticity [Richardson, 2005]. However, in some numerical simulations [Garraffo et al., 2003] the NBC rings enter the Caribbean nearly intact.

Simmons and Nof [2002] present an analytical model and numerical results which suggest that weak eddies are able to squeeze through the gaps but that intense eddies resist. The circulation around the islands in their numerical experiments increased due to flow separation at the island edges, which has also been observed in experimental investigations. Duran-Matute and Velasco Fuentes [2008] performed experiments on an eddy encountering a gap and observed eddies formed by flow separation interacting with the incident eddy. This caused a looping trajectory, differing from their otherwise effective point vortex theory, as shown in fig. 3.8 which combines their figs. 13 and 14. Tanabe and Cenedese [2008] also observed eddies forming from separated flow in the lee of the islands in their experiments, which investigated an eddy passing a chain of circular islands.

Point vortex models of eddies approaching a gap have been useful in understanding the dynamics of the situation and give precise criteria for whether an eddy will pass through or leap over a gap, depending on the background flow and the eddy's initial distance from the wall [Johnson and McDonald, 2005b, Nilawar et al., 2012]. These models do not, however, allow flow separation. This section reconsiders a point vortex encountering a gap in a wall, modelling flow separation with the QGBM

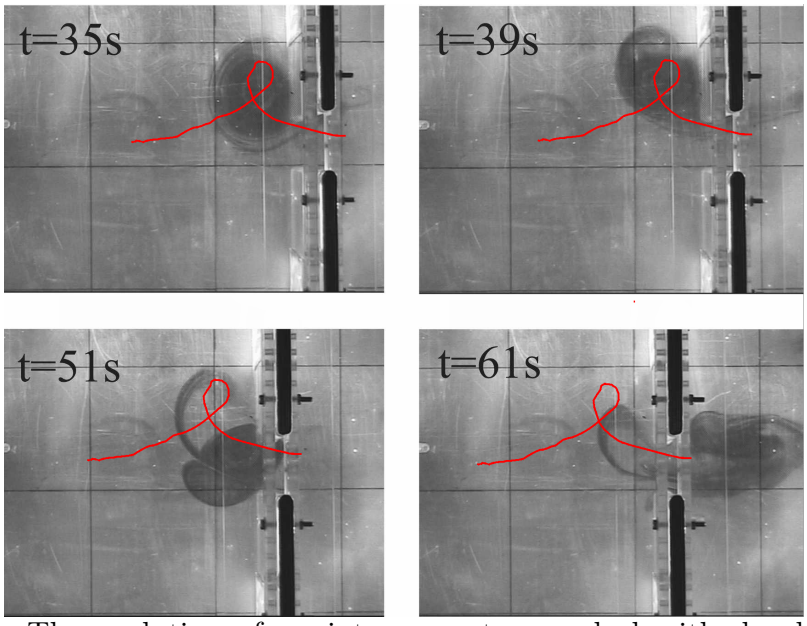

Figure 3.8: The evolution of an intense vortex marked with dye being driven through gap in a wall by a current in a rotating tank experiment reproduced from Duran-Matute and Velasco Fuentes [2008]. The red line shows the trajectory of the centre of the incident vortex.

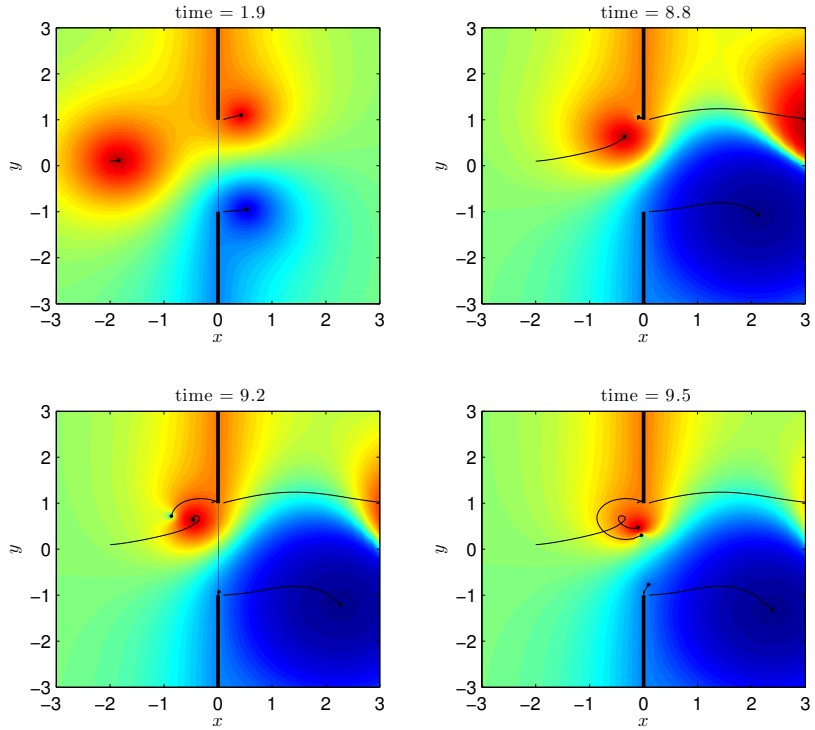

Figure 3.9: The surface perturbation and vortex trajectories (black lines) for a simulation of a vortex being driven through a gap by a current in a similar arrangement to fig. 3.8. The incident vortex has strength $\Gamma = 10$, $a = 1$ and the flux through the gap is $Q = 2$.

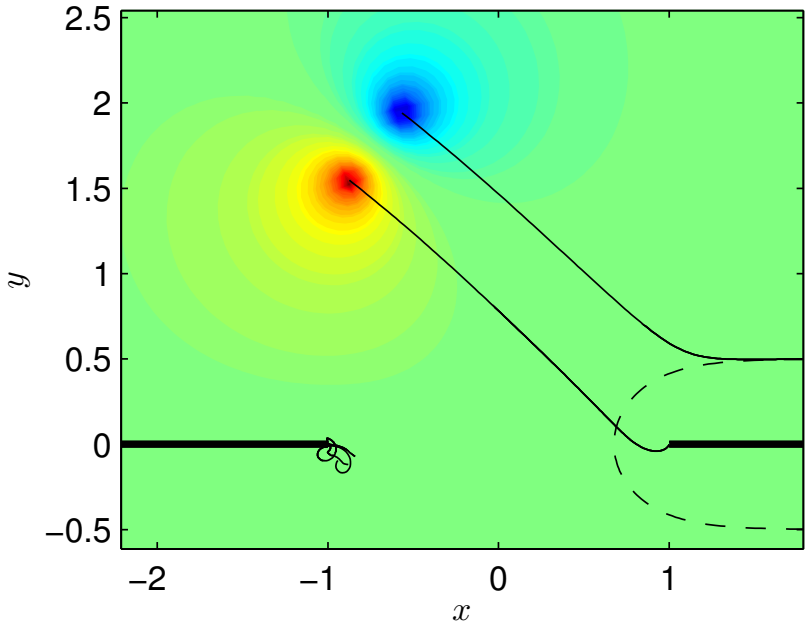

Figure 3.10: Vortex trajectories for an incident vortex with no background flow without shedding (dashed line) and with shedding (solid lines). The colour shows the surface perturbation at the final time in the simulation with shedding. The incident vortex is initially a distance of 1/2 from the wall and $a = 1$.

model.

Consider first the situation with no background flow ($\eta = 0$ on the walls, $\eta \to 0$ far from the walls) and a point vortex approaching the gap from an initial position (x_0, y_0), where $x_0 \gg a$ and the initial distance from the wall y_0 is varied. In the absence of flow separation there is a critical value of y_0, depending on a, above which vortices leap the gap, and below which they pass through. When flow separation is included, very different results are found. For no values of y_0 or a does the vortex pass through the gap. A typical scenario where, in the absence of shedding, a vortex would have passed through is shown in fig. 3.10. Here the sheddy from the near wall pairs with the incident vortex and prevents it from entering the gap with the pair ultimately propagating away. Very little vorticity is generated at the far tip. The result that vortices can no longer self-advect through a gap relates to those of section 2.4.2 where, for a similar situation with a single plate instead of a gap, it was found that, for all a, the incident vortex and shed vortex paired up and moved away in the upper half plane without rounding the plate tip.

The NBC rings are aided in passing through gaps by the presence of a background flow. Considering the previous scenario but with an additional unidirectional flow

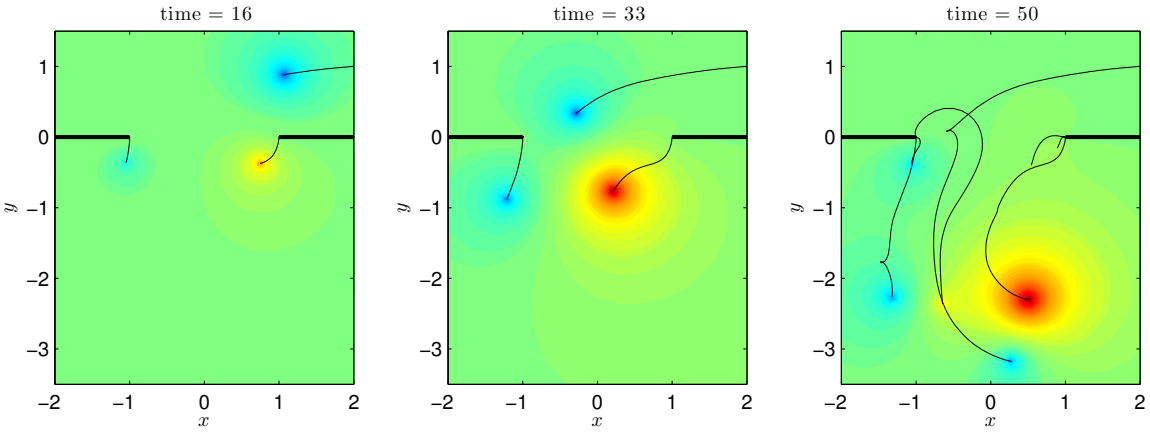

Figure 3.11: Vortex trajectories for an incident vortex with a background flow of strength $Q = 0.2$. The colour shows the surface perturbation at the final time in the simulation. The parameter $a = 1$ and the incident vortex is initially a distance $y_0 = 1/2$ from the wall.

through the gap of flux Q, achieved with the conditions $\eta = Q/2$ on the left wall, $\eta = -Q/2$ on the right and $\eta \to 0$ far from the walls, shows that, for flux Q above a certain critical value the current overpowers the resistance of the vortex and advects it through the gap. Typically a current of flux $Q = 0.2$ was able to overpower a vortex with unit circulation. This example is shown in fig. 3.11. Here, a significant amount of vorticity is generated from both edges of the gap, driven by the unidirectional background current.

The experiments of Duran-Matute and Velasco Fuentes [2008] offer a good test of the QGBM method in this single-gap geometry. They found good agreement between point vortex methods and their experiments until the generation of vorticity at the walls became significant. Figure 3.8 shows the results of one of their experiments for a more intense vortex (combining their figures 13 and 14). As the incident vortex approaches the gap, vorticity is shed from the nearest edge. This shed vortex pairs up with the incident vortex and they perform one spiral before passing through the gap. The red line shows the trajectory of the centre of the incident vortex which is visualised with dye in the experiment.

The results of a QGBM simulation with the incident vortex starting at $(x_0, y_0) = (-2, 0)$, with $\Gamma = 10$, $a = 1$ and $Q = 2$ as a typical example, although the same qualitative behaviour is shown for other values of a, are shown in fig. 3.9. The colouring in fig. 3.9 indicates the surface perturbation and so is not directly comparable with the dye in fig. 3.8. In fig. 3.9 the incoming vortex induces the separation and

formation of a sheddy of oppositely signed vorticity on the upper wall. The two vortices pair and perform a single loop before passing through the gap, similar to the behaviour observed in the experiments. The simulations in fig. 3.9 are typical, with this behaviour appearing to be robust across a range of parameters. In the simulation the throughflow also generates eddies at both edges of the gap. As there was no dye injected in these regions in the experiment it does not appear possible to decide whether these vortices were present in the experiments. The QGBM model appears to capture the main features found in these experiments very well and supports the suggestions that a sheddy formed at the gap edge and interacted with the incident vortex, offering a significant improvement to the non-separating point vortex models. The effect of the separated shear layer may explain the reluctance of the NBC rings to pass through gaps and the large number of eddies observed to the west of the islands.

3.5.3 Unidirectional flow through a gap - the Canary Eddy Corridor

The Canary Current is a wind-driven eastern boundary current flowing southwestward along the western coast of Africa as far as Senegal. Sheddies are generated continually in the lee of the Canary Islands, which form a partial barrier across the current [Barton, 2001, Sangrà et al., 2007]. Fig. 3 of Barton [2001] shows multiple sheddies visible in the sea surface temperature and his fig. 4 shows the looping profile of a drifter trapped in a sheddy. These eddies form a long chain known as the Canary Eddy Corridor [Sangrà et al., 2009] and may form the origin for swesties (shallow subtropical subducting westward propagating eddies) [Pingree, 1996].

Here, sheddies formed in the wakes of gaps between islands are modelled. Consider a single gap in a wall with a symmetric unidirectional current of flux Q through the gap, given by setting $\eta = Q/2$ on one wall, $\eta = -Q/2$ on the other and $\eta \to 0$ at large distances.

The original Brown–Michael model has no mechanism for curtailing the growth of a sheddy: as the separated shear layer rolls up, the eddy grows monotonically and typically drifts downstream. In real flows, as the eddy grows, factors like instabilities

in the shear layer become more important and eventually destroy the vortex sheet, stopping the growth of the sheddy and freeing the shear layer to roll up into a new shed eddy. To represent this process a condition is added here determining when a sheddy stops growing and a new sheddy forms.

For outflows shed vortices tend to form pairs [Blondeaux and De Bernardinis, 1983]. Thus one appropriate choice of termination condition is to halt the growth of an eddy when the distance between the vortex and the separation point, an estimate of the length of the vortex sheet, is longer than the distance to the nearest vortex. The eddies then form a pair with their circulations fixed and move away freely with new sheddies forming at the gap.

Figure 3.12 shows a simulation with this condition, $a = 1$ and a unidirectional background current through the gap of flux $Q = 1$. Vortex pairs are shed regularly and periodically with shedding frequency of approximately 0.2 (8 eddies are formed over a timespan of length 40), giving a Strouhal number (defined as $S_\mathrm{t} = nL/U$ for shedding frequency n, lengthscale $L = a$ and velocity scale $U = 1/a$) of $S_\mathrm{t} \approx 0.2$. This value is consistent with the results of Dong et al. [2007] and the standard Von Karman vortex street for non-rotating non-stratified two-dimensional flow past an object. The first four panels of fig. 3.12 show the evolution of a pair of sheddies over their formation period up to the point where their feeding vortex sheets have collapsed and a new pair of sheddies have started growing. The fifth pane gives a larger scale view over longer time to show the periodic shedding.

Although this criteria gives realistic results, and is the closest to reality in this case, other choices are possible. An alternative would be to set a maximum feasible circulation for the vortex Γ_max. Varying Γ_max gives a continuum of models with the original Brown–Michael corresponding to $\Gamma_\mathrm{max} \to \infty$ and a vortex sheet model given by $\Gamma_\mathrm{max} \to 0$. Figures 3.13 and 3.14 show examples using $\Gamma_\mathrm{max} = 2$ and $\Gamma_\mathrm{max} = 25$ with $a = 1$ and $Q = 1$. In both cases many sheddies are generated. For $\Gamma_\mathrm{max} = 2$, the growing sheddy is frequently pulled back towards the separation point by another eddy. causing its circulation to decrease and a new sheddy to form leading to the generation of a large number of vortices, some of which have very small circulations. These many smaller eddies concentrate into an area resembling a single larger eddy, perhaps modelling the small eddies formed from instabilities of figs. 1.1 and 3.1.

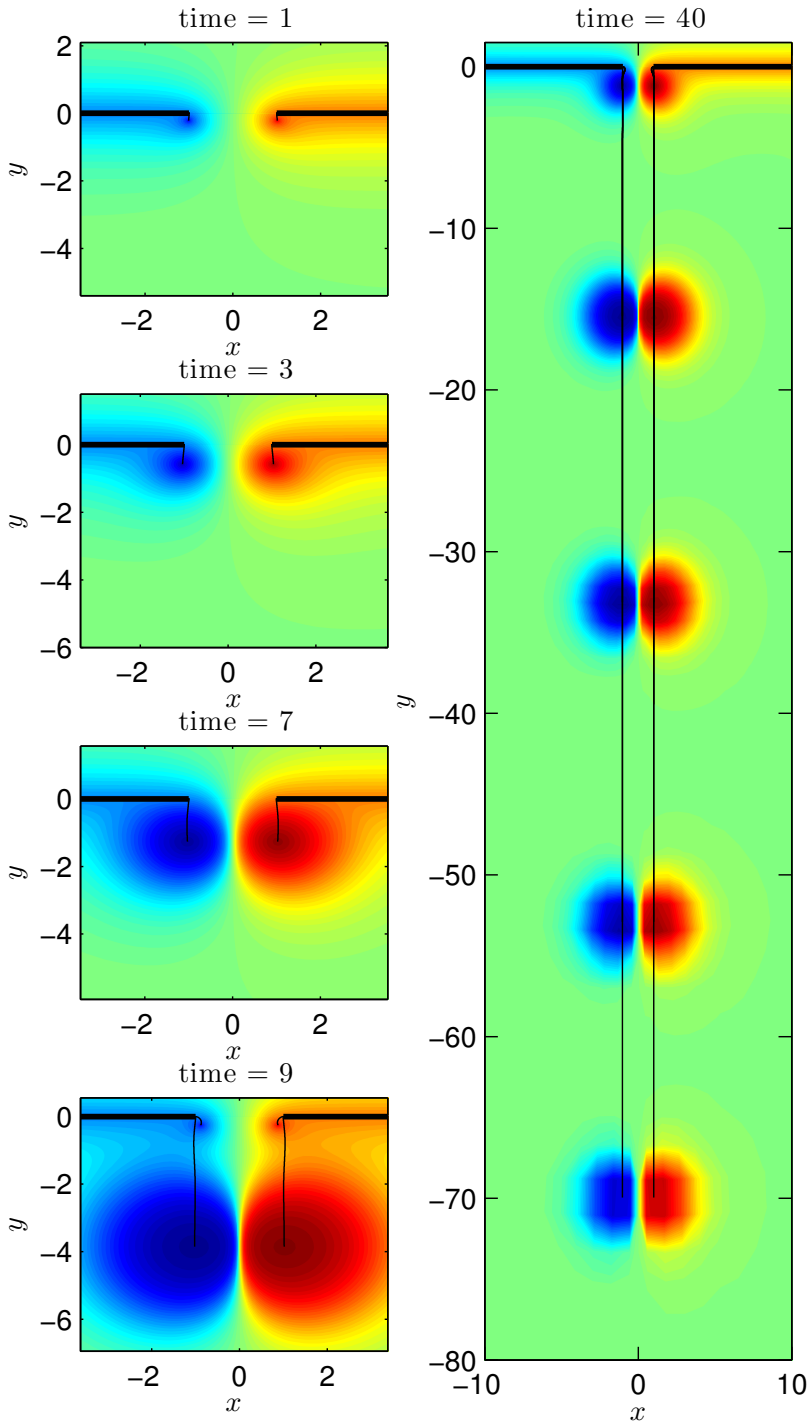

Figure 3.12: The surface perturbation from a QGBM simulation of a current through a gap of flux $Q = 1$ driving the formation of shed eddies for $a = 1$. The four snapshots on the left span the growth period of a pair of sheddies from their genesis until they are set free and new sheddies begin to form. The panel on the right shows a larger scale view after a longer period of time to show the periodic behaviour. The trajectories of the centres of the eddies are marked as black lines.

The $\Gamma_{\max} = 25$ condition gives dynamics somewhere between the clustered, many-vortex shedding of $\Gamma_{\max} = 2$ (fig. 3.13) and the regular periodic shedding of the condition on the vortex sheet lengths (fig. 3.12). Several distinct, strong sheddies are formed but these are close enough that the nonlinear interactions between them cause complex spiral trajectories and leapfrogging of eddies past eddies shed at earlier times.

Although the results of the simulation of fig. 3.13 appear significantly different from those of fig. 3.12, the centre of vorticity follows a very similar path for small and moderate times. A many-vortex simulation like this becomes more computationally intensive as the number of vortices grow and is significantly more difficult to interpret than a standard Brown–Michael simulation. Using a condition such as $\Gamma_{\max} = 2$ is sacrificing some of the key advantages of the QGBM method. This, the similar evolution of the centres of vorticity and the good qualitative agreement (for example on the Strouhal number) suggests that the condition based on vortex sheet length is a superior choice. These simulations provide a good qualitative representation of the formation of sheddies from the Canary Islands.

3.6 Conclusions

The model has been applied to observations, numerical experiments and experimental results in a number of oceanographic situations: the Canary Eddy Corridor, Agulhas Cyclones, Cook Strait throughflow, California Current at Point Sur and the collision of the North Brazil Current rings with the Lesser Antilles. Comparison between sea surface height data showing the formation of an Agulhas Cyclone and the results of a QGBM simulation suggests that the model captures the growth of the shed eddy. Rotating tank experiments investigating a vortex advected through a gap show trajectories significantly affected by flow separation as a shed eddy pairs with the vortex and causes a looping trajectory, a result robustly reproduced by the QGBM model.

Non-separating point vortex models of the North Brazil Current rings colliding with the Lesser Antilles do not capture the reluctance of these rings to pass between island gaps. The QGBM model, which allows flow separation, shows that eddies

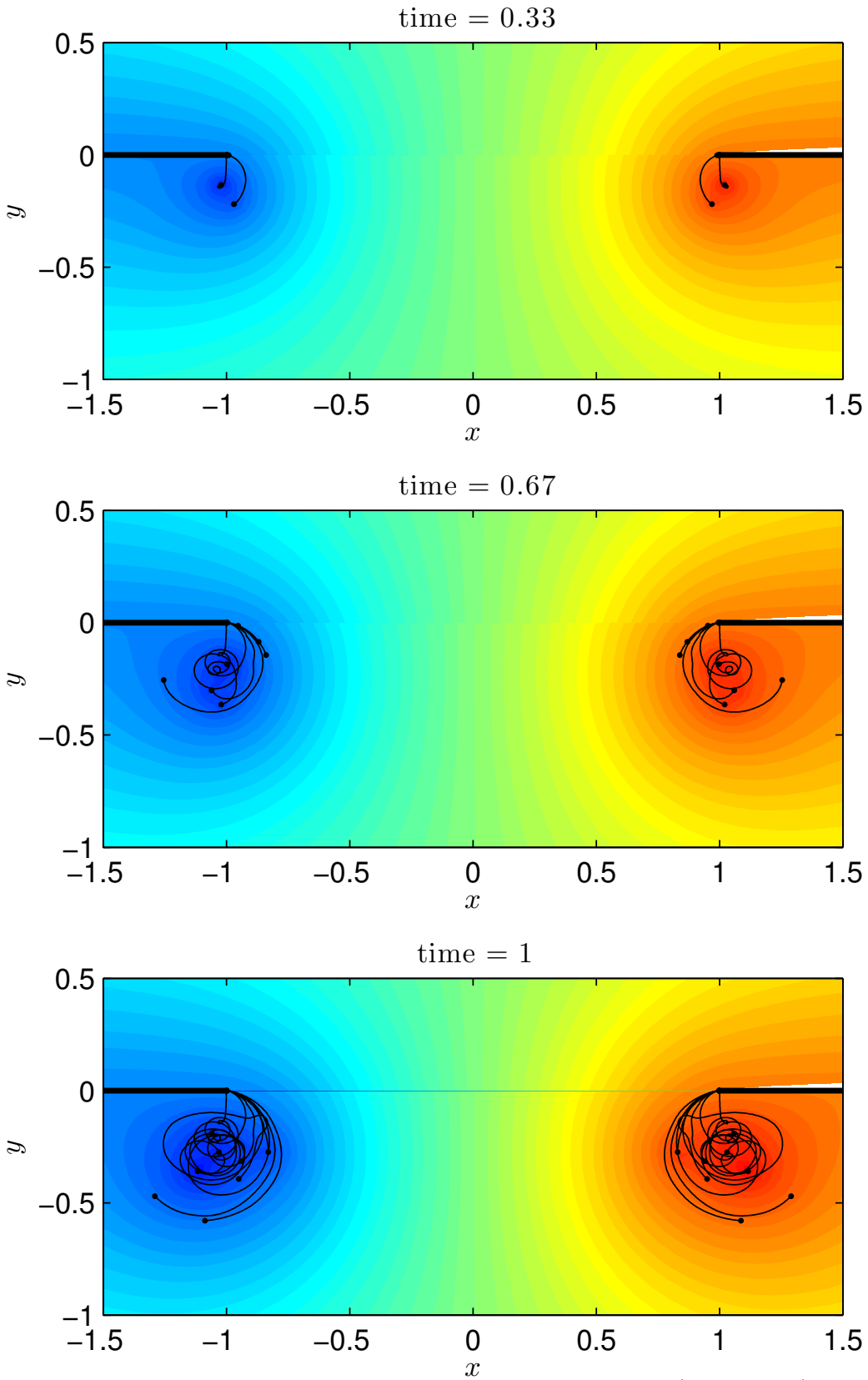

Figure 3.13: The surface perturbation and sheddy trajectories (black lines) at three points in time from a simulation of sheddies formed from a current of flux $Q = 1$ passing through a gap for $a = 1$ and with the condition that the magnitude of the sheddy circulation cannot exceed $\Gamma_{\max} = 2$.

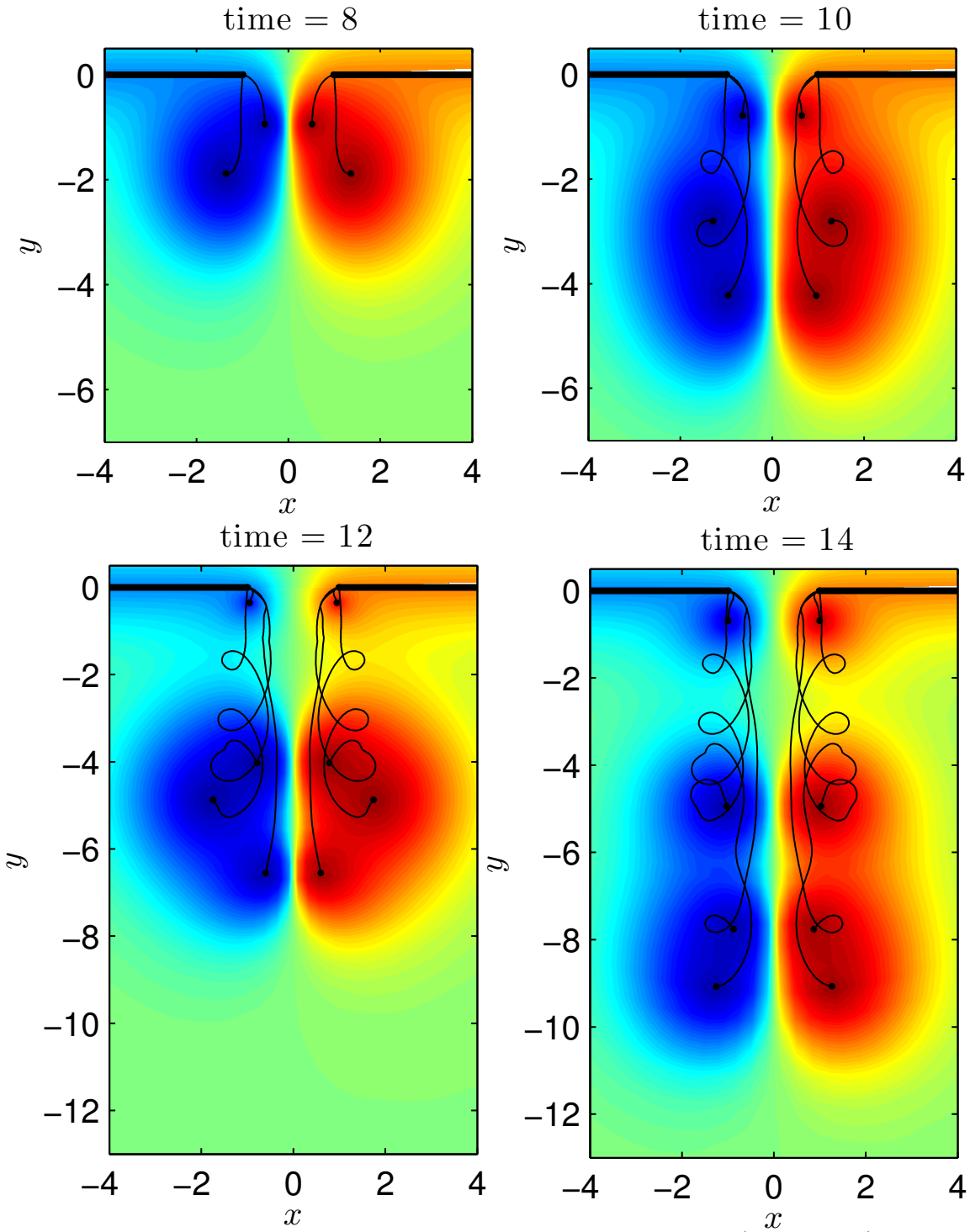

Figure 3.14: The surface perturbation and sheddy trajectories (black lines) at four points in time from a simulation of sheddies formed from a current of flux $Q = 1$ passing through a gap for $a = 1$ and with the condition that the magnitude of the sheddy circulation cannot exceed $\Gamma_{\max} = 25$.

are far less likely to pass through the island gaps. The vorticity expelled by flow separation may thus be an important reason why North Brazil Current rings do not often enter the Caribbean intact.

Chapter 4

A quasigeostrophic model of coastal outflows

This chapter presents a simple model of coastal outflows consisting of a source along an infinite wall expelling constant potential vorticity fluid into an initially quiescent $1\frac{1}{2}$-layer quasigeostrophic ocean. This captures the key balance between the rotation-modified source velocity and the generation of vorticity as the buoyant outflow fluid adjusts. Section 4.1 describes the model. In section 4.2 a long wave approximation for outflows that vary gradually in the alongshore direction is used to derive analytical expressions for steady outflow boundary profiles for an arbitrary source velocity profile. Section 4.3 uses the long wave approximation to derive analytical solutions describing the full unsteady evolution of the outflow for two example problems: a point source outflow and a uniform outflow. In section 4.4 these analytical solutions are compared to contour dynamics simulations, again for point and uniform source outflows.

4.1 Quasigeostrophic model of a coastal outflow

The coast is modelled as a straight wall along the x-axis and the river mouth as a source discharging fluid into an initially quiescent ocean occupying the upper half plane $y > 0$. The source water is relatively lighter than the lower layer of the ambient

so adjusts quickly to a constant unperturbed depth D, where $|D - D_\mathrm{s}|/D \ll 1$. The upper layer has the source density ρ_1 and the lower layer has the density $\rho_2 > \rho_1$. Let the source lie between $x = -L$ and $x = L$ and have depth D_s and volume flux $Q_0 D$, giving an area flux, once adjusted, of Q_0, hereafter simply referred to as the flux. To conserve potential vorticity (PV) as the expelled fluid adjusts, the squashing of vortex columns generates relative vorticity Π which is constant, and positive if $D_\mathrm{s} < D$ or negative if $D_\mathrm{s} > D$. The unperturbed depth of the outflow D is constant so the perturbation PV Π/D is proportional to the generated relative vorticity Π and is constant, but takes the sign of Π so may be positive or negative. Low Rossby number flows are considered here and the river depth is assumed constant so the PV in the river is constant and equal to f_0/D_s. Here, small density differences are considered, so the outflow adjusts and is taken to gain the perturbation PV Π/D instantaneously. Schematics of this set-up are shown in fig. 4.1. This mechanism is taken as an illustrative example of the dynamics of coastal outflows. Here, the focus is on outflows where the dynamics are forced by the generation of vorticity as the outflow fluid adjusts. The source fluid may have additional relative vorticity but this is taken to be weaker than the generated vorticity for the wide, gradual outflows considered here.

Coastal outflows are typically large scale but shallow features. This work considers outflows without significant inertia (i.e. small Rossby number) over long periods so an appropriate model is that of $1\frac{1}{2}$-layer QG flow, as described in section 1.3, except that in this and the following chapter the equations are left in fully dimensional form. Here the streamfunction is η but, as this is in dimensional variables here, this is only proportional to the surface displacement, not equal to it. If the interface perturbation is h, then $\eta = g'h/f$ and

$$\boldsymbol{u} = \left(-\frac{\partial \eta}{\partial y}, \frac{\partial \eta}{\partial x} \right). \tag{4.1}$$

The dimensional quasigeostrophic PV is $(\nabla^2 \eta - \eta/L_\mathrm{R}^2)/D$. Conservation of PV is again given by

$$\frac{\mathrm{D}}{\mathrm{D}t} \left(\nabla^2 \eta - \frac{1}{L_\mathrm{R}^2} \eta \right) = 0, \tag{4.2}$$

where $\mathrm{D}/\mathrm{D}t$ is the material derivative.

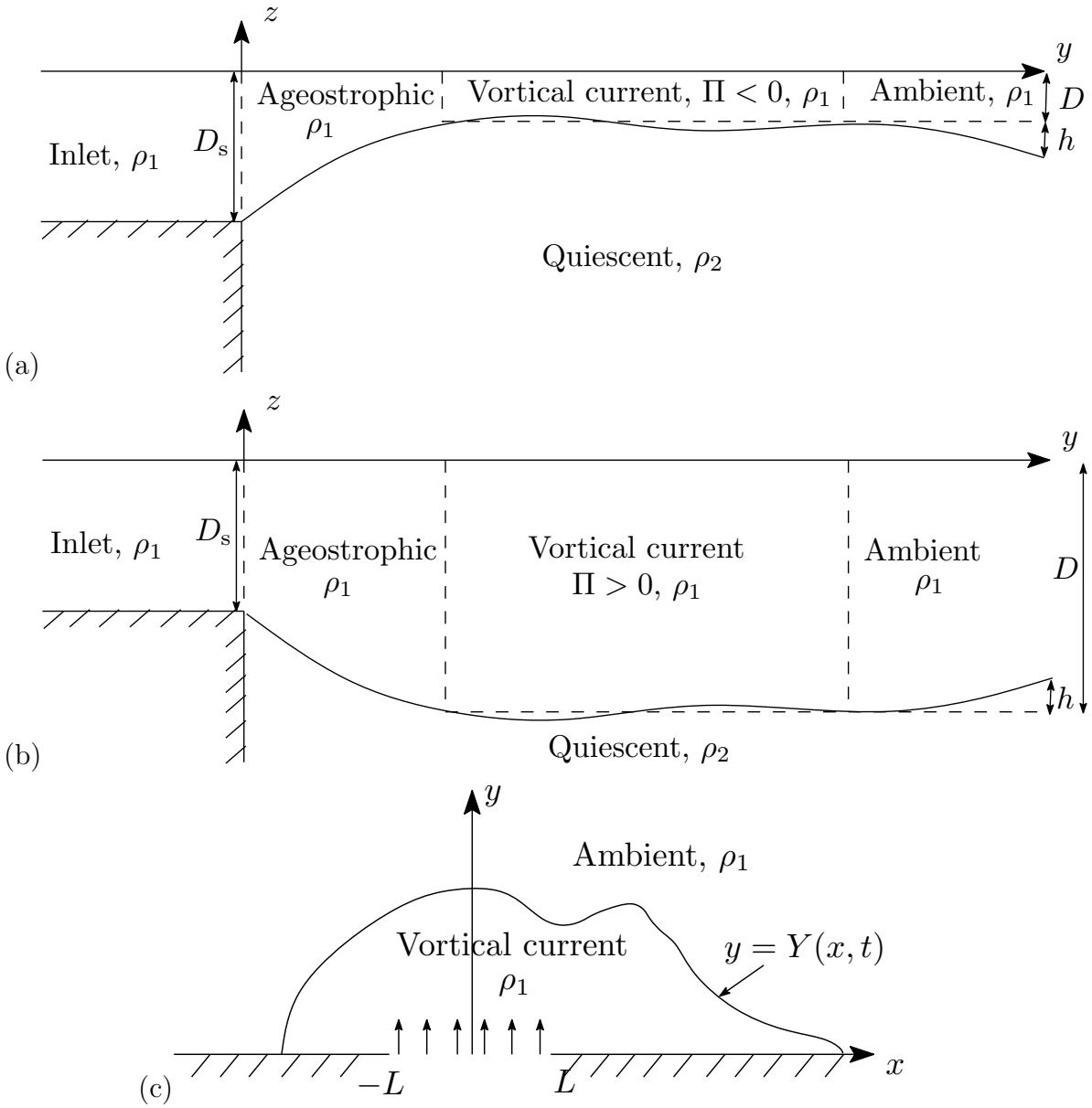

Figure 4.1: A schematic of the flow geometry near the source. (a) A side view of the offshore profile (i.e. in the (y, z) plane) at the source. Before the source is switched on at $t = 0$ the ambient is a quiescent two-layer fluid with interface depth D. When the outflow begins the expelled fluid rapidly and ageostrophically adjusts to the depth D, giving a flow with surface perturbation of height h. Here $D < D_s$, the depth of the source, so uniform negative vorticity of Π is generated as the fluid is squashed vertically. (b) As (a) but for the case $D > D_s$ so the expelled fluid stretches as it adjusts and uniform positive vorticity is generated. (c) A plan view in the horizontal (x, y) plane showing the boundary $y = Y(x, t)$ of the vortical fluid at some time $t > 0$.

An arbitrary source profile is imposed with the boundary condition on the wall $\eta(x,0) = Q(x)$, where the source function $Q(x)$ is such that $Q(L) - Q(-L) = Q_0$. To give an initially quiescent flow, Q is selected such that $Q(x) = 0$ for $x < -L$ and $Q(x) = Q_0$ for $x > L$. However the analysis here generalises readily and is discussed for an arbitrary upstream value of Q, i.e. a flow with an additional alongshore ambient current, in subsection 5.2.2. This problem can be thought of as a dam-break scenario where basins with surface heights $h = 0$ and $h = g'Q_0/f$ are separated by a wall with a gap. When the dam is released the propagation of Kelvin waves rapidly establishes the value $\eta(x,0) = Q_0$ for $x > L$, along the righthand wall with this process being instantaneous in the QG limit. The form of $Q(x)$ is related to the normal outflow velocity by

$$v(x,0) = \frac{\partial Q}{\partial x}. \tag{4.3}$$

If $\mathcal{D}$ is the domain occupied by the ejected fluid, bounded by $\partial\mathcal{D}$, then from (4.2)

$$\nabla^2\eta - \frac{1}{L_{\mathrm{R}}^2}\eta = \begin{cases} \Pi, & \text{in } \mathcal{D}, \\ 0, & \text{outside } \mathcal{D}. \end{cases} \tag{4.4}$$

This equation, combined with the boundary condition specifying the source flux

$$\eta = Q(x), \qquad \text{for } y = 0, \tag{4.5}$$

and that the fluid is quiescent far from the source

$$\nabla\eta \to 0, \qquad \text{as } x^2 + y^2 \to \infty, \tag{4.6}$$

give the streamfunction η. The fluid velocity can then be found using (4.1). The problem is closed with the initial condition that the source is initiated at $t = 0$ and the condition that $\partial\mathcal{D}$ is a material boundary, which for outflows where $\partial\mathcal{D}$ can be expressed as $y = Y(x,t)$, can be written $\mathrm{D}(y - Y)/\mathrm{D}t = 0$ on $y = Y(x,t)$ and rearranged to

$$Y_t = [\eta(x, Y(x,t))]_x, \tag{4.7}$$

where subscripts denote partial derivatives.

Equations (4.4) to (4.7) describe the evolution of the expelled vortical fluid. The velocity is determined by the streamfunction η, which is in turn completely determined by the shape of the curve $\partial\mathcal{D}$. Since the PV is piecewise constant, the evolution of this curve can be accurately and efficiently computed using the method of contour dynamics with surgery [Dritschel, 1988].

If lengths in this problem are scaled on $\sqrt{Q_0/|\Pi|}$ and time on the vortical timescale $1/|\Pi|$ then the only parameter, apart from the sign of Π, is the ratio of the Rossby radius to the lengthscale, given by

$$a = L_{\mathrm{R}}\sqrt{\frac{|\Pi|}{Q_0}}. \tag{4.8}$$

This nondimensional parameter, the reciprocal of the Kelvin number discussed for outflows by Garvine [1995], measures the relative importance of the relative vorticity to the planetary vorticity and therefore also the relative importance of the vorticity to the asymmetric, rotation-modified component of the source velocity. For large values of a (small Kelvin number), the interface is stiff and the dynamics are dominated by the anomalous vorticity. For small a (large Kelvin number), the interface is less stiff, effects are more localised and the dynamics are dominated by the source. For the large river outflows considered here such as the Columbia River outflow or Chesapeake Bay outflow volume fluxes can be in the region of 10^3-$10^4\,\mathrm{m^3 s^{-1}}$, depths are typically 10^0-$10^1\,\mathrm{m}$, timescales are 10-100 days and lengthscales are 10-100 km [Horner-Devine et al., 2015].

As section 5.1.4 later discusses, both the rotation-modified component of the source and the vorticity contribute fluxes of x-momentum which can be used to understand the turning of the current. The relative importance of these two momentum fluxes is dictated by a. When the outflow adjusts to a deeper level Π is negative and the vorticity contributes negative momentum flux, working against the source and driving the current leftward. As a measures the balance of these two fluxes it controls how much fluid can turn left and how much must turn right. In the rigid-lid limit $a \to \infty$, vorticity is solely responsible for turning the current and analytical solutions for steady profiles are given by Johnson and McDonald [2006]. The equations here are left in fully dimensional form and, noting that the evolution

of an outflow depends only on a and the sign of Π, the dynamics are discussed over the full parameter range.

4.2 The long wave approximation

Typically coastal outflows have a much larger alongshore extent than offshore. In this case (4.4) can be replaced by

$$\frac{\partial^2 \eta}{\partial y^2} - \frac{1}{L_{\mathrm{R}}^2}\eta = \begin{cases} \Pi, & 0 < y < Y, \\ 0, & y > Y, \end{cases} \tag{4.9}$$

and solved explicitly to give the streamfunction $\eta(x, y, t)$ for a current of width $Y(x, t)$

$$\eta = L_{\mathrm{R}}^2 \Pi \left[\frac{\mathrm{e}^{(y-Y)/L_{\mathrm{R}}}}{2} + \left(\frac{Q}{L_{\mathrm{R}}^2 \Pi} + 1 - \frac{\mathrm{e}^{-Y/L_{\mathrm{R}}}}{2} \right) \mathrm{e}^{-y/L_{\mathrm{R}}} - 1 \right], \tag{4.10}$$

for $y \leq Y$ and $\eta = Q_{\mathrm{e}} \exp(-(y - Y)/L_{\mathrm{R}})$ for Y, where $Q_{\mathrm{e}} = \eta(x, Y)$ is the flux exterior to the current, which is to be found as part of the solution. The flux Q_{e} is a key quantity of interest as it dictates how much flux turns leftward (Q_{e}) and how much rightward ($Q_0 - Q_{\mathrm{e}}$). Using this expression in (4.7) and substituting $Z = \exp(-Y/L_{\mathrm{R}})$ (for simplicity) gives the equation for the evolution of the current width

$$\frac{\partial Z}{\partial t} + \Pi L_{\mathrm{R}} Z \left(1 + \frac{Q}{L_{\mathrm{R}}^2 \Pi} - Z \right) \frac{\partial Z}{\partial x} = -\frac{Z^2}{L_{\mathrm{R}}} \frac{\partial Q}{\partial x}. \tag{4.11}$$

Evaluating (4.10) at $y = Y(x)$ gives

$$Z^2 - 2\left(\frac{Q}{L_{\mathrm{R}}^2 \Pi} + 1 \right) Z + 1 = \frac{-2Q_{\mathrm{e}}}{L_{\mathrm{R}}^2 \Pi}, \tag{4.12}$$

giving $Z(x)$, and therefore the current width $Y(x)$, as a function of $Q(x)$ and $\eta(x, Y) = Q_{\mathrm{e}}$.

The long wave approximation giving (4.9) can be made whenever the source half-width L is large in comparison to the current width Y or the Rossby radius L_{R}. However, even for narrow sources the interface Y is typically slowly varying in x so this approximation still applies. Thus, as will be shown later, these long

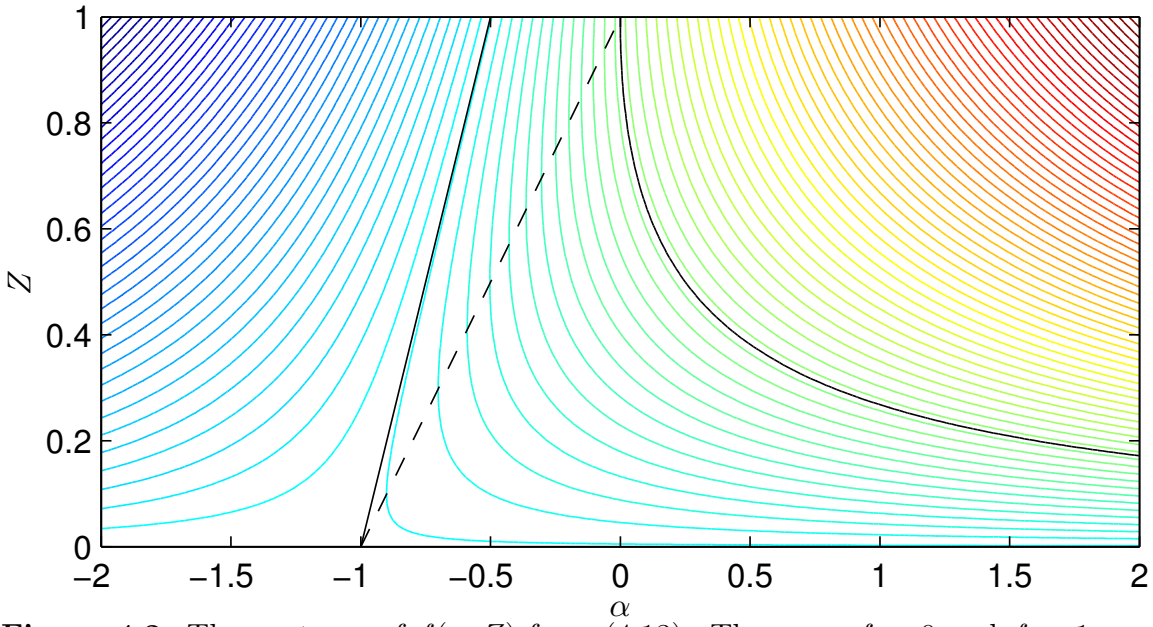

Figure 4.2: The contours of $f(\alpha, Z)$ from (4.13). The cases $f = 0$ and $f = 1$ are shown in black and the line $Z = \alpha + 1$ where $\partial f/\partial Z = 0$ is shown dashed.

wave results describe much of the evolution of the current width accurately, even for narrow sources. As an extreme test, many of the results considered here are for a point source i.e. $L \to 0$.

4.2.1 Steady boundary profiles

For steady solutions Q_e is a constant and the current width is given as a function of $Q(x)$ by (4.12). The existence of steady solutions can be neatly analysed by rewriting (4.12) as

$$f(\alpha, Z) = Z^2 - 2\,(\alpha + 1)\,Z + 1 = -2\alpha_\mathrm{e}, \tag{4.13}$$

where $\alpha(x) = Q(x)/L_\mathrm{R}^2\Pi$ and $\alpha_\mathrm{e} = Q_(x)/L_\mathrm{R}^2\Pi$, where Q_e and α_e are constants across a steady section of the outflow. The contours of $f(\alpha, Z)$ are plotted in fig. 4.2. The value of α_e on the contour dictates the turning of the current: if $\alpha_\mathrm{e} = 0$ then the entire current turns right, and if $\alpha_\mathrm{e} = Q_0/L_\mathrm{R}^2|\Pi|$ then the entire current turns left. For a steady solution over the source region to exist there must be a contour of (4.13) joining the solution from the right where $Q = Q_0$ to the left where $Q = 0$. For positive PV this equates to a contour of $f(\alpha, Z)$ joining $\alpha = 0$ to $\alpha = Q_0/L_\mathrm{R}^2\Pi$, which is possible for all values of $Q_0/L_\mathrm{R}^2\Pi$. The solution is given by the contour with

$\alpha_e = 0$ (shown in black in fig. 4.2) which starts at the point $\alpha = 0$, $Z = 1$, showing that this solution carries the full flux of the source and joins to the wall on the left hand end of the source $x = -L$. Where $\alpha = Q_0/L_R^2\Pi$, $Z < 1$ so to the right of the source this solution terminates in a constant width current, which can extend downstream in the region $x > L$.

For steady solutions for negative PV outflows, there must be a contour joining $\alpha = 0$ to $\alpha = Q_0/L_R^2\Pi$. The contour $f(\alpha, Z) = 1$ is given by $Z = 2(\alpha + 1)$ and is displayed in black in fig. 4.2. Clearly no other contours can cross this line so no solution can connect $\alpha = 0$ to $\alpha \leq -1$ and there can be no steady solution across the source region for $Q_0/L_R^2|\Pi| \geq 1$ (i.e. for $a \leq 1$). In these cases a bulge near the source must grow indefinitely.

For $Q_0/L_R^2\Pi < 1$ (i.e. for $a \geq 1$) a number of contours can connect across the source region. The narrowest of these solutions (that with largest Z) ends on the left at the line $\partial f/\partial Z = 0$, given by $Z = \alpha + 1$ and displayed dashed in fig. 4.2. This critical hydraulic solution Z_h is selected by the full solution to (4.11). However, as will be shown later, for narrow sources other solutions may be selected.

4.2.2 Steady profiles with an alongshore ambient current

For outflows with an additional alongshore ambient current of strength Q_c, which has streamfunction $\eta_c = Q_c \exp(-y/L_R)$, a steady solution must connect $\alpha = Q_c/L_R^2\Pi$ to $\alpha = (Q_c + Q_0)/L_R^2\Pi$. The analysis follows similarly to before and the results are discussed in section 5.2.2. In particular, fig. 5.16 summarises the possible dynamics based on the values of a and Q_c/Q_0 as described below. Steady currents are now possible in two cases. The first case is similar to that for no ambient current and requires $\alpha > -1$ on the left side of the source. For $Q_c < 0$ this requires $a > \sqrt{-Q_c/Q_0}$ (up to $Q_c = 2$) and gives bidirectional steady currents as Y is non-zero on both sides of the source. Or, for $Q_c > 0$, steady solutions exist for all a and have $Z = 1$ (i.e. $Y = 0$) on the left so the steady current is unidirectional, contains the entire flux Q_0 and turns rightward.

In the second case, a strong leftward ambient current, a new type of solution,

a steady leftward current is found. This can either have $\alpha < -0.5$ at $x = L$ if $a < \sqrt{-2(Q_c/Q_0 + 1)}$ or have $-0.5 < \alpha < 0$ at $x = L$ and connect as far as the line $\partial f/\partial Z = 0$ (shown dotted in fig. 4.2). This second alternative is possible if $a < \sqrt{-2(Q_c/Q_0 + 1)}$, $Q_c/Q_0 < -1$ and $a < -Q_c/\sqrt{2}Q_0$.

4.3 Unsteady evolution of long wave outflows

The boundary of the expelled fluid follows from (4.11), a first order quasilinear inhomogeneous hyperbolic PDE. The evolution of the current width along the characteristics of (4.11) is given by

$$\frac{\mathrm{d}Z}{\mathrm{d}t} = -\frac{Q_x}{L_R} Z^2, \tag{4.14a}$$

$$\frac{\mathrm{d}x}{\mathrm{d}t} = \Pi L_R Z \left(1 + \frac{Q}{L_R^2 \Pi} - Z\right), \tag{4.14b}$$

where $Q_x = \partial Q/\partial x$.

Outside of the source region $Q_x = 0$ so Z (and therefore the current width Y) is constant along characteristics, which therefore, according to (4.14b), move at constant speed. Thus, outside of the source region only three behaviours are possible: constant width currents, rarefactions and steepening currents resulting in shocks. Once the evolution in the source region is determined, the downstream and upstream evolutions are given by simple analytical solutions.

4.3.1 Universal solutions for a point source outflow

For a point source outflow $Q = Q_0 H(x)$, for the Heaviside function H, the boundary evolution is given by universal similarity solutions. These are derived below for the three cases of downstream rarefactions for positive PV, and both upstream and downstream rarefactions for negative PV. The implications of these similarity solutions is that the corresponding experimental results should all collapse onto a single

curve in each of these three cases. The solutions are functions of the non-dimensional speed variable $s = x/|\Pi|L_{\mathrm{R}}t$, noting that, for $t > 0$, $Q = Q_0 H(s)$. Rewriting (4.11) in terms of s gives

$$\left[\mathrm{sgn}(\Pi)Z\left(1 + \frac{Q}{L_{\mathrm{R}}^2\Pi} - Z\right) - s\right]\frac{\partial Z}{\partial s} = 0, \tag{4.15}$$

away from the source. Therefore either $\partial Z/\partial s = 0$ and the current has constant width or

$$\mathrm{sgn}(\Pi)Z\left(1 + \frac{Q}{L_{\mathrm{R}}^2\Pi} - Z\right) - s = 0. \tag{4.16}$$

4.3.1.1 Upstream rarefactions for negative PV

Upstream ($x < -L$) rarefactions are only possible for negative PV. In this case (4.16) becomes

$$Z^2 - Z - s = 0, \tag{4.17}$$

giving the universal solution

$$Z = (1 - \sqrt{1 + 4s})/2, \tag{4.18}$$

for $-0.25 \leq s \leq 0$, meaning that rarefaction head moves upstream at speed $0.25|\Pi|L_{\mathrm{R}}$.

4.3.1.2 Downstream rarefactions for positive PV

For positive PV only downstream ($x > L$) rarefactions are possible. For these, (4.16) becomes

$$Z\left(1 + \frac{1}{a^2} - Z\right) - s = 0. \tag{4.19}$$

The simple solution to this equation is not universal in these variables but can be made so by rescaling using $Z = \lambda\hat{Z}$, $s = \lambda^2\hat{s}$, where $\lambda = 1 + a^{-2}$, to give

$$\hat{Z}^2 - \hat{Z} + \hat{s} = 0, \tag{4.20}$$

with solution

$$\hat{Z} = (1 - \sqrt{1 - 4\hat{s}})/2, \tag{4.21}$$

for $0 < \hat{s} < 0.25$. The minimum width of the current is given by $Z = (1 + a^{-2})/2$ so for $a \leq 1$ this rarefaction terminates at the wall and for $a > 1$ it cannot meet the wall and must end in a shock.

4.3.1.3 Downstream rarefactions for negative PV

For negative PV upstream rarefactions obey

$$Z\left(1 - \frac{1}{a^2} - Z\right) + s = 0. \tag{4.22}$$

Rescaling using $Z = \lambda\hat{Z}$, $s = \lambda^2\hat{s}$, where $\lambda = |1 - a^{-2}|$, gives

$$\hat{Z}^2 - \mathrm{sgn}(\lambda)\hat{Z} - \hat{s} = 0. \tag{4.23}$$

For $a = 1$, $\mathrm{sgn}(\lambda) = 0$ and $Z = \sqrt{s}$, $0 \leq s \leq 1$. For $a > 1$, $\mathrm{sgn}(\lambda) = 1$ and the universal solution is

$$\hat{Z} = (1 + \sqrt{1 + 4\hat{s}})/2. \tag{4.24}$$

Note that at $s = 0$, $Z = \lambda$, the width of the constant width current, so this solution joins continuously onto the steady current. For $a < 1$ the universal solution is

$$\hat{Z} = (-1 + \sqrt{1 + 4\hat{s}})/2, \tag{4.25}$$

which grows indefinitely at $s = 0$ and can always connect to the wall downstream.

4.3.2 Outflow from a uniform strength source

For a uniform source i.e. a source with strength

$$Q(x) = \begin{cases} 0, & x \leq -L, \\ Q_0(x + L)/2L, & -L < x \leq L, \\ Q_0, & L < x, \end{cases} \tag{4.26}$$

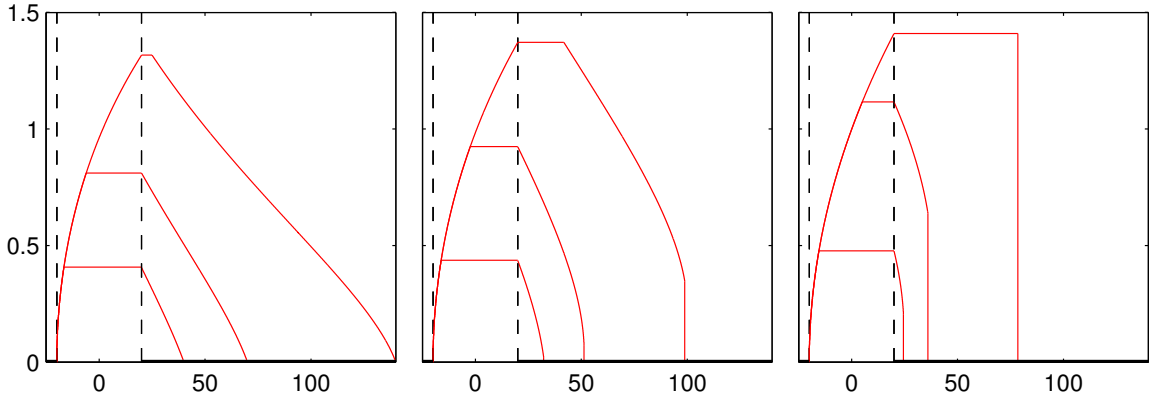

Figure 4.3: The analytical long wave solution for the boundary of a positive PV outflow from a uniform source of half-width $L = 20$ at times $t = 20$, 50, 120 for (left to right) $a = 1$, 1.6, 5. In this, and all subsequent figures, the coast is shown as a thick black line and the edges of the source region are shown as black dashed lines. Note also that all outflow figures in this chapter are on unequal-aspect axes to fully display the wide outflows. Outflows are displayed on equal-aspect axes in chapter 5.

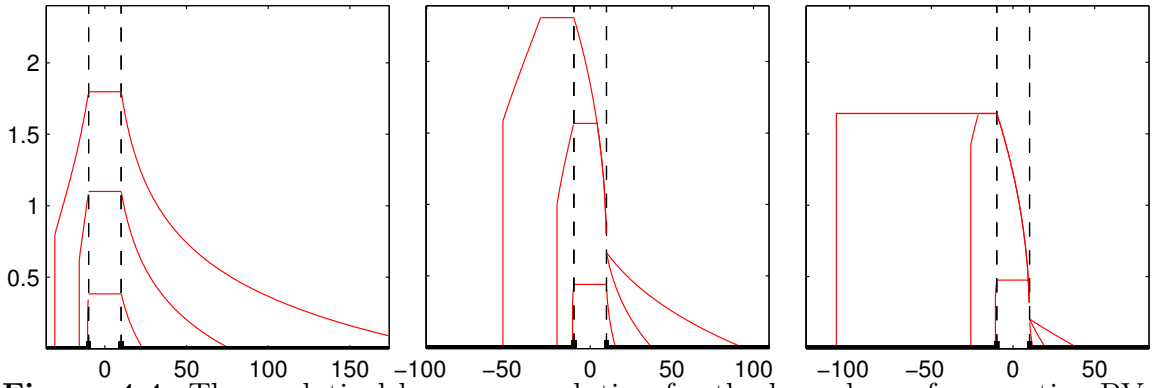

Figure 4.4: The analytical long wave solution for the boundary of a negative PV outflow from a uniform source of half-width $L = 10$ at times $t = 10$, 50, 150 for (left to right) $a = 0.7$, 1.8, 5.

the evolution can almost entirely be described with simple analytical solutions. These are displayed for positive PV in fig. 4.3 and negative PV in fig. 4.4, with these results derived below.

4.3.2.1 The source region

The characteristic equation for Z in the source region (4.14a) is

$$\frac{\mathrm{d}Z}{\mathrm{d}t} = -\frac{Q_0}{2LL_\mathrm{R}}Z^2, \tag{4.27}$$

with solution

$$Z_{\mathrm{s}} = \frac{1}{1 + \frac{Q_0 t}{2LL_{\mathrm{R}}}}, \tag{4.28}$$

giving

$$Y_{\mathrm{s}} = L_{\mathrm{R}} \log\left(1 + \frac{Q_0 t}{2LL_{\mathrm{R}}}\right). \tag{4.29}$$

Thus the outflow boundary in the source region grows uniformly. For negative PV and $a \leq 1$ there is no steady solution so the growth continues indefinitely as seen in the left panel of fig. 4.4. For negative PV outflows with $a > 1$ or for positive PV outflows a steady solution across the source region exists and the outflow boundary increases following (4.28) until it reaches the steady profile at some time $t = t_1$ (with $t_1 = 0$ for positive PV). The central panel of fig. 4.4 shows the boundary at $t = 10 < t_1$. For $t > t_1$ the profile across the source region is given by $Z = \min(Z_{\mathrm{s}}, Z_{\mathrm{h}})$, where Z_{h} is the critical steady hydraulic solution to (4.12) as seen in fig. 4.3 and the central panel of fig. 4.4. At the time $t = t_2$ and beyond, the steady solution is completely established across the source region.

4.3.2.2 Downstream region for positive PV

Downstream of the source for positive PV integrating along the characteristics of (4.14) shows that the current is led by an unsteady profile given by

$$Z_{\mathrm{r}} = \frac{1}{1 + \frac{Q_0 t_{\mathrm{r}}}{2LL_{\mathrm{R}}}}, \tag{4.30a}$$

$$x_{\mathrm{r}} = L + \Pi L_{\mathrm{R}} Z_{\mathrm{r}} \left(1 + \frac{1}{a^2} - Z_{\mathrm{r}}\right)(t - t_{\mathrm{r}}), \tag{4.30b}$$

for $t > t_{\mathrm{r}}$, where $0 < t_{\mathrm{r}} < t_2$, left in implicit form here for simplicity. For $t < t_2$ this solution joins to the growing solution in the source region. For $t > t_2$ a constant width current joins the steady solution to the rarefaction as displayed in fig. 4.3.

For $a \leq 1$ this fully describes the solution. However, for $a > 1$ the front of the current steepens until a shock with position x_{j} and height Y_{j} (giving $Z_{\mathrm{j}} = -L_{\mathrm{R}} \log Y_{\mathrm{j}}$) forms. The shock conserves mass and has the rarefaction height so its speed, height

and position are given by

$$\frac{\mathrm{d}x_\mathrm{j}}{\mathrm{d}t} = \frac{Q_0 - Q_\mathrm{e}}{Y_\mathrm{j}} = -\frac{L_\mathrm{R}\Pi}{2}\frac{(Z_\mathrm{j} - \frac{2}{a^2} - 1)(Z_\mathrm{j} - 1)}{\log Z_\mathrm{j}}, \tag{4.31a}$$

$$Z_\mathrm{j} = \frac{1}{1 + \frac{Q_0 t_\mathrm{j}}{2LL_\mathrm{R}}}, \tag{4.31b}$$

$$x_\mathrm{j} = L + \Pi L_\mathrm{R} Z_\mathrm{j}\left(1 + \frac{1}{a^2} - Z_\mathrm{j}\right)(t - t_\mathrm{j}). \tag{4.31c}$$

Eliminating t_j from (4.31c) using (4.31b) and differentiating the result with respect to t gives a second expression for $\mathrm{d}x_\mathrm{j}/\mathrm{d}t$ which can be equated with (4.31a) and rearranged to give

$$\left[(\lambda - 2Z_\mathrm{j})\left(t - \mu\left(\frac{1}{Z_\mathrm{j}} - 1\right)\right) + \mu\frac{(\lambda - Z_\mathrm{j})}{Z_\mathrm{j}}\right]\frac{\mathrm{d}Z_\mathrm{j}}{\mathrm{d}t} = -\frac{(Z_\mathrm{j} - \frac{2}{a^2} - 1)(Z_\mathrm{j} - 1)}{2\log Z_\mathrm{j}} - Z_\mathrm{j}(\lambda - Z_\mathrm{j}), \tag{4.32}$$

where $\lambda = 1 + a^{-2}$ and $\mu = 2LL_\mathrm{R}/Q_0$. Solving (4.32) with the initial condition $Z_\mathrm{j}(0) = 1$ gives the evolution of the shock height and therefore the position via (4.31). In practice the most straightforward approach is to integrate this ODE numerically. For $a > 1$ the shock grows from $Z_\mathrm{j} = 1$ until a steady solution is reached when the right hand side of (4.32) is zero, i.e. when

$$\frac{(Z_\mathrm{j} - \frac{2}{a^2} - 1)(1 - Z_\mathrm{j})}{2\log Z_\mathrm{j}} = Z_\mathrm{j}(\lambda - Z_\mathrm{j}). \tag{4.33}$$

This equation can be solved numerically to give the steady value of Z_j for any given value of a. As a increases, the height of the jump increases and eventually exceeds the steady current height given by (4.12) as $Z = \lambda - \sqrt{\lambda^2 - 1}$. The value of a at which this first occurs can be found by equating this steady current height with the steady jump height given by (4.33). Solving this numerically gives the critical value of $a_\mathrm{c} \approx 1.8684$. For $a > a_\mathrm{c}$ the jump height increases until it reaches the steady current width and from there onwards it propagates along the constant width current and can grow no further. The growth of the jump can be seen in the second two panels of fig. 4.3. The third panel is for $a = 5 > a_\mathrm{c}$ and at the final time displayed the steady current has overtaken the jump. Note that the junction between the unsteady current and constant width current moves at the unsteady current speed,

until it overtakes the shock, where it takes the lower shock speed.

4.3.2.3 Downstream region for negative PV

For negative PV the flow in the upstream region is led by a rarefaction given, analogously to (4.30), by

$$Z_{\mathrm{r}} = \frac{1}{1+\frac{Q_0 t_{\mathrm{r}}}{2LL_{\mathrm{R}}}}, \tag{4.34a}$$

$$x_{\mathrm{r}} = L + \Pi L_{\mathrm{R}} Z_{\mathrm{r}} \left(1 + \frac{1}{a^2} - Z_{\mathrm{r}}\right)(t - t_{\mathrm{r}}), \tag{4.34b}$$

for $t > t_{\mathrm{r}}$, where $0 < t_{\mathrm{r}} < t_1$. For $t > t_1$ this rarefaction is joined on the left by a constant width current to the steady solution across the source. Unlike the positive PV case, this solution is simply a rarefaction and no shock can form.

4.3.2.4 Upstream region for negative PV

The downstream unsteady current is, analogously to (4.30) and (4.34), given by

$$Z_{\mathrm{r}} = \frac{1}{1+\frac{Q_0 t_{\mathrm{r}}}{2LL_{\mathrm{R}}}}, \tag{4.35a}$$

$$x_{\mathrm{r}} = -L + \Pi L_{\mathrm{R}} Z_{\mathrm{r}} \left(1 - Z_{\mathrm{r}}\right)(t - t_{\mathrm{r}}), \tag{4.35b}$$

for $t > t_{\mathrm{r}}$, where $0 < t_{\mathrm{r}} < t_2$. For $t > t_2$ this is connected on the right to the steady current at $x = -L$ by a constant width current. As in the downstream region for positive PV, shocks can form upstream for negative PV, but in this case this happens for all values of a. The shock evolution is governed by

$$\frac{\mathrm{d}x_{\mathrm{j}}}{\mathrm{d}t} = \frac{-Q_{\mathrm{e}}}{Y_{\mathrm{j}}} = -\frac{L_{\mathrm{R}}\Pi}{2}\frac{(Z_{\mathrm{j}}-1)^2}{\log Z_{\mathrm{j}}}, \tag{4.36a}$$

$$Z_{\mathrm{j}} = \frac{1}{1+\frac{Q_0 t_{\mathrm{j}}}{2LL_{\mathrm{R}}}}, \tag{4.36b}$$

$$x_{\mathrm{j}} = -L + \Pi L_{\mathrm{R}} Z_{\mathrm{j}} \left(1 - Z_{\mathrm{j}}\right)(t - t_{\mathrm{j}}). \tag{4.36c}$$

Rearranging and differentiating as before gives the ODE for Z_j

$$[(2Z_\mathrm{j}-1)t+2\mu(1-Z_\mathrm{j})]\,\frac{\mathrm{d}Z_\mathrm{j}}{\mathrm{d}t}=\frac{(Z_\mathrm{j}-1)^2}{2\log Z_\mathrm{j}}+Z_\mathrm{j}(1-Z_\mathrm{j}), \tag{4.37}$$

where, as before, $\mu = 2LL_\mathrm{R}/Q_0$. Integrating (4.37) numerically with the initial condition $Z_\mathrm{j}(0) = 1$ gives the evolution of the shock. The shock height increases up to a maximum height when the right hand side of (4.37) is zero, i.e. when

$$Y_\mathrm{max}/a = -\log Z_\mathrm{j} = (1-Z_\mathrm{j})/2Z_\mathrm{j}, \tag{4.38}$$

which has approximate solution $Y_\mathrm{max} \approx 1.25643a$. The critical value of a where this maximum jump height first exceeds the constant width current is given by equating Y_max and the current width $Y = -a\log(1-\sqrt{2-a^{-2}}/a)$ to give

$$a_\mathrm{c} = \left[b+\sqrt{1-b^2}/b^2\right]^{\frac{1}{2}} \approx 1.82206, \qquad b = 1-\exp\left(-Y_\mathrm{max}/a\right). \tag{4.39}$$

In the right hand panel of fig. 4.4 $a = 5 > a_\mathrm{c}$ and the constant width current overtakes the shock.

4.4 Outflow simulations

The full two-dimensional evolution of the outflow boundary can be accurately computed using the method of contour dynamics. This section examines these results in comparison to the analytical long wave solutions for two test cases: a uniform source and, as an extreme test of the theory, a point source.

Figure 4.5 shows a contour dynamics simulation of a negative PV outflow with vortical velocity profiles $u(x, y)$ for fixed x as functions of y computed numerically and compared to the long wave theory. It should be noted that these profiles are the component of velocity due to vorticity so are the full velocity with the component due to the source subtracted.[1] This choice has been made to highlight the relevant

[1]The solution can be split into a component due to the source: the linear solution to $\mathcal{L}\eta = 0$, with $\eta(x, 0) = Q(x)$, and the nonlinear component due to the vorticity: the solution to $\mathcal{L}\eta = \Pi$, $\eta(x, 0) = 0$.

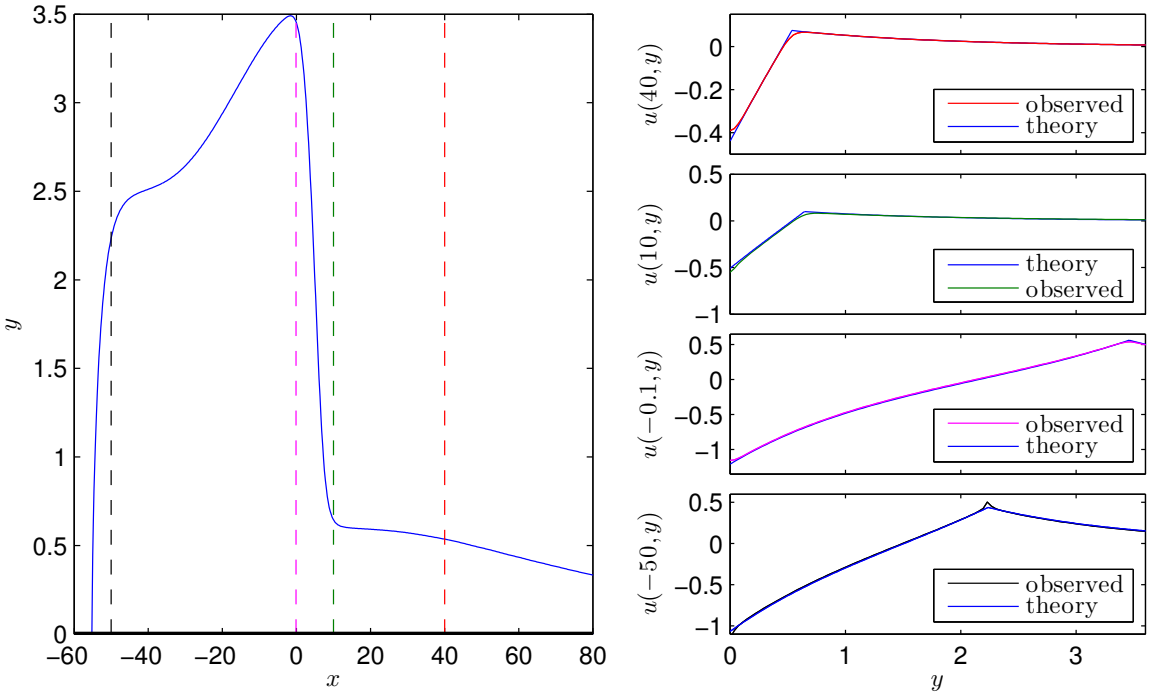

Figure 4.5: A snapshot of outflow boundary (left) from a contour dynamics simulation of a negative PV outflow from a point source for $a = 1.3$ at time $t = 220$. The right hand panels show cross sections of the vortical velocity profile $u(x, y)$ as a function of y for four values of $x = 40$, 10, -0.1 and -50. The long wave velocity profile (blue) is compared to numerically computed velocity profiles (coloured). The position of the cross section is indicated in the left hand panel with a dashed line of the corresponding colour.

comparison, instead of comparing two velocity profiles with the same function added to each, which may hide any differences. The measured and theoretical profiles agree extremely well and are graphically indistinguishable almost everywhere. The only differences are at the outer and inner edges of the current, however these differences are due to numerical error, not a breakdown of the theory. The velocity profiles are computed using a crude, first-order approximation to the expression giving the velocity at a point as an integral over the boundary of the Green's function (as used in contour dynamics). Without explicitly taking account of the Green's function singularity, the contribution from nodes very close to the evaluation point is poorly represented, resulting in errors when evaluating velocities near to the contour and resulting in the errors seen in $u(x, y)$ at the current edges. Note that all other contour dynamics results in this thesis use a sophisticated, higher-order contour dynamics algorithm taking account of the singularities [Dritschel, 1988].

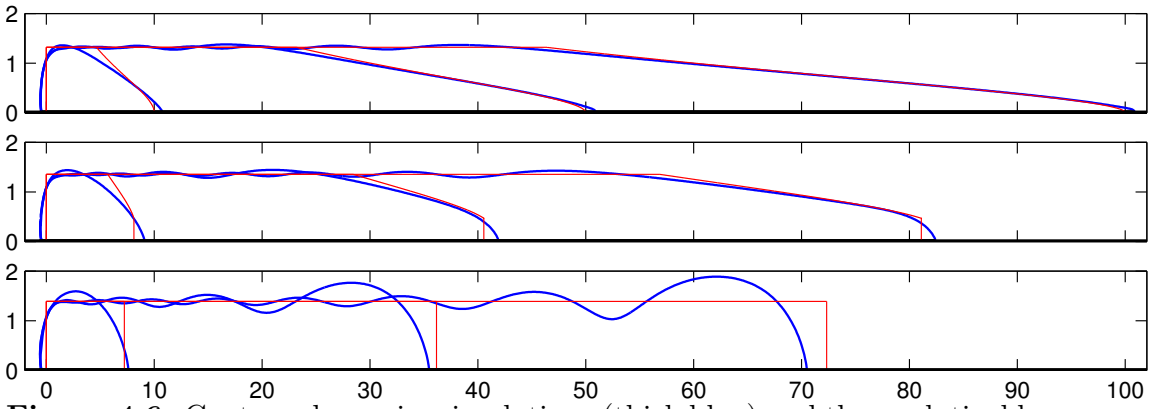

Figure 4.6: Contour dynamics simulations (thick blue) and the analytical long wave solutions (thin red) for positive PV outflows from a point source at times $t = 10$, 50, 100 and parameter values (top to bottom) $a = 1$, 1.3, 2

4.4.1 Positive PV

Figure 4.6 compares contour dynamics and the long wave solutions for positive PV outflows from a point source at various times and values of a. The two are almost indistinguishable over the rarefaction, particularly for the two later times $t = 50$ and 100 and for $a = 1$ (top panel). The constant width current matches very well with the contour dynamics showing small interfacial Rossby waves perturbing the surface. A steady profile has developed around the source. As this is a point source outflow, the long wave theory cannot capture the profile here which has fully two dimensional dynamics. In the lower two panels the long wave solution features a shock. At the shock the long wave approximation breaks down and in the contour dynamics the shock is resolved into a rounded head. For the largest value of $a = 2$ (lower panel) the shock has the full height of the constant width current and is resolved into a large eddy, trailing larger waves than in the lower a results. The two-dimensional dynamics of the leading eddy were discussed in the rigid-lid limit, by Stern and Pratt [1985] who showed that the steepness of the nose front must equilibrate, but that, behind the frontal eddy the interface profile may steepen and overturn horizontally, leading to the entrainment of ambient fluid. These rigid-lid results appear to appropriately describe the dynamics for large a, although (see the positive PV contour dynamics simulations in fig. 5.2) the backward wave breaking decreases for lower a i.e. as the Kelvin number increases from zero. Overall, the long wave theory appears to represent the dynamics very well.

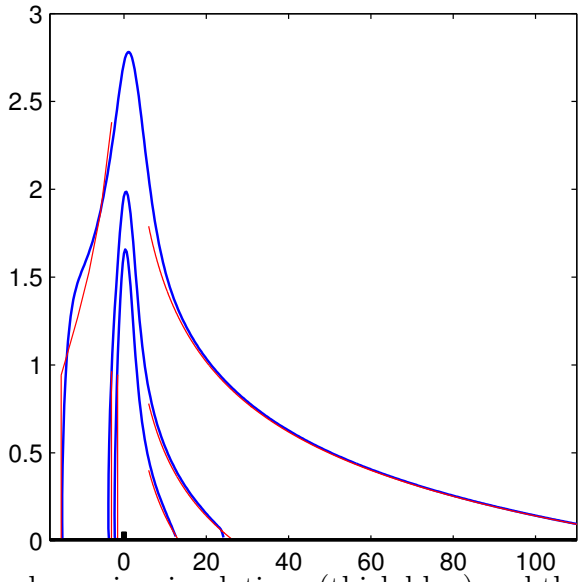

Figure 4.7: Contour dynamics simulations (thick blue) and the analytical long wave solutions (thin red) for a negative PV outflow from a point source with $a = 0.75$ at times $t = 10$, 20, 100.

4.4.2 Negative PV

Figure 4.7 compares contour dynamics and long wave simulations for a negative PV outflow from a point source for $a = 0.75$. These are indistinguishable in the downstream rarefaction. As this is a point source outflow, the dynamics near the source are fully two-dimensional and are not described by the long wave theory. In the upstream region the contour dynamics and long wave theory agree approximately but it appears that a 'shelf' i.e. a section of constant width current is beginning to form downstream in the contour dynamics simulations.

Figure 4.8 compares contour dynamics and long wave solutions for a negative PV outflow from a point source for $a = 1.3$. Here the rarefactions agree well in the far downstream but the point source outflow has selected a different steady solution to the critical steady solution across the source. As this is a point source outflow the early evolution is not governed by the long wave theory and the outflow is able to grow offshore past the critical steady solution and therefore selects an alternative steady solution. This gives different widths for the leftward and rightward steady solutions. However these widths are still described by the long wave theory, i.e. given one width, the other can be calculated. Upstream of the source the steady current ends in a rarefaction which joins onto a second section of steady current,

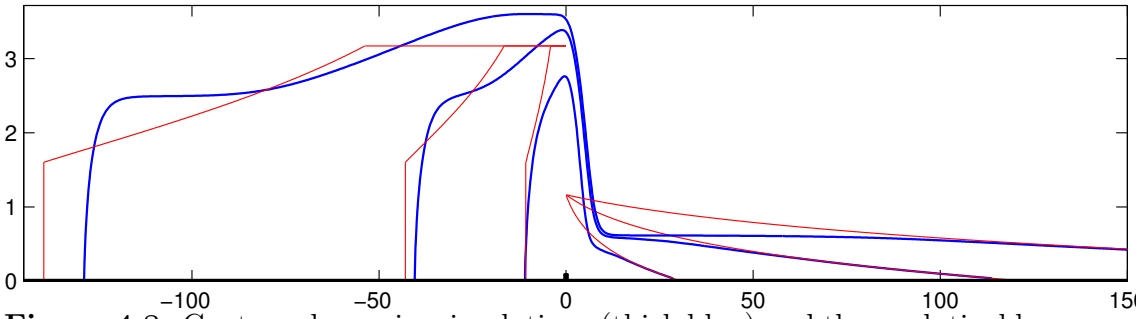

Figure 4.8: Contour dynamics simulations (thick blue) and the analytical long wave solutions (thin red) for a negative PV outflow from a point source with $a = 1.3$ at times $t = 30$, 150, 500.

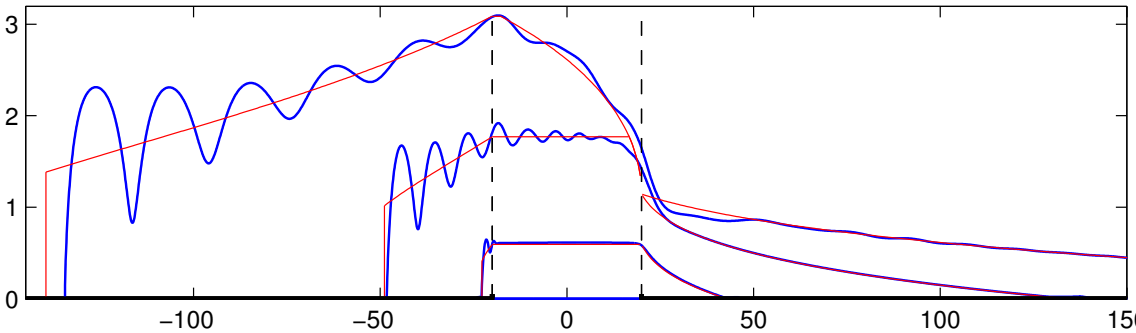

Figure 4.9: Contour dynamics simulations (thick blue) and the analytical long wave solutions (thin red) for a negative PV outflow from a uniform source of half-width $L = 20$ with $a = 1.3$ at times $t = 30$, 150, 500.

a 'shelf', which terminates in a shock. For this point source case the long wave theory, although still capturing the rough evolution, does not completely represent the outflow.

Figure 4.9 considers a negative PV outflow also for $a = 1.3$, but for a uniform source of half-width $L = 20$, appropriate for wide estuary outflows and river deltas [Horner-Devine et al., 2015], instead of the point source outflow in fig. 4.8. In this case the long wave approximation applies across the source region and the analytical solution accurately describes the contour dynamics results. The outflow across the source initially grows uniformly (see the solution at $t = 30$) until it reaches the steady solution which is then gradually established. The downstream rarefactions also agree well in this case. The contour dynamics results are perturbed by waves trailing the leading upstream shock. Upstream from the source region the contour dynamics shows waves around the long wave rarefaction solution but again a shelf further downstream appears to have formed.

Figure 4.10 compares contour dynamics and the long wave solution for a negative

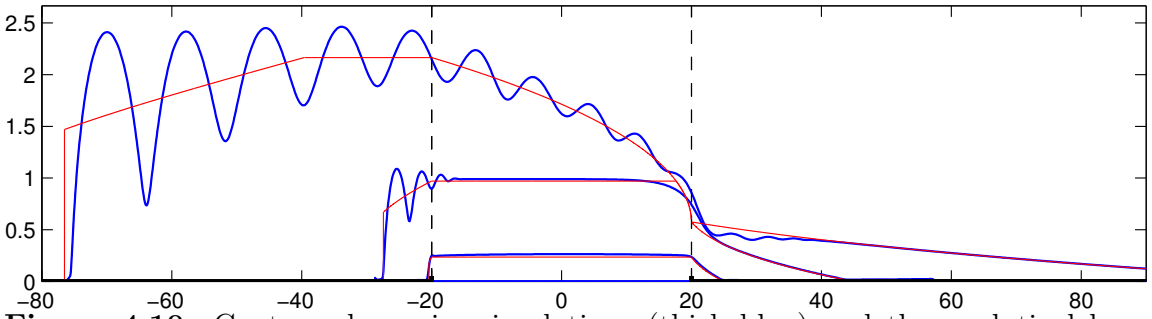

Figure 4.10: Contour dynamics simulations (thick blue) and the analytical long wave solutions (thin red) for a negative PV outflow from a uniform source of half-width $L = 20$ with $a = 2$ at times $t = 10$, 50, 200.

PV outflow from a uniform source of half-width $L = 20$ for $a = 2$. Again the long wave theory accurately captures the downstream rarefaction, the time-dependent and steady dynamics across the source region and the upstream steady current with the only differences due to waves perturbing the interface. However, upstream of the steady current the contour dynamics results deviate from the long wave rarefaction and appear to have again formed a shelf with width close to that of the constant width current.

Overall the long wave theory appears to represent the dynamics of outflows remarkably accurately with the only significant differences being interfacial waves and upstream shelving for negative PV outflows. Even for point source outflows the long wave theory describes the outflow dynamics accurately for positive PV and roughly for negative PV.

4.5 Conclusions

In this chapter a simple model of coastal outflows was described with the resultant behaviours analysed using contour dynamics simulations and analytical solutions derived using a long wave approximation. This simple one parameter model displays rich dynamics, which can nevertheless be described accurately by a gradually varying approximation. The outflow boundary can evolve to form steady currents, rarefactions or steepening currents resulting in shocks. Comparisons between the long wave analytical solutions and contour dynamics results show excellent agreement in most applicable cases. In fact, even for the extreme test of representing a point source

outflow, the analytical solutions reproduce positive PV outflows very well and represent many of the features of negative PV outflows. The main differences result from the early point source evolution where the long wave approximation does not apply, but after this initial stage it appears that the long wave solutions accurately represent the dynamics.

Chapter 5

Oceanographic applications of the quasigeostrophic model of coastal outflows

This chapter applies the model from chapter 4 to examine the outflow from a river, estuary or strait into a coastal ocean. First it uses the analytical solution developed in chapter 4 and contour dynamics simulations to discuss the implications of the model for an understanding of coastal outflows. Second, it extends the model and the long wave theory to consider the effects of ambient currents, tides, winds or a variable source flux. Third, a consideration of the momentum flux at the source is used to understand the turning of the current, showing that steady solutions conserve momentum and hence resolving the momentum imbalance paradox of Pichevin and Nof [1997]. Finally, a new numerical scheme to compute steady outflow profiles is developed. The simplicity of the model, and insight given by the long wave solutions, enables a full understanding of the dynamics. The outflows display a range of behaviours including indefinitely growing near-source bulges, steady profiles with varying offshore width, bidirectional currents and rarefying or eddy-like leading heads, all of which can be understood with the long wave theory. Despite the simplicity of the model, the results show good agreement in comparison with observations, experiments and numerical models.

Section 5.1 fully examines the primary problem of a constant strength outflow without ambient currents, tides or winds. Sections 5.1.1 to 5.1.3 give detailed results

for the evolution of quasigeostrophic outflows comparing simulations and theory for zero, positive and negative potential vorticity. Section 5.1.4 uses the momentum flux at the source to analyse the turning of the current and shows analytically and numerically that steady solutions conserve momentum. Section 5.1.5 presents a numerical scheme for computing steady profiles for general outflows and gives an asymptotic steady profile for the limit $a \to 0$. Section 5.2 extends the model to consider the effects of variable strength sources, alongshore currents, tides or winds. Conclusions and discussion are presented in Section 5.3.

Chapter 4 derives (4.10), (4.11) and (4.12), the key equations governing the evolution of an outflow boundary where a long wave approximation can be made, and uses these equations to construct the form of the variable width steady solutions and the leading unsteady profiles for arbitrary $Q(x)$, thus completely characterising the ultimate evolution of the flow. For simple source profiles analytical expressions giving the full evolution of the outflow over time are derived by following the characteristics of (4.11). All of these long wave results are compared to contour dynamics simulations and show very good agreement both in the evolution of the material boundary and in the velocity profiles. In this chapter, a number of these results will be used and the implications of (4.10), (4.11) and (4.12) will be analysed in an oceanographic context for the new cases of outflows of variable strength or with alongshore currents.

The long wave approximation is formally valid if the source half-width L is large compared to either the current width Y or the Rossby radius L_{R}. However, it also appears to be accurate for narrow sources. In fact, even with a point source ($L \to 0$), the interface Y is slowly and smoothly varying in the x-direction and chapter 4 shows that the long wave approximation reproduces much of the evolution correctly. Thus the precise details of the source velocity profile appear not to have a very large effect on the evolution of the outflow.

5.1 Constant strength sources without ambient currents, tides or winds

This section describes the outflow behaviour over the full range of a for the simple starting case of a constant flux source without the complicating effects of ambient currents, tides or winds. If the fluid adjusts to a shallower (or deeper) level it will generate negative (or positive) vorticity. For positive PV the momentum flux is positive and turns the current to the right. For negative PV the momentum flux is negative and turns the current leftward instead. Thus the discussion here is split into three cases: a zero PV outflow ($a = 0$), a cooperative positive PV outflow and an antagonistic negative PV outflow.

5.1.1 Outflow of zero PV fluid

If the PV of the outflow fluid is zero then it is simply passively advected by the source flow. The velocity field due to this source is derived in appendix B.2. It gives an asymmetric outflow due to the rapid radiation of Kelvin waves. For a point source, a universal solution for this problem can be obtained by scaling lengths on L_{R} and time on L_{R}^2/Q_0 (a different scaling to that discussed earlier) and is shown in fig. 5.1. The outflow turns to the right and moves downstream in a thinning current with downstream profile given very closely by $x = Q_0 \exp(-y/L_{\mathrm{R}})t/L_{\mathrm{R}}$. The flow cannot evolve to form a steady constant-width current and the bulge at the source grows indefinitely. The offshore extent of the bulge slows from fast initial growth to grow logarithmically in time, as can be seen by considering (B.14) for $x = 0$ and noting that for $r \gg L_{\mathrm{R}}$, $K_1(r/L_{\mathrm{R}})$ decreases exponentially in r. The boundary profile for small time is given by the rigid-lid solution: a growing semi circle with radius $r = \sqrt{2Q_0 t/\pi}$.

5.1.2 Outflow of positive PV fluid

If the outflow fluid has positive PV then there is an additional flux of positive x-momentum and the current is further driven rightwards under the influence of its

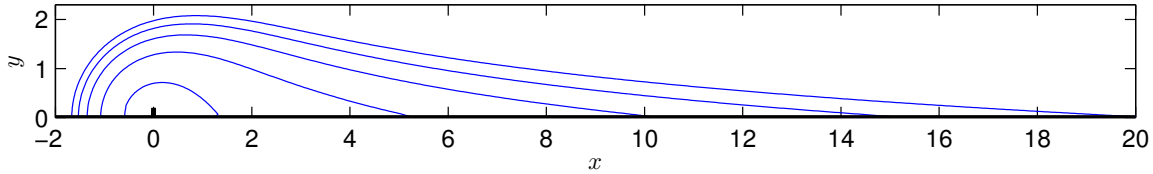

Figure 5.1: Contour dynamics results showing the boundary of a zero PV outflow driven by a point source at the origin for times t =1, 5, 10, 15, 20. In this and all subsequent figures the wall is shown as a thick black line with a notch marking the position of the source.

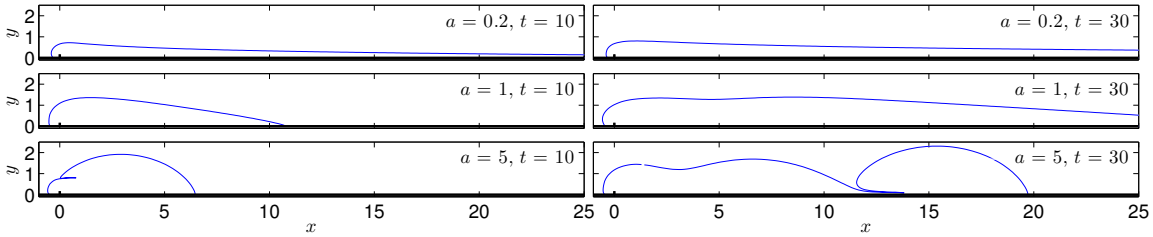

Figure 5.2: The boundary of a positive PV outflow driven by a point source in contour dynamics simulations for $Q_0 = 1$, $\Pi = 1$ and $L_\mathrm{R} = 0.2$, 1, 5, giving $a = 0.2$, 1, 5 at times t =10, 30.

image in the wall. The evolution of the expelled fluid for a range of a is shown in fig. 5.2. For small a (large Kelvin number), vorticity is weak compared to the source and a solution similar to that for zero PV (fig. 5.1) is found, except that, for non-zero a, a steady constant width current always forms. This steady current is led by a rarefying head with profile accurately given by a similarity solution to (4.11) (see chapter 4). For large a (small Kelvin number), the flow is dominated by the vorticity which drives the flow rightward in a steady constant width current, led by a large eddy. The solution for $a = 5$ is close to that for the rigid-lid limit $a \to \infty$ discussed by Johnson and McDonald [2006].

The width of the steady current, which evolves for all a and can be seen in fig. 5.2, is given by setting $Q_\mathrm{e} = 0$ in (4.12) to find

$$Y = L_\mathrm{R} \cosh^{-1}\left(1 + \frac{Q_0}{\Pi L_\mathrm{R}^2}\right). \tag{5.1}$$

The non-dimensional steady current width $Y' = Y\sqrt{|\Pi|/Q_0}$ increases monotonically with the parameter a and tends to the limiting width of $\sqrt{2}$. In fig. 5.3 this analytical solution is compared to the non-dimensionalised average current widths from contour dynamics simulations, computed by averaging the current width over a section of steady current to account for the small perturbations to the width. For all values

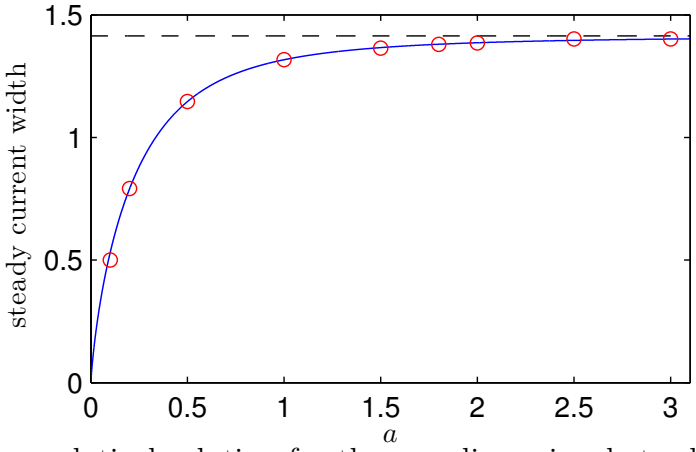

Figure 5.3: The analytical solution for the non-dimensional steady current width $Y' = Y\sqrt{|\Pi|/Q_0}$, where Y is given by (5.1), as a function of a (blue line) and the non-dimensionalised average current widths in contour dynamics simulations (red circles). The limit $Y \to \sqrt{2}$ as $a \to \infty$ is shown as a black dashed line.

of a the near-source bulge stops growing when it reaches the steady current width. At this point, the constant width current is progressively established downstream, perturbed only by interfacial Rossby waves.

Figure 5.4 shows a satellite radar image of the surface-intensified outflow from the wide mouth of Chesapeake Bay. The region occupied by the expelled fluid bears a strong resemblance to quasigeostrophic positive PV outflow (and indeed such a profile could not evolve for a negative PV QG outflow), shown in fig. 5.5 for both a point source and for a finite width source with uniform outflow velocity profile i.e. $v(x, 0) = v_0$ and $a = 2$, chosen because the density varies from 20 to 30 PSU [Donato and Marmorino, 2002], which, for a current of depth $D \approx$10 m, gives $L_{\mathrm{R}} \approx 10$ km, roughly twice the lengthscale. A point source, and a uniform source of width slightly larger than the bay are selected to bound the possible results, demonstrating that source width doesn't significantly effect the downstream profile. Both the observations and simulations show a long, narrow outflow confined to the coast, slowly varying around a steady profile and terminating in a rounded head. This rounded head is typical of the positive PV simulations presented here and doesn't form for a zero PV outflow (cf. fig. 5.1).

A closer comparison of the observed and numerical velocity fields in the vicinity of the head of the current is shown in fig. 5.6 and fig. 5.7, with arrows in fig. 5.6 showing

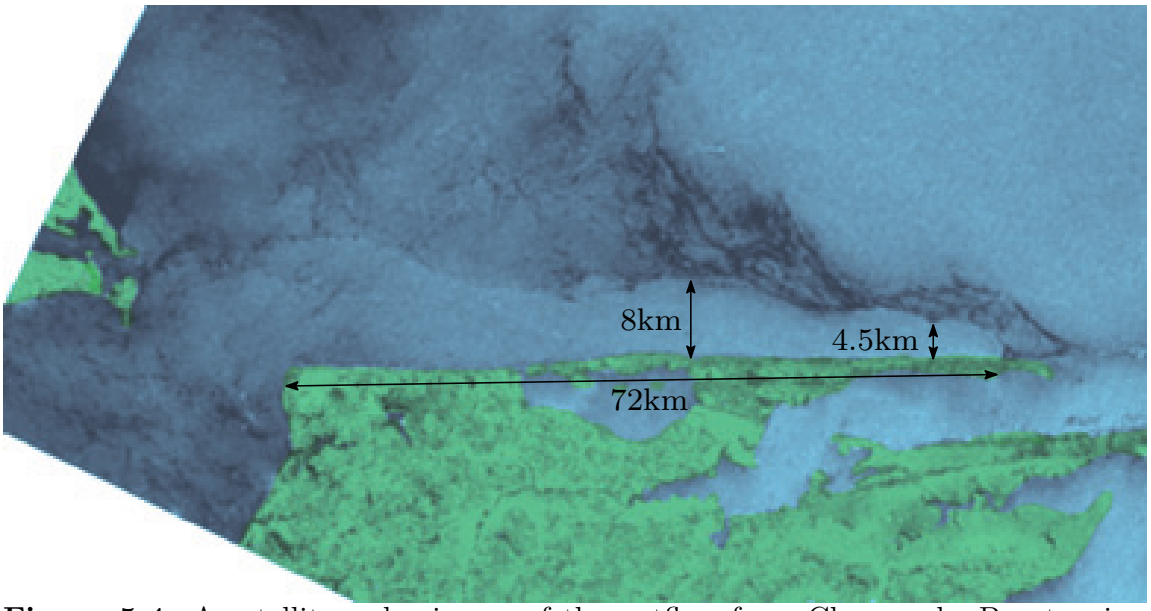

Figure 5.4: A satellite radar image of the outflow from Chesapeake Bay turning rightward and forming a coastal current reproduced from Donato and Marmorino [2002].

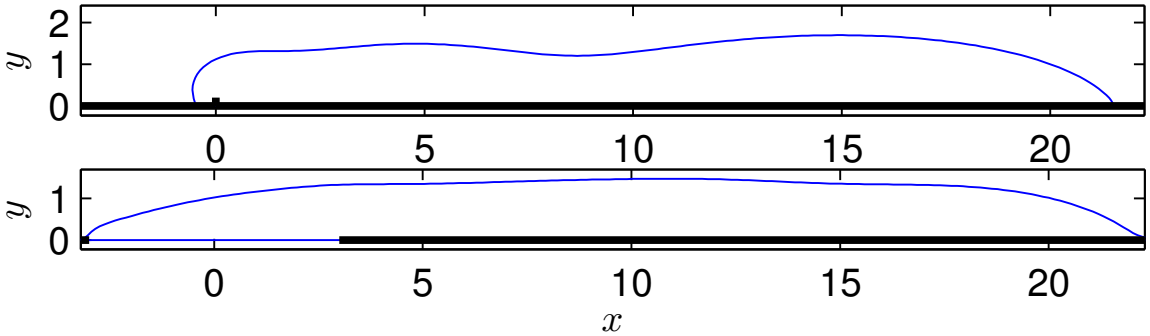

Figure 5.5: Contour dynamics simulations showing the profiles of positive PV outflows from a point source (top) and a uniform velocity source distributed from $x = -3$ to $x = 3$ (bottom) at time $t = 30$ for $Q_0 = 1$, $\Pi = 1$ and $L_\mathrm{R} = 2$ giving $a = 2$.

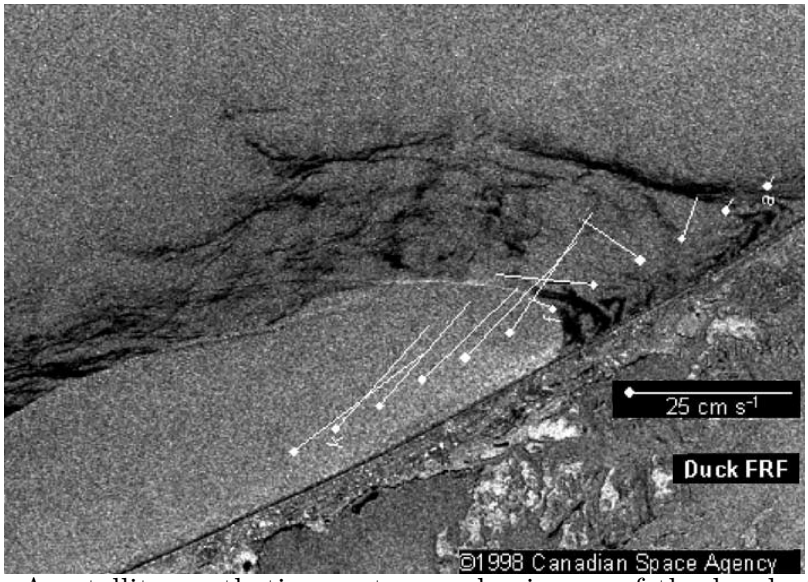

Figure 5.6: A satellite synthetic aperture radar image of the head of the Chesapeake Bay outflow reproduced from Donato and Marmorino [2002]. White lines show velocity vectors from later direct measurements.

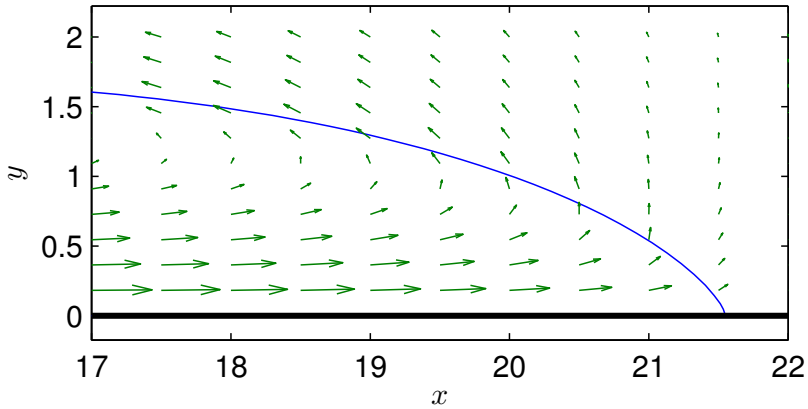

Figure 5.7: The head of a positive PV outflow from a point source for $Q_0 = 1$, $\Pi = 1$ and $L_\mathrm{R} = 2$ giving $a = 2$ at time $t = 30$. Velocity arrows are shown in green.

observed current speed and direction from later direct measurements, aligned to this satellite image. These show strong downstream flow near to the wall within the current which weakens and turns away from the coast at the edge of the current. There is then a backflow of the ambient fluid around the head and back towards the source. This is typical of a current with positive vorticity and, although other factors such as wind may influence the surface velocity, these results match well with velocity vectors produced by the QG model and displayed in fig. 5.7.

The outflow profiles for positive PV also bear a strong qualitative resemblance to the profiles of buoyant outflows in the rotating tank experiments of Thomas and Linden [2007] reproduced in fig. 5.8, particularly for $a \approx 1$. Both show constant

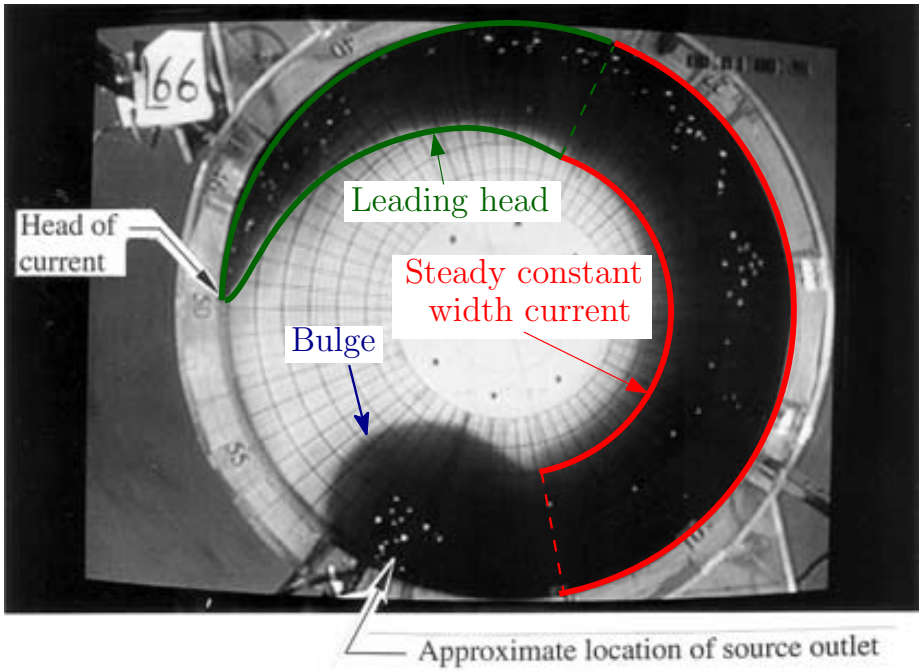

Figure 5.8: Experimental results from Thomas and Linden [2007] showing a buoyant outflow in rotating tank with a bulge joining to a constant width joining to a narrowing head.

width currents forming led by narrowing heads.

5.1.3 Outflow of negative PV fluid

For outflows of fluid with negative PV, the vorticity contributes a flux of negative x-momentum and drives the expelled fluid to the left, opposite to the rightward drainage pathway established by Kelvin wave radiation. The inverse Kelvin number a measures the relative importance of the vorticity to the source in the momentum balance. Thus for small a (high Kelvin number) the fluid is expected to predominantly turn rightward and for large a (small Kelvin number) to turn left. The evolution of the expelled fluid boundary over time for various values of a is shown in fig. 5.9. For small a the source dominates and the outflow closely resembles the zero PV outflow in fig. 5.1. For large a the vorticity dominates and the flow is driven leftward, with the solution for $a = 5$ similar to the rigid-lid solution. For moderate values of a, a bi-directional current forms. The agreement of these contour dynamics simulations with long wave theory is discussed in section 4.4 with fig. 4.7 being particularly relevant for the top two cases of fig. 5.9 and fig. 4.6 applying to the final case.

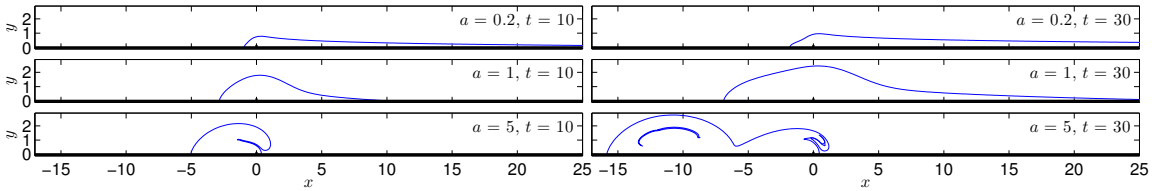

Figure 5.9: Contour dynamics results showing the boundary of a negative PV outflow driven by a point source at the origin at times t =10, 30, for $Q_0 = 1$, $\Pi = -1$ and $L_R = 0.2$, 1, 5, giving $a = 0.2$, 1, 5.

For $a \leq 1$ the bulge near the source grows indefinitely with logarithmically growing offshore displacement. Thus the source fluid is split between the growing bulge and the leftward and rightward currents. Steady, constant width currents flowing both leftward and rightward are possible, but are not observed to form in the initial value problem for wide sources, as predicted by the long wave theory. For narrow sources, contour dynamics results show that a steady leftward current can form but a steady rightward current has not been found for $a \leq 1$. The generic behaviour for these currents is to form rarefactions, i.e. thinning currents, the shape and velocity profile of which are accurately described by simple solutions of (4.11) (see chapter 4 for details). Thus, for $a \leq 1$, the evolution is in general unsteady. The only exception being a section of steady leftward current in the case of a narrow source.

When $a > 1$ the interface near the source evolves to a steady profile for all outflow velocity profiles. For wide sources this is given by the solution of (4.12) (see chapter 4) and for narrow sources it can be efficiently computed using the numerical scheme described in section 5.1.5. These steady solutions are led, as seen in the $a = 0.2$ and $a = 1$ results at $t = 30$ in fig. 5.9, by rarefying head profiles to each side, given by simple solutions of (4.11), again described in chapter 4. When a is above a critical value $a_c \approx 1.82$, the leftward rarefaction is overtaken and the steady solution terminates in a vortical head, as displayed for $a = 5$ in fig. 5.9.

5.1.4 Momentum balance and the turning of outflows

Analysing the momentum fluxes in a coastal outflow provides a useful tool to understand the turning of the current and the relative importance of different factors

in controlling this. Appendix B.1 considers a steady flow and integrates the nonlinear x-momentum equation of the rotating shallow water equations over the region S bounded by the curve ∂S, for either a large rectangular region or the region bounded by the outflow boundary $\partial\mathcal{D}$ and $x = \pm R$ for large R, and shows that QG flow trivially satisfies the leading order geostrophic balance, but that a steady flow must also balance the momentum fluxes through the boundaries of the domain

$$\oint_{\partial S} uv \, \mathrm{d}x = \oint_{\partial S} u^2 \, \mathrm{d}y. \tag{5.2}$$

The first term in (5.2) is the x-momentum flux into the domain through the source, hereafter labelled ΔM_s. The second term is the flux of momentum out of the domain in the downstream and upstream currents, hereafter labelled ΔM_c. For unsteady flows, deviation from this balance is due to changes in the total momentum within the control domain. Thus this equation can be used to understand the turning of the current. If the x-momentum flux through the source is positive then the current must ultimately turn rightward (where $\mathrm{d}y > 0$), if it is negative then the current must turn left (where $\mathrm{d}y < 0$). The current can be turned either by the effect of rotation or the vorticity of the current. For source profiles where $v(x, 0)$ is symmetric in x, the source momentum will be zero and the current will be symmetric in x if $u(x, 0) = 0$ or $u(x, 0)$ is an odd function of x, as it is for outflows unaffected by rotation or vorticity. For flows affected by vorticity or rotation, $u(x, 0)$ has an even component which gives a momentum flux at the source and turns the current.

5.1.4.1 Momentum flux due to rotation

Appendix B.2 derives the velocity field due to both finite width and point sources for QG flow. (B.16) gives the alongshore velocity u for a QG point source and shows that it consists of an odd singular component (2^{nd} term), a finite odd component (3^{rd} term) and a finite even component (1^{st} term). Close to the source the flow is dominated by the odd singular part, but the finite even component still contributes to the momentum flux and it is this that is ultimately responsible for turning the current. For finite width sources (B.13) shows that u has an even component equal to $Q_0 \exp(-y/L_\mathrm{R})/2L_\mathrm{R}$ (as well as an odd component).

For a zero PV outflow, the velocity field is given by (B.16) and (B.14) so, far downstream, $\Delta M_{\mathrm{c}} = Q_0^2/2L_{\mathrm{R}}$ and, noting that the odd components of u contribute nothing to the integral, $\Delta M_{\mathrm{s}} = Q_0^2/2L_{\mathrm{R}}$ showing that momentum is conserved for this steady flow. For a finite width symmetric source of zero PV fluid the source flux is also equal to $Q_0^2/2L_{\mathrm{R}}$ (the contribution from the first term in (B.13), the second term is odd in x so makes no contribution) and the downstream flux is the same so this steady solution also conserves momentum.

5.1.4.2 Momentum flux due to vorticity and rotation

In the previous examples rotation was entirely responsible for turning the outflow. For vortical outflows, vorticity will also play a role in turning the outflow and for rigid-lid flows, rotation has no effect and vorticity is solely responsible for turning the flow. At the source the integral of the product of the non-symmetric u due to the vorticity and the singular v due to the source gives a momentum flux into the domain. For rigid-lid outflows there is initially no momentum flux and the outflow is symmetrical. Over time the vorticity driven cross-flow increases, increasing the momentum flux and turning the current rightward. The flow evolves to a steady state where the momentum fluxes at the source and downstream in the current match.

Johnson and McDonald [2006] give the analytical steady solution for the fluid velocity everywhere within the domain. In complex variable form this is

$$z = \frac{2\mathrm{i}Q_0}{\pi} w_1 \log\left(\frac{w_1 - \mathrm{i}\sqrt{2Q_0\Pi}}{w_1}\right) - \sqrt{\frac{2Q_0}{\Pi}}\frac{1}{\pi}, \tag{5.3}$$

which relates the position $z = x + \mathrm{i}y$ to the function $w_1 = \mathrm{i}\Pi y + v + \mathrm{i}u$, which gives the velocity. The interface profile can then be found by setting $u = v = 0$. As $z \to 0$, $w_1 \to \infty$, so expanding for large w_1 and small z gives

$$z = \frac{2\mathrm{i}Q_0}{\pi w_1} - \frac{\sqrt{8Q_0^3\Pi}}{3\pi w_1^2} + \mathcal{O}(w_1^{-3}), \tag{5.4}$$

which can be rearranged to find

$$w_1 = \frac{\mathrm{i}Q_0}{\pi z} + \frac{\mathrm{i}}{3}\sqrt{8Q_0\Pi} + \mathcal{O}(z). \tag{5.5}$$

This form splits the velocity at the source into the irrotational, singular, symmetric component due to the source (1st term) and the finite component due to the vorticity (2nd term), with u-component equal to $\sqrt{8Q_0\Pi}/3$. Integrating this against the delta function offshore velocity gives the momentum flux $\Delta M_\mathrm{s} = \sqrt{8Q_0^3\Pi}/3$. The downstream momentum flux can be computed by integrating the linear downstream velocity profile $u = \Pi(Y - y)$ where the downstream current width is $Y = \sqrt{2Q_0/\Pi}$ giving $\Delta M_\mathrm{c} = \sqrt{8Q_0^3\Pi}/3$ and matching to the source momentum flux.

For outflows of non-zero PV both rotation and vorticity contribute to the source momentum flux and the turning of the current. The momentum fluxes for these outflows can be computed numerically. Examples of the evolution of the fluxes over time are shown in fig. 5.10 for $Q_0 = 1$, $\Pi = 1$ and $L_\mathrm{R} = 0.5$, 1, 2. The momentum fluxes entering at the source and leaving downstream across the line $x = 10$ are plotted separately. When the currents reach a steady state these two fluxes become equal with only some small oscillation in the downstream flux due to the interfacial Rossby waves. Initially there is no momentum flux due to vorticity and the source and downstream fluxes are both equal to $Q_0^2/2L_\mathrm{R}$, the zero PV fluxes. This initial value of ΔM_s as a fraction of the final value shows how important rotation is in turning the current. The moment when the vortical current arrives at the line $x = 10$ can clearly be seen as a sharp increase in ΔM_c from $Q_0^2/2L_\mathrm{R}$.

5.1.4.3 Momentum balance for long wave solutions

Appendix B.3 calculates the momentum fluxes for steady long wave solutions of (4.12) and (4.10) for a domain bounded by the outflow boundary $\partial\mathcal{D}$ and $x_1 < x < x_2$ for arbitrary x_1, x_2, L_R, Q_0, Π and an arbitrary source profile. The source flux is given by (B.19) and the flux in the alongshore current is given by (B.21), showing that, for all parameter values and source profiles

$$\Delta M_\mathrm{s}(x_1, x_2) = \Delta M_\mathrm{c}(x_2) - \Delta M_\mathrm{c}(x_1), \tag{5.6}$$

and the flow conserves momentum.

The momentum imbalance paradox [Pichevin and Nof, 1997] stems from assuming $u(x, 0)$ is odd and therefore neglecting the flux of momentum at the source. However,

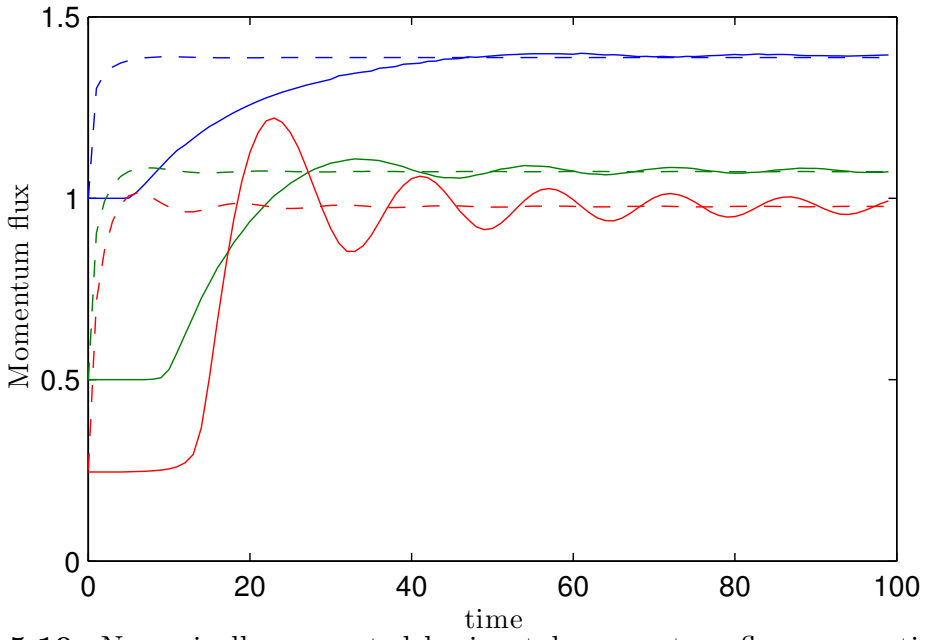

Figure 5.10: Numerically computed horizontal momentum fluxes over time from the source ΔM_s (dashed) and across the line $x = 10$ ΔM_c (solid) for outflows with $Q_0 = 1$, $\Pi = 1$ and varying $L_\mathrm{R} = 0.5$ (blue), 1 (green) and 2 (red).

when this momentum flux is included the paradox is resolved and steady solutions are in fact possible.

5.1.5 Steady profiles

5.1.5.1 An iterative scheme to compute steady profiles

If a steady solution exists then its boundary $y = Y(x)$ is a streamline of the flow. The problem to solve for a steady profile is

$$\mathcal{L}\eta = \begin{cases} 0, & y > Y(x) \\ \Pi, & 0 < y < Y(x), \end{cases} \tag{5.7}$$

where the operator $\mathcal{L} = \nabla^2 - L_\mathrm{R}^{-2}$. This is combined with the boundary conditions that the streamfunction matches the far-downstream behaviour of a constant width current given by (4.10), $\eta = Q(x)$ on $y = 0$, $\eta \to 0$ as $y \to \infty$ and the additional condition that $\eta = Q_\mathrm{e}$ on $y = Y(x)$. In a finite rectangular domain, these boundary conditions can be applied on the edges of the domain used to solve (5.7).

A solution of this problem is found iteratively. Discretise the problem with first

order centred finite differences on a regularly spaced finite grid to give the matrix operator $\mathbf{A}$. Let $\boldsymbol{\eta}_n$ and $\boldsymbol{\Pi}_n$ be the vectors giving the value of the η and Π at each grid point at the n^{th} iteration. Now for a given free surface, $\boldsymbol{\Pi}_n$ is known and the streamfunction can be found as $\boldsymbol{\eta}_n = \mathbf{A}^{-1}\boldsymbol{\Pi}_n$. The values of the streamfunction can then be used to update $\boldsymbol{\Pi}_n$ for the next iteration. Given $\boldsymbol{\eta}_n$, the location of the boundary Y can be identified, for each value of x, by tracking from large to small y and finding the first instance where $\eta > Q_{\text{e}}$. This point and all below it must be within the expelled fluid. Denote this approach as $\boldsymbol{\Pi}_{n+1} = \chi(\boldsymbol{\eta}_n)$. For positive PV, Y can be a multivalued function of x so the alternative method $\chi(\boldsymbol{\eta}_n) = \Pi H(\boldsymbol{\eta}_n)$, for the element-wise Heaviside function H (where the entries of $H(\boldsymbol{x})$ are 1 where the corresponding element of $\boldsymbol{x}$ is strictly positive and 0 otherwise), is used. For improved stability an under-relaxed version of the method can be used by updating $\boldsymbol{\Pi}_n$ at each timestep with a fraction α based on this method (in the results below $\alpha = 0.05$ has been used) and a fraction $1 - \alpha$ of its previous value.

This method gives the iterative scheme

$$\boldsymbol{\eta}_n = \mathbf{A}^{-1}\boldsymbol{\Pi}_n, \tag{5.8a}$$

$$\boldsymbol{\Pi}_{n+1} = \alpha\chi(\boldsymbol{\eta}_n) + (1 - \alpha)\boldsymbol{\Pi}_n. \tag{5.8b}$$

For the initial value $\boldsymbol{\Pi}_1$ some approximation must be used. For positive PV the rigid-lid profile, but scaled in size to match to the steady x-independent current can be used, and for negative PV a smooth monotonic function matching the left and right steady solutions can be used. The entries of $\boldsymbol{\Pi}_1$ are Π if the grid-point is within this contour and 0 if it is outside.

Steady solutions for positive PV calculated using this method are shown and compared to contour dynamics results in figure 5.11. By time $t = 30$ the contour dynamics results are very close to the steady solutions with the only differences due to the initial transience, still visible in the form of interfacial Rossby waves moving to the right. The results of the iterative scheme for $a = 10^5$ were compared to the exact solution in the rigid-lid limit and found to be graphically indistinguishable.

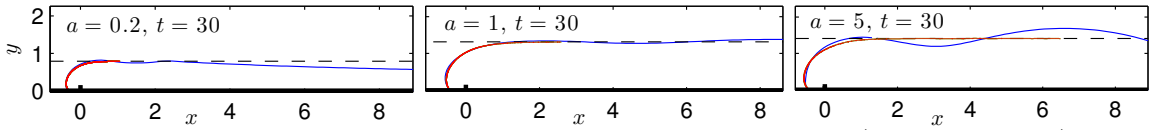

Figure 5.11: A snapshot of the outflow boundary at $t = 30$ (solid blue line) computed with contour dynamics and the steady profile (solid red line) computed with the iterative scheme for an outflow with $Q_0 = 1$, $\Pi = 1$ and $L_\mathrm{R} = 0.2$, 1, 5, giving $a = 0.2$, 1, 5. The width of a steady x-independent current is shown as a dashed black line.

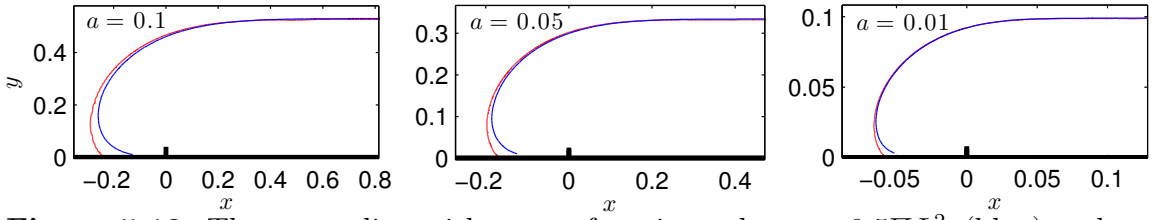

Figure 5.12: The streamline with streamfunction value $\eta = 0.5\Pi L_\mathrm{R}^2$ (blue) and an iteratively computed steady profile (red) for outflows with $Q_0 = 1$, $\Pi = 1$ and (left to right) $L_\mathrm{R} = 0.1$, 0.05, 0.01, giving $a = 0.1$, 0.05, 0.01, showing the steady solution converging to the streamline of the source flow as a decreases.

5.1.5.2 Steady profile for $a \ll 1$

Analytical solutions for steady profiles in the rigid-lid limit $a \to \infty$ were derived by Johnson and McDonald [2006]. For the limit $a \to 0$ and negative PV a steady solution is not possible, and for positive PV and small a the dynamics are dominated by the source and the steady solution is given by the contour of the streamfunction due to the source that matches to the constant width current i.e. the contour that asymptotes to $y = Y$ as $x \to \infty$.

In the case of a point source, for example, (B.15) gives the streamfunction due to the source. The value of η on the bounding streamline of the steady solution is

$$\eta = Q_0 \mathrm{e}^{-\frac{Y}{L_\mathrm{R}}} \approx \frac{\Pi L_\mathrm{R}^2}{2}, \tag{5.9}$$

for small a. So the steady solution for a point source outflow of positive PV fluid when a is small can be computed by equating (B.15) with $\Pi L_\mathrm{R}^2/2$.

Results showing the steady contour computed using the above asymptotic solution are compared to the iterative scheme in figure 5.12 for $a = 0.1$, 0.05 and 0.01.

5.2 Unsteady sources, currents, winds and tides

5.2.1 Variable strength outflows

Variations in the volume flux of coastal outflows, which can vary by as much as an order of magnitude [Horner-Devine et al., 2015, van Maren and Hoekstra, 2004], can be represented using a source with time-dependent strength. This section considers both strengths oscillating around an average value and those transitioning from one constant value to another as prototypical examples. A periodically varying outflow can be represented by a source with strength varying sinusoidally between two values $Q_{\min}$ and $Q_{\max}$ with period T i.e. a source with strength

$$Q_0(t) = \frac{Q_{\max} - Q_{\min}}{2} \sin\left(\frac{2\pi t}{T}\right) + \frac{Q_{\max} + Q_{\min}}{2}. \tag{5.10}$$

For zero PV outflows the linearity of the problem means that, by the end of a period, a variable strength outflow has evolved to the same profile as a constant strength source with the same average flux. It is only through interaction with the nonlinear vortical dynamics that varying the source strength can change the evolution across a full period. Therefore the source-dominated rightward rarefaction is expected to be relatively unaffected by the variable strength.

Figure 5.13 shows results for a strongly varying source ($Q_{\min} = 0.2$, $Q_{\max} = 1$) for a large range of periods $T = 40, 10, 2$ compared to a constant strength source with the same average flux $Q_0 = 0.6$ for an outflow of negative PV fluid. The profiles are plotted at $t = 40$ where they have all completed an integer number of periods. While there is reasonable variability over an outflow cycle, by the end of a complete period the results are very similar, even for such a strongly varying source and such a large range of periods. The biggest difference from the constant strength source are the results for the longest period outflow $T = 40$ but even these are still very similar. This suggests that, at least for QG dynamics, oscillations of outflow strength may not be a significant dynamical factor and that models which average this outflow flux may be providing a good representation of the dynamics.

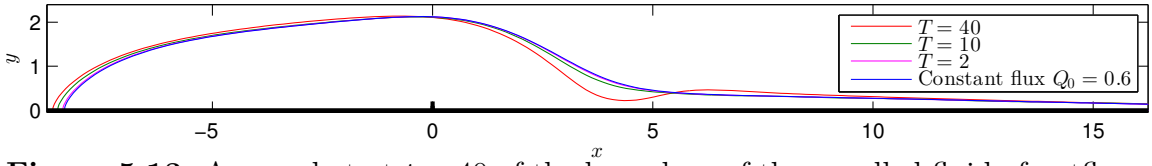

Figure 5.13: A snapshot at $t = 40$ of the boundary of the expelled fluid of outflows with strength sinusoidally varying between $Q_{\min} = 0.2$ and $Q_{\max} = 1$ for variation periods $T = 40, 10, 2$ compared to a constant flux outflow of strength $Q_0 = 0.6$. In each case $\Pi = -1$ and $L_{\mathrm{R}} = 1$.

The effects of varying outflow strength can be analysed using long wave theory. As an example, consider an outflow which starts at one strength Q_1, before smoothly changing to a second constant strength Q_2 i.e. the outflow with

$$Q_0(t) = \begin{cases} Q_1, & t \leq T \\ \frac{Q_1+Q_2}{2} + \frac{Q_1-Q_2}{2}\cos\left(\frac{\pi(t-T)}{T}\right), & T < t \leq 2T \\ Q_2, & t > 2T. \end{cases} \tag{5.11}$$

Provided that the timescale T is not small, the solution for this outflow is accurately given by the long wave approximation and may be found analytically by integrating along the characteristics of (4.11) (see chapter 4 for the details of this procedure). An example comparing the analytical solution to contour dynamics for $L_{\mathrm{R}} = 0.7$, $\Pi = 1$, $Q_1 = 1$, $Q_2 = 1.5$ and $T = 250$ is shown at time $t = 750$ in fig. 5.14. The period $T = 250$ has been selected to best display the long time accuracy of the analytical solution.

The various profiles possible are best understood by analysing the wave speed $c(Z) = \Pi L_{\mathrm{R}} Z\,(1 + Q/L_{\mathrm{R}}^2\Pi - Z)$ of long waves from (4.11). This has a maximum at $Z = Q/2L_{\mathrm{R}}^2\Pi$, noting that $0 < Z \leq 1$ with $Z = 1$ corresponding to a zero width current and the current width increasing as Z decreases. This wave speed is displayed for the two cases $Q/L_{\mathrm{R}}^2\Pi \geq 1$ and $Q/L_{\mathrm{R}}^2\Pi < 1$ with positive PV in fig. 5.15. The outflow in fig. 5.14 corresponds to $Q/L_{\mathrm{R}}^2\Pi \geq 1$ where a thicker current close to the source (point A) is connected to a thinner current downstream (point B). As the wave speed increases in the downstream direction between the two they can be joined by a rarefaction and the forward current can be joined by a rarefaction to the wall (point C). If, however, the rear current was thinner (point B), it could not join smoothly to a thicker current downstream (point A) because the wave speed would decrease

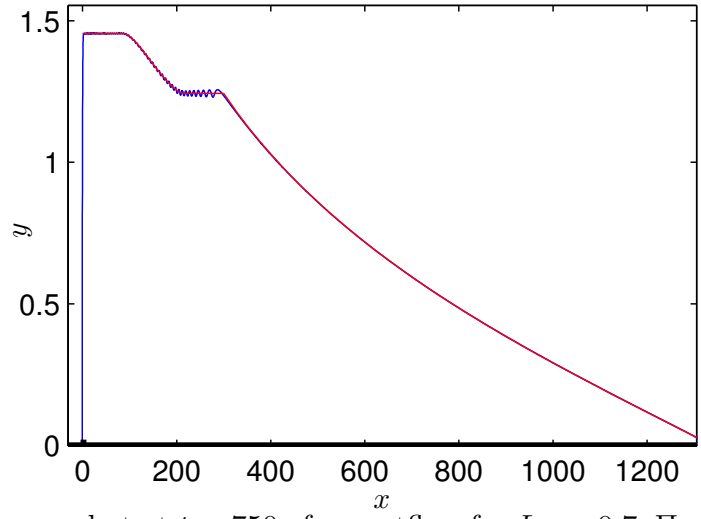

Figure 5.14: A snapshot at $t = 750$ of an outflow for $L_\mathrm{R} = 0.7$, $\Pi = 1$ with strength varying from $Q_1 = 1$ for $t < 250$ smoothly up to $Q_2 = 1.5$ for $t > 500$. The result of a contour dynamics simulation is shown in blue and the analytical solution is shown in red. Across the leading rarefaction and rear constant width current these are indistinguishable. Note that the axes are scaled to fit the whole outflow.

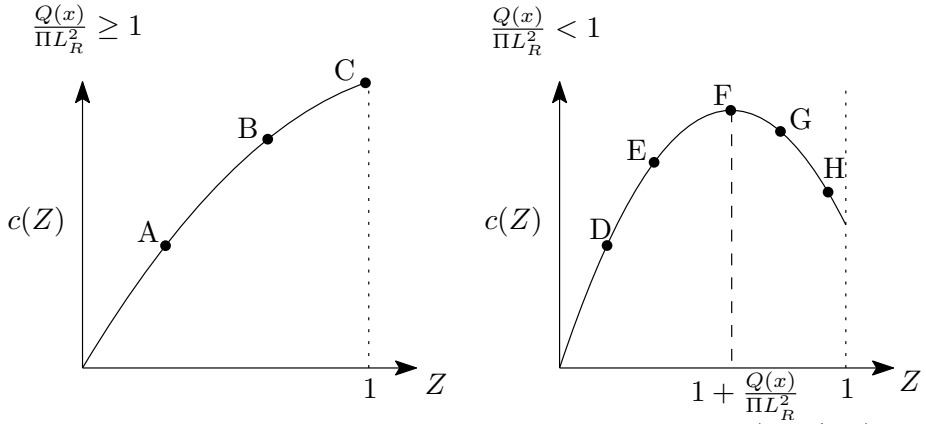

Figure 5.15: The long wave speed c as a function of $Z = \exp(-Y/L_\mathrm{R})$ for the two cases $Q(x)/\Pi L_\mathrm{R}^2 \geq 1$ and $Q(x)/\Pi L_\mathrm{R}^2 < 1$.

in the downstream direction and a shock would form. This shock would be resolved by the full two-dimensional dynamics into a series of waves. If $Q/L_\mathrm{R}^2\Pi < 1$ then the forward thinner current (point E) cannot connect to $Z = 0$, instead it rarefies until near point F where a shock forms. For $Q/L_\mathrm{R}^2\Pi < 1$, it is also possible to have smooth solutions with $Q_2 < Q_1$ where a thinner current near the source (point H) can smoothly join to a thicker current downstream (point G). This constant width current cannot thin further so must end in a shock. For negative PV, the wave speed can be negative, giving leftward currents with the analysis following similarly.

5.2.2 Alongshore currents

Ambient alongshore currents can have significant effects on coastal outflows. Downstream currents support the turning of the outflow and inhibit the growth of a bulge near the source. Fong and Geyer [2002] investigated the effects of a downstream current on a coastal outflow in a numerical model and found that even weak downstream currents were sufficient to halt bulge growth and confine all the outflow flux to the coastal current. The Delaware River plume is influenced by a downstream current which, in conjunction with the downstream angle of the outflow, inhibits any bulge formation and confines the entire flux to the coastal current. The Amazon River plume, while unaffected by rotation, is influenced by alongshore currents which carry a significant flux of fresh Amazon water northward into the Northern Hemisphere. Where the ambient current is oriented upstream, as in the case of the Columbia River outflow [Hickey et al., 2005], a bidirectional plume can be formed with a fraction of the outflow flowing upstream, a fraction downstream and, in some cases, a fraction feeding a growing bulge.

Matano and Palma [2010a] investigate the formation of bidirectional currents using the Princeton Ocean Model. They argue that the common practice of imposing a downstream ambient current to inhibit upstream spreading and bulge formation is unjustified and that bidirectional currents are a robust feature of numerical models. They show that although, as identified by Yankovsky [2000] and Garvine [2001], many aspects of the model set up affect and inhibit upstream spreading, none of these completely stop upstream spreading. They show that the adjustment of the flow generates a positive baroclinic pressure gradient driving the flow upstream. In their model the fluid adjusts to a deeper level than the outflow source, consistent with the generation of negative vorticity. In an accompanying note [Matano and Palma, 2010b] they show that if the buoyant discharge is stopped then all the fluid turns and moves upstream, a conclusion supported by the negative PV results here.

The effects of alongshore currents can be incorporated into the QG model by adding an additional background current with rightward flux Q_c. That is, a current with streamfunction

$$\eta_\mathrm{c} = Q_\mathrm{c} \mathrm{e}^{-y/L_\mathrm{R}}. \tag{5.12}$$

The results examined in section 5.1 are for the special case $Q_c = 0$. The case $Q_c = -Q_0$, an upstream current with flux equal to that of the source, is particularly interesting. Examining the exact solutions for the source profile in general (B.13) or for a point source (B.15) shows that this case is equivalent to the standard $Q_c = 0$ problem with the source profile reflected in x (a Southern Hemisphere outflow) as these profiles have a component independent of x equal to $Q_0 \exp(-y/L_R)/2L_R$ and a component which is an even function of x. Thus the outflow evolution for negative and positive PV are reversed for this value of Q_c. That is, the outflow evolution for $Q_c = -Q_0$, with generated vorticity Π is identical to the outflow for $Q_c = 0$ with generated vorticity $-\Pi$, reflected in the y-axis. Thus, the earlier results for negative PV can equally be interpreted as results for positive PV against an ambient current in the Southern Hemisphere.

For $Q_c = -Q_0/2$ the flow due to the source and current combined is symmetrical so contributes no momentum flux. Thus, as for rigid-lid outflows, the only asymmetry is due to the vorticity and positive and negative PV outflows are simply reflections of each other. A zero PV ($a = 0$) outflow splits and flows equally left and right with an initially semi-circular profile which flattens over time into rarefying currents to the left and right.

For the rest of this subsection, only the case for positive PV is considered (negative PV solutions can be recovered by reflecting $Q_c \to -Q_0 - Q_c$ and $x \to -x$) and the outflow is a two parameter problem dependent on a and Q_c/Q_0. As discussed in section 4.2.2, analysing the long wave equations (4.12) and (4.11), the behaviour of outflows can be classified in $(Q_c/Q_0, a)$ parameter space as shown in Figure 5.16. The standard cases of a positive PV outflow without a background flow and a negative PV current without a background flow lie on the lines $Q_c/Q_0 = 0$ and $Q_c/Q_0 = -1$ respectively. Dependent on Q_c/Q_0 and a there is either a single rightward steady current (right-hand green region), steady currents in both directions (blue region), no steady currents (red region) or a steady leftward current (left-hand green region). The width and velocity profiles across these steady currents are the simple solutions to (4.12) and (4.10). These steady solutions join onto constant width currents which are led by simple rarefying solutions to (4.11),with the only exception is for $a \geq \sqrt{Q_c/Q_0 + 1}$ (the area above the purple line in fig. 5.16) where the rightward steady

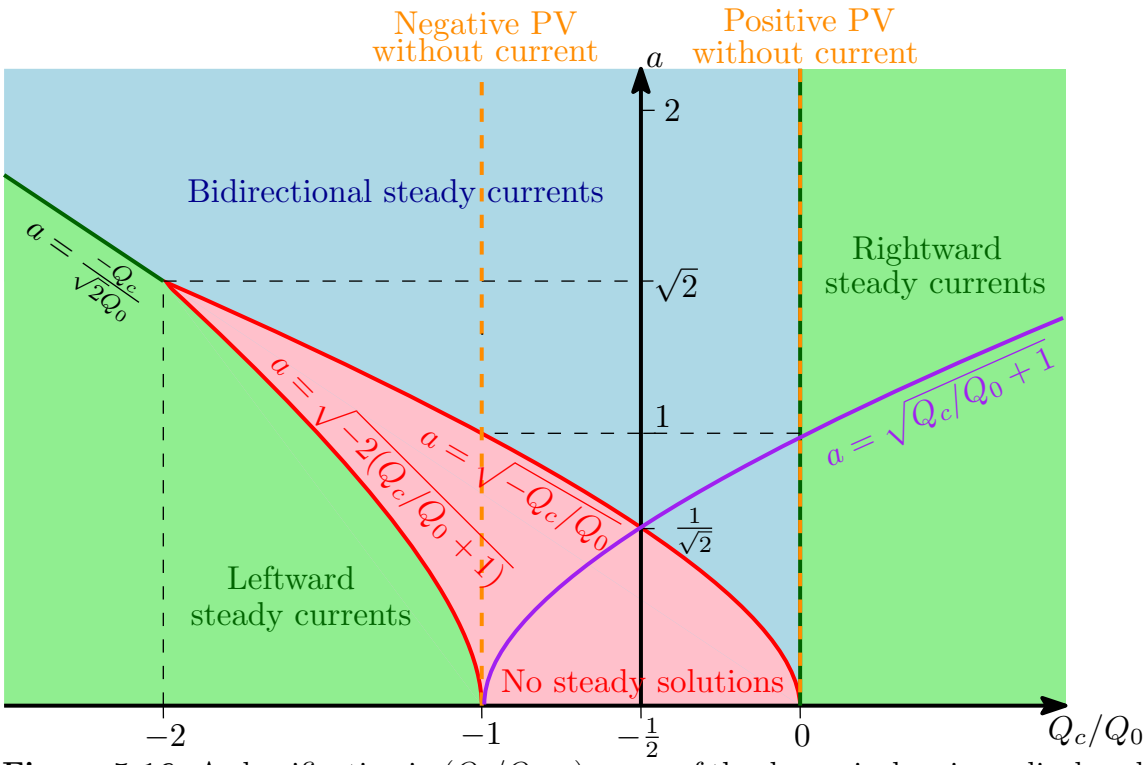

Figure 5.16: A classification in $(Q_c/Q_0, a)$-space of the dynamical regimes displayed in an outflow with an ambient current of strength Q_c. Above the purple line rightward rarefactions must end in a shock.

current is led by a rarefaction that terminates in a shock. This corresponds to the situation in the second panel of fig. 5.15 where a steady current (point E) rarefies to a shock (near point F) because at the shock the wave speed starts to decrease in the downstream direction. As a increases further the size of the rarefaction decreases until there is only a shock, which is resolved by the full two-dimensional dynamics to a head profile as seen in, for example, the lower panels of fig. 5.2 and for rigid-lid outflows.

Thus, ambient currents can have very significant effects on the outflow dynamics when the flux they carry is comparable to the source flux. The outflow dynamics with an ambient current form four main behaviours, three of which (single rightward current, bidirectional currents and no steady currents) have already been shown in detail in the earlier discussion of positive and negative PV outflows without ambient currents in section 5.1 (see figs. 5.2 and 5.9). An example of the final case, a leftward steady current, is shown in fig. 5.17 for $Q_c = -2$, $\Pi = 1$, $Q_0 = 1$, $L_R = 1$, giving $a = 1$ and $Q_c/Q_0 = -2$. There is a steady profile across the source region joining on its left to a steady constant width current led by a rarefaction which are accurately

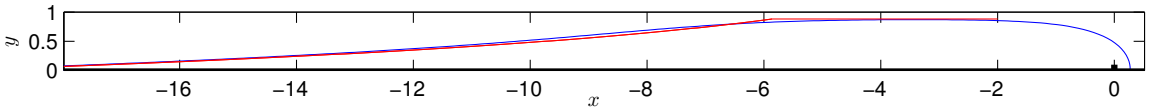

Figure 5.17: A snapshot at time $t = 10$ of a contour dynamics simulation (blue) and the long wave analytical solution (red) for an outflow from a point source for $Q_0 = 1$, $\Pi = 1$, $L_\mathrm{R} = 1$, giving $a = 1$, with a background current of strength $Q_\mathrm{c} = -2$. $Q_\mathrm{c}/Q_0 = -2$ is less than the critical value of $-3/2$ so a steady leftward current with constant width has formed, led by a rarefaction.

described by the analytical solution as shown.

The results here match well to those of Fong and Geyer [2002] and Hickey et al. [2005]. Weak alongshore currents inhibit bulge growth and transfer the entire outflow flux into the downstream current in the simulations of Fong and Geyer [2002], corresponding to moving from the red area with a growing bulge in fig. 5.16 to the green area $Q_\mathrm{c}/Q_0 > 0$ when a small alongshore current is included. The introduction of an antagonistic current causes a bidirectional current to form both here and in the observations and simulations of Hickey et al. [2005].

5.2.3 Tides

Numerical models [Chen, 2014, Isobe, 2005] show that one of the main effect of tides on outflows is to increase the alongshore transport and reduce the growth of the bulge. This is supported by observations, for example measurements of the strongly tidally influenced outflow of the Changjiang (Yangtze) River found 90% of the freshwater flux enters the coastal current [Wu et al., 2013]. Isobe [2005] investigated the effect of tides and the role of inertial instability in the growth of the bulge in a numerical model for moderate Rossby number. He found that tides stabilised and halted the growth of the bulge and increased the alongshore transport. Isobe's figure 14 shows model results for a variety of outflow and tidal strengths. The larger outflow results display the classic circular, inertia driven bulge when the tidal forcing is weak. For stronger tidal forcing the bulge is broken up and the results start to resemble a lower Rossby radius outflow, suggesting that tides may limit the role of inertia. For lower outflow velocity, Isobe's results, which have anticyclonic vorticity, look very similar to QG outflows for negative PV and low a (see fig. 5.9 $t = 10$, $a = 1$).

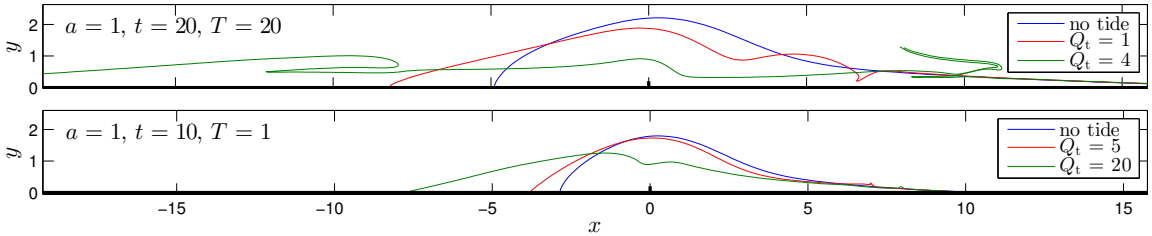

Figure 5.18: Simulations of outflows for $Q_0 = 1$, $\Pi = -1$ and $L_R = 1$, giving $a = 1$, with tidal forcing of various strengths and periods. The top panel shows a snapshot after one tidal period of an outflow with tidal forcing of period $T = 20$ and strengths $Q_t = 1$ and $Q_t = 4$ compared to the unforced case. The bottom panel shows a snapshot at $t = 10$ of an outflow with tidal forcing of period $T = 1$ and strengths $Q_t = 5$ and $Q_t = 20$ compared to the unforced case.

The effects of tides can be investigated in the QG model by adding an additional periodically varying ambient current of the form

$$\eta_t = Q_t \sin(2\pi t/T) \exp(-y/L_R), \tag{5.13}$$

with maximum flux Q_t and period T. This addition could be thought of as horizontally varying the position in parameter space in fig. 5.16 i.e. periodically varying Q_c. This contrasts to the variable strength outflow which was a vertical variation in $(Q_c/Q_0, a)$ parameter space i.e. varying a. Examples of solutions with this tidal forcing are shown in fig. 5.18 for short and long periods $T = 1$ and $T = 20$ and various tidal strengths for a negative PV outflow.

There are many similarities to the variable strength outflows shown in section 5.2.1. The longer the period of the forcing, the greater effect there is on the evolution of the outflow. Also, the right-hand rarefaction (which is dominated by the source) is again virtually unchanged by the forcing, which can only affect the ultimate outflow evolution through interaction with the nonlinear vortical dynamics. However tides have a much more significant effect than a variable strength outflow. Tidal forcing spreads the outflow horizontally, particularly in the direction of propagation due to the vorticity. This is achieved by inhibiting the growth of the bulge near the source. For long periods, a tide with maximum flux equal to the source is able to significantly disrupt the outflow. For short periods, the tide needs a flux an order of magnitude larger than the source to provide significant disruption.

The average speed of a leftward vortical layer, as a function of the layer width Y,

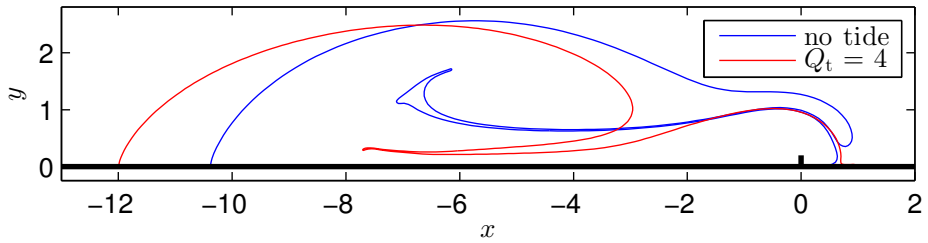

Figure 5.19: A snapshot at $t = 20$ of simulations of a negative PV outflow for $Q_0 = 1$, $\Pi = -1$ and $L_R = 5$, giving $a = 5$ with (red) and without (blue) tidal forcing of strength $Q_t = 4$ and period $T = 20$.

is proportional to $(1 - \exp(-Y/L_R))^2/Y$, which has a maximum at $Y \approx 1.25643 L_R$. If the current width, as the outflow is spread by tides, gets closer to this value then vorticity will drive the current further leftward as seen in fig. 5.18. However, if the unforced outflow is thinner than this value then spreading the current will slow its leftward propagation and the tides will have less effect. An example of this situation for $a = 5$ is shown in fig. 5.19. Here, a tide with strength $Q_t = 4$ and period $T = 20$ has much less effect than it did for $a = 1$ in the top panel of fig. 5.18.

5.2.4 Wind forcing

Wind stress can significantly affect river plumes through the Ekman response of the near surface fluid. Winds oriented in the downstream direction push surface water towards the coast and drive downwelling, further focussing the outflow against the coast. Upstream oriented winds have the opposite effect, pushing water and the coastal current away from the coast and driving upwelling. Typically this results in currents separated from the coastline with rounded heads as seen in the observations of Gulf of Maine plume [Fong et al., 1997], Columbia River outflow [Hickey et al., 1998] and the Chesapeake Bay outflow [Dzwonkowski and Yan, 2005] as well as in the numerical simulations of Hickey et al. [2005].

Dzwonkowski and Yan [2005] traced the outflow from Chesapeake Bay in satellite-measured ocean colour data over time under varying wind conditions. Figure 5.20 reproduces their figure 8 which shows the plume evolution over 5 days. For the first three days there are southward winds driving downwelling or weak variable winds. For the fourth and fifth days there are northward winds driving upwelling. Under downwelling favourable winds the current remains close to the coast and evolves

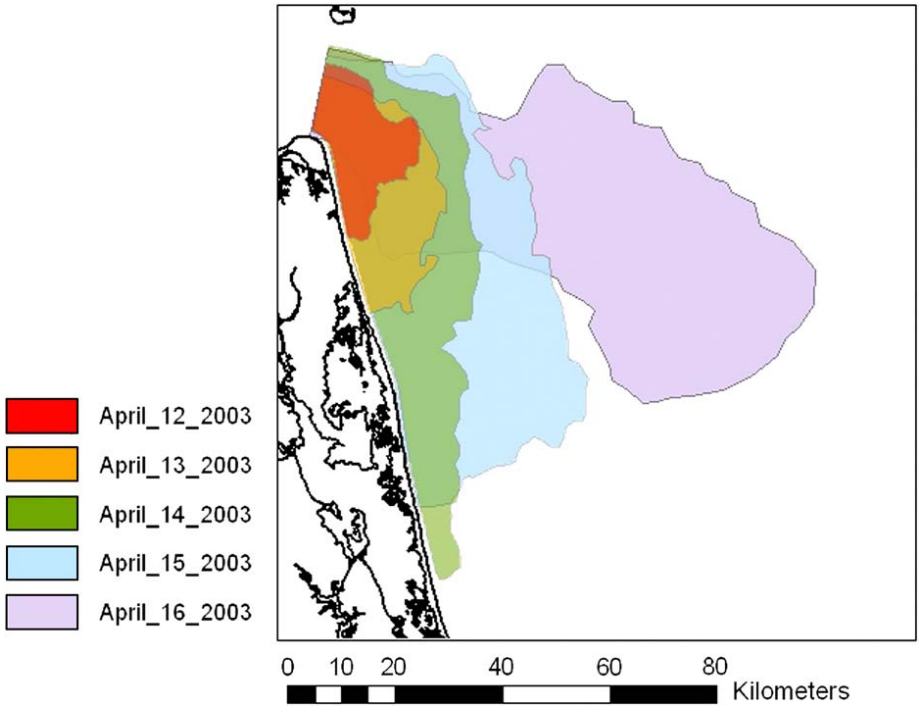

Figure 5.20: Area of the Chesapeake outflow plume over five days with downwelling-favourable or varying winds becoming upwelling-favourable on the last two days, as measured by satellite-based ocean colour data reproduced from Dzwonkowski and Yan [2005].

similarly to the observations of Donato and Marmorino [2002] reproduced in fig. 5.4 and the QG results presented here so far. Under the upwelling favourable winds, surface water is pulled away from the coast and the plume quickly follows moving away from the shore and retreating back toward the source. Its final profile is much more rounded than the alongshore nose after day 3.

The upwelling or downwelling caused by winds can be qualitatively represented in the QG model of outflows by adding a continuous source along the extent of the wall. A source with flux per unit length Q_w through the wall $y = 0$ has streamfunction

$$\eta_\mathrm{w} = Q_\mathrm{w} x \mathrm{e}^{-y/L_\mathrm{R}}, \tag{5.14}$$

giving

$$\begin{pmatrix} u_\mathrm{w} \\ v_\mathrm{w} \end{pmatrix} = \begin{pmatrix} Q_\mathrm{w} x / L_\mathrm{R} \\ Q_\mathrm{w} \end{pmatrix} \mathrm{e}^{-y/L_\mathrm{R}}. \tag{5.15}$$

Figure 5.21 shows an example of simulations with various wind strengths compared to the results without wind for an upwelling favourable wind. The upwelling

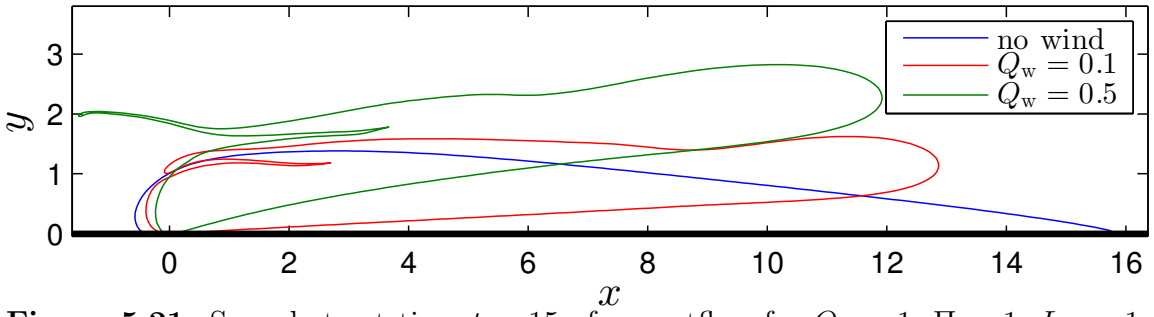

Figure 5.21: Snapshots at time $t = 15$ of an outflow for $Q_0 = 1$, $\Pi = 1$, $L_R = 1$, giving $a = 1$, with wind forcing of strengths $Q_w = 0$, 0.1 and 0.5.

causes the expelled fluid to be pushed away from the coast and form an offshore current at an angle to the coast and with a rounded head similar to the observations shown in fig. 5.20. As the wind strength increases the current forms a larger angle to the coast and travels less far alongshore.

5.3 Conclusions

This chapter applies a simple QG model to investigate the dynamics of coastal outflows using contour dynamics simulations and the long wave analytical solutions developed in chapter 4. The chapter has four main parts: first the implications of the long wave solutions are discussed in an oceanographic context. Second, the impacts of ambient currents, tides, winds and variable source flux are examined with extensions of the long wave theory. Third, the momentum fluxes are considered, resolving the momentum imbalance paradox [Pichevin and Nof, 1997] and showing that steady solutions are a robust feature of coastal outflows. Finally, a numerical scheme to compute steady solutions is developed. The simplicity of the model and the accuracy of the long wave approximation mean that the dynamics can be fully understood and used to interpret observations, experiments and more sophisticated and complex numerical models. Despite the simplicity of the model it shows good agreement in comparisons with observations, experiments and other numerical models.

The results are analysed in detail for three primary problems: zero, positive and negative PV, and a full range of the inverse Kelvin number $a = L_R\sqrt{|\Pi|/Q_0}$, which measures the relative importance of the vorticity to the source. For zero PV the outflow profile grows indefinitely with a long rarefying head to the right. For

positive PV, both the source and the vorticity contribute positive x-momentum flux and for all a, steady profiles evolve with a constant width coastal current led by either a rarefying head for low a or a rounded head for larger a. The outflow profile and velocity fields match well to observations of the Chesapeake Bay outflow [Donato and Marmorino, 2002]. For negative PV, which can also be interpreted as a positive PV outflow against an ambient current, richer dynamics are obtained due to the competing effects of the positive x-momentum flux from the source driving the flow rightward and the negative x-momentum flux from the vorticity driving it left, and bidirectional currents form. For $a \leq 1$ the near-source bulge grows indefinitely with rarefactions carrying fractions of the flux leftward and rightward. For $a > 1$ the flow always evolves to a steady profile across the source region, connecting to steady constant width currents both leftward and rightward which are led by a rarefaction on the right and either a rarefaction (for smaller a) or rounded vortical profile (for larger a) on the left.

With a detailed understanding of the dynamics developed in these primary problems, the effects of a number of other factors are then considered. The effects of an ambient alongshore current of strength Q_c are investigated and the long wave theory is expanded to fully characterise the dynamics in $(Q_\mathrm{c}/Q_0, a)$-space with four main dynamical regimes identified: steady rightward currents, steady bi-directional currents, steady leftward currents and unsteady growth. The outflows in each of these regimes are accurately described by analytical long wave solutions. This identifies a number of interesting features. Downstream ambient currents ($Q_\mathrm{c} > 0$) suppress the growth of the bulge and encourage the growth of steady constant width currents containing the entire fluid flux, matching well to the results of Fong and Geyer [2002]. Upstream flowing ambient currents can lead to the formation of bidirectional steady currents as observed, for example, in the ambient current forced Columbia River outflow [Hickey et al., 2005]. The results here support the conclusion of Matano and Palma [2010a] that bidirectional currents are a robust feature of coastal outflows. These are observed in outflows from the Columbia [Hickey et al., 2005], Hudson [Chant, 2011] and Chiangjiang (Yangtze) [Beardsley et al., 1985] rivers and can be forced by ambient currents, winds or the generation of negative vorticity.

Outflows with variable source flux are investigated for two prototypical problems:

for a flux transitioning from one constant value to another, analytical long wave solutions are found and demonstrated; and for a sinusoidally varying source flux, it is shown that, over a complete cycle, the outflow profile does not vary significantly from a constant strength outflow with the same average flux. Analysis of the long wave speed shows that a smooth outflow profile evolves if the long wave speed increases in the direction of propagation. Otherwise, where the wave speed decreases, a shock forms in the long wave solution and is resolved by the full two-dimensional dynamics into large waves.

A second important periodic forcing is that of tides. Here the effects of tides were represented as a sinusoidally varying alongshore current. These were found to have significant effects on the outflow profile, halting the formation of the near-source bulge and spreading the fluid alongshore, matching well to the results of Isobe [2005]. The effects of winds were represented and it was shown that, for upwelling-favourable winds, the outflow fluid detaches from the coastline and forms a rounded profile, matching well to observations from the Chesapeake Bay outflow [Dzwonkowski and Yan, 2005] and observations and numerical simulations of the Columbia River outflow [Hickey et al., 2005].

Chapter 6

Conclusions and future work

This thesis uses simple models of $1\frac{1}{2}$-layer quasigeostrophic flow to examine flows in the coastal ocean driven by vorticity. Two main problems are considered: the generation of eddies as flow separates at a point of sharply varying coastline, expelling the vortical boundary layer into the interior flow; and the evolution of an outflow of fluid from a river or strait which gains relative vorticity as it adjusts. Chapter 2 presents a quasigeostrophic Brown–Michael (QGBM) model which represents shed vorticity as a single point vortex of variable strength. A numerical scheme to find the streamfunction and advect the vortices is developed and tested, and some results describing the evolution of eddies shed from the tips of infinite wedges are discussed. In chapter 3 the QGBM model is applied to a number of oceanographic examples and the results are discussed in comparison to observational, experimental and numerical modelling studies. Chapter 4 presents a simple model of a coastal outflow in which the outflow fluid has constant potential vorticity. Analytical solutions describing much of the evolution, including the ultimate variable-width steady solutions and the unsteady leading heads, are derived using a long-wave approximation. These solutions are compared to contour dynamics results and shown to accurately reproduce the outflow evolution. In chapter 5 the model is further discussed in an oceanographic context with comparisons to observational, experimental and numerical model results. The model is extended to consider the additional effects of variable strength outflow, ambient alongshore currents, tides and winds. A consideration of the momentum fluxes in the model is used to understand the turning of the current and to resolve the momentum imbalance paradox of Pichevin and Nof [1997].

Additionally, a numerical scheme to compute steady solutions is developed. Direct summary and conclusions are presented at the end of each chapter. Some further conclusions and avenues of future work are discussed here.

6.1 Point vortex modelling of sheddies

Recent work [Dewar et al., 2015, Gula et al., 2015, Molemaker et al., 2015] showing that vertical eddy diffusivity causes a horizontal shear layer to form at sloped ocean margins has clarified the mechanism for the formation of sheddies and suggests that small-scale viscous separation is under-represented in ocean models. Models without sufficient resolution, sloping boundaries and viscous boundary conditions fail to capture this thin shear layer, its detachment and subsequent dynamical effects.

Detached shear layers typically roll up into concentrated spirals of vorticity and form, or behave as, large coherent eddies. Chapters 2 and 3 model the formation of these mesoscale eddies and their impact in a number of oceanographic contexts using a simple approach based on the Brown–Michael model of vortex shedding, adapted for quasigeostrophic oceanographic flows. The simple nature of the model means it is straightforward to implement, simple to diagnose and that it highlights the key physical processes. The aim is to show that an inviscid model with explicit representations of the important vortical features can accurately represent observed features of oceanic flows while avoiding many of the difficulties of viscous models associated with the very high resolution required to resolve thin but important boundary layers.

The Brown–Michael model is a simplified model which captures the key features of vortex shedding while avoiding both the far more difficult and complex problem of determining the shape and strength of a vortex sheet, and the computational cost of a viscous model using a grid-based approach. It has been widely used in a variety of situations to capture the qualitative, and in some cases quantitative, effects of flow separation. A number of comparisons by other researchers of the Brown–Michael model with more sophisticated approaches have shown good qualitative agreement, especially considering its far lower computational cost. Here it is applied to examine the effects of flow separation from sharply curving boundary topography in the ocean, complementing existing observational, experimental and more complex numerical

work.

An appealing feature of the original Brown–Michael model and of rigid-lid flow is the wide range of results available analytically. Here, this advantage has been exchanged for a more realistic $1\frac{1}{2}$-layer quasigeostrophic model, necessitating the development of a numerical scheme.

Recent work by Johnson and Southwick [2016] derives analytical solutions for the streamfunction and vortex Hamiltonian for quasigeostrophic vortices in rational-angled wedge domains and gap domains. The results are given as infinite sums which can be truncated to accurately give vortex trajectories and have the potential to be generalised to any simple domain in separable coordinates. These new analytical solutions can be applied to the QGBM model in simple domains (wedges and gaps for example) and speed up the calculations significantly by replacing the spectral method to find the streamfunction. In particular, these analytical solutions give simple formulas for the vortex circulation required to satisfy the Kutta condition. For example, for a stream of strength U around a semi-infinite plate the shed vortex circulation is

$$\Gamma_\mathrm{s} = \frac{U\pi\sqrt{2a}}{K_{\frac{1}{2}}(r_\mathrm{s}/a)\sin(\theta_\mathrm{s}/2)}, \tag{6.1}$$

where the shed vortex strength and position are Γ_s and $(r_\mathrm{s}, \theta_\mathrm{s})$ in polar coordinates. Or, if the background flow is a free vortex of strength Γ_f and position $(r_\mathrm{f}, \theta_\mathrm{f})$, also in the semi-infinite plate domain, the Kutta condition is satisfied by

$$\Gamma_\mathrm{s} = \Gamma_\mathrm{f}\frac{K_{\frac{1}{2}}(r_\mathrm{f}/a)\sin(\theta_\mathrm{f}/2)}{K_{\frac{1}{2}}(r_\mathrm{s}/a)\sin(\theta_\mathrm{s}/2)} \tag{6.2}$$

With these simple forms for Γ_s, $\mathrm{d}\Gamma_\mathrm{s}/\mathrm{d}t$ can be written analytically and the QGBM model can be written as a closed system of ODEs for the vortex positions. These can now be integrated using standard, accurate Runge-Kutta methods instead of the implicit time-stepping scheme. For the domain shapes where this method applies, the QGBM model will have comparable computational cost to rigid-lid Brown–Michael simulations. The results of Johnson and Southwick [2016] are supported by analytical solutions derived in appendix A.5. These are expressed as infinite range integrals for the quasigeostrophic streamfunction around wedges using the Kontorovich-Lebedev

transform [Sneddon, 1972]. These results are for arbitrary angled wedges. It may be possible to use a similar technique to find analytical solutions in other domains such as a gap. For a gap, a transform based on the Mathieu functions would be required.

There are a number of other simple domain shapes of oceanographic interest which the QGBM model can be applied to. Examples include multiple gaps in a wall or circular islands, where separation points (where the flow is required to stagnate) would need to be specified.

It could be possible to develop new Brown–Michael models assuming different flow conditions. Examples could include two active layers or models with continuous stratification. While the QGBM model is primarily intended to qualitatively represent the dynamics of shed eddies, it would be of interest to test how well it compares quantitatively to more complex methods. It could also be possible to implement Brown–Michael vortex shedding in numerical ocean models. This may well be pushing the model too far beyond where it realistically applies but it would be of interest to see how an inviscid model of say, flow past an island, with point vortices included to represent separation compares to a standard ocean model with similar computation time, by benchmarking them against high resolution runs of the ocean model.

The streamfunction, rather than complex potential, based derivation of the QGBM model opens up some avenues for applying the Brown–Michael to other vortex shedding problems. One particularly interesting example is the generation of vortex rings as fluid is expelled from an orifice. This could be modelled as an axisymmetric vortex ring, with dynamics governed by a Brown–Michael type model.

6.2 Quasigeostrophic models of outflows

The simple model of coastal outflows considered here displays rich dynamics which can be described remarkably well by long wave solutions. While the majority of recent studies of coastal outflows use ocean observations or simulations in complex numerical models, a bottom-up theoretical approach may have much to contribute to understanding of outflows, supporting observational and modelling efforts. A theoretical framework explaining what features result from the key physics will aide

interpretation of observations. The approach here establishes a first step in understanding the full dynamics of outflows, showing that a variety of features result from relatively simple physics, and examining how these features evolve and fit together.

Examining the momentum fluxes in the model highlights that rotation and vorticity both contribute to, and can be used to understand, the turning of the current and shows that with the momentum flux at the source included, steady solutions conserve momentum and the momentum imbalance paradox [Pichevin and Nof, 1997] is resolved. This clarification enables progress toward understanding when steady solutions, and when indefinitely growing bulges, form from outflows. The picture suggested by the results here is that indefinitely growing bulges are not ubiquitous, but do form in a number of cases. An almost circular growing bulge forms when the outflow velocity is intense and inertia enters the dynamics at leading order. However without inertia it is still possible for bulges to grow indefinitely for outflows with zero PV or small negative PV ($a \leq 1$) i.e. if the source fluid adjusts to a deeper level as it exits the source mouth or if there is an upstream oriented ambient current. The results here also show that the generation of vorticity is a stabilising effect that inhibits the perpetual growth of bulges and is a significant factor in the common observations of constant width steady currents downstream of the source mouth.

There are a number of effects such as mixing, coastline shape and bathymetry that are not included here. Mixing can be highly complex and is driven by a number of factors. Some of those, such as winds and tides are considered here but some, such as waves, bottom friction and frontal processes require more complex modelling. Coastline shape can strongly influence coastal currents. Klinger [1994] and Sadoux et al. [2000] investigated outflows of buoyant water that form geostrophic coastal currents before encountering a cape. At the cape, the flow was able to separate and form a growing gyre similar to those considered in chapters 2 and 3.

The present model is aimed at surface-advected flows so the influence of bathymetry has not been included, although it is possible to represent some shapes of bottom topography in a QG model. An and McDonald [2004] and An [2004] consider outflows of vortical fluid into the coastal ocean with a shelf parallel to the coast with contour dynamics simulations and find that the shelf helps turn the current rightward. Thus, bathymetric steering may be a third mechanism affecting the turning

of outflows. This could be further investigated in a number of ways. While contour dynamics cannot in general incorporate non-piecewise-constant PV distributions, the long wave limit solutions should be able to include simple bathymetry such as a bottom profile linear in y. The effects of a number of small shelves can be investigated using contour dynamics and may give dynamics qualitatively similar to continuously varying bathymetry.

While mixing is a complex process, its effects could, albeit crudely, be represented in the present model. One possible way would be to add a growing layer of intermediate PV between the expelled and recipient fluid. This could, for example, grow normally to the interface, with growth magnitude a function of the velocity along the interface to represent more intense mixing with higher velocities. Such a model can be implemented with contour dynamics.

It would be of interest to perform detailed direct comparisons between the QG model of coastal outflows and more sophisticated numerical models. This would have two purposes: it would quantitatively test the QG model; but could also assess the key idea of the model here, namely that the stretching of vortex columns is key to the dynamics. Key questions would be how well do the generated vorticities in the numerical model match those assumed here and how close is the PV of the outflow fluid to a constant value? Quantitative tests of the QG model would highlight what features are accurately reproduced by the relatively simple assumptions here, and what require more complex dynamics.

Perhaps the biggest difference between the QG model of outflows and those typically applied in the literature is that, in QG, the depth perturbation is small, whereas in many other models the outflow enters a constant density (or continuously stratified) ocean and forms a current which outcrops to the surface i.e. there is an $\mathcal{O}(1)$ change in depth. A unification of these approaches would be to consider a more general outflow assuming flow governed by the rotating shallow water equations, but then to apply a long wave approximation. With the long wave approximation and the assumption of geostrophy, the offshore interface profile and therefore the streamfunction and velocity profiles can be derived, assuming, for example, constant potential vorticity. These relations can be used in the long wave kinematic boundary condition, in a similar analysis to that here, to deduce the evolution of the outflow. This

model would be able to predict the full dynamics of the outflow, including variable width steady currents and unsteady sections of the flow.

Appendix A

Point vortex trajectories

A.1 $\eta(0, Y) = -\operatorname{erfc}(Y/\sqrt{a})$ for steady flow around a semi-infinite plate

For the case of a semi-infinite plate with background flow with boundary condition on the plate $\eta = -1$, the numerical results indicate that, for $x < 0$, $v(x, 0) = k\mathrm{e}^{x/a}/\sqrt{-ax}$ for some constant k. Integrating this along the negative x-axis and equating to the upstream flux shows that the constant $k = -1/\sqrt{\pi}$. As Fig. A.1 shows, the numerical results for $v(x, 0)$ rapidly converge to $-\mathrm{e}^{x/a}/\sqrt{-a\pi x}$ as N is increased. The streamfunction along the negative x-axis can be found by integrating

$$\eta(x, 0) = \int_{-\infty}^{x} \frac{\partial \eta}{\partial x}(x', 0)\,\mathrm{d}x' = \int_{-\infty}^{x} -\frac{\mathrm{e}^{\frac{x'}{a}}}{\sqrt{-\pi a x'}}\,\mathrm{d}x' = -\operatorname{erfc}\left(\sqrt{\frac{x}{a}}\right). \tag{A.1}$$

Therefore in the mapped plane $\eta(0, Y) = -\operatorname{erfc}(Y/\sqrt{a})$. These results are confirmed by the analytical solutions given in appendix A.5 and by Johnson and Southwick [2016].

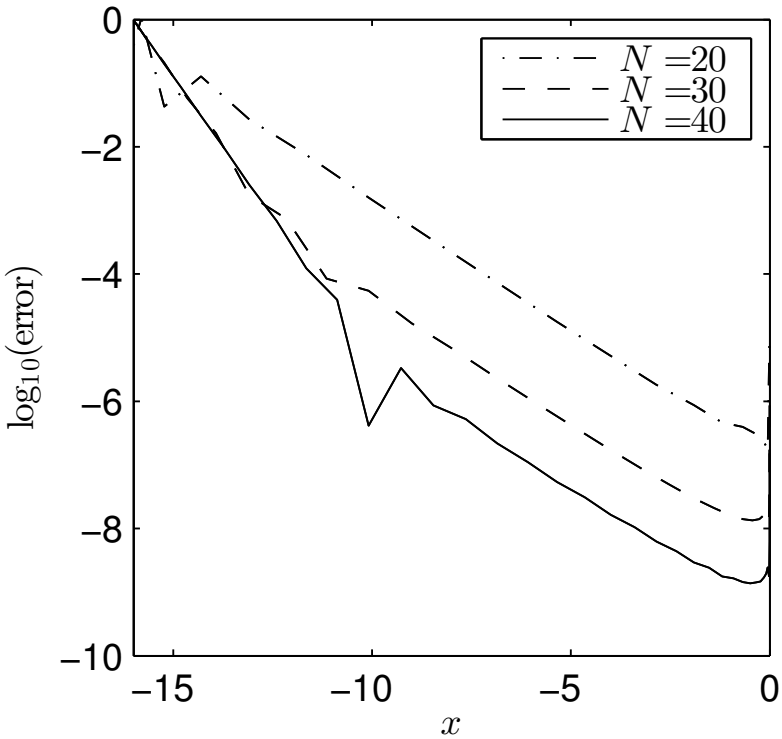

Figure A.1: Log plot of error $= |(-\mathrm{e}^x/\sqrt{-\pi x} - v(x,0))/(-\mathrm{e}^x/\sqrt{-\pi x})|$, the percentage difference between the numerical solution and suggested exact solution for $v(x,0)$ $(x<0)$ for a steady flow around a semi-infinite plate, plotted over x. Results are shown for $a=1$ and three different values of N, the number of grid points in each direction in the spectral grid. The numerical solution appears to be converging to the suggested exact solution with increasing N. The influence of the approximate boundary condition at $x=-16$ is also clear but it should be noted both that the solution is exponentially small for large x (the absolute difference between the numerical and suggested exact solutions is approximately 10^{-8} near $x=-16$ for all three values of N plotted here) and that the solution far from the plate tip has exponentially small influence on the flow near the plate tip.

A.2 Vortex trajectory around a semi-infinite plate for $a \to 0$

In the limit $a \to 0$, a free vortex moving around a semi-infinite plate with no background flow will only 'feel' the effect of the infinitesimal section of boundary closest to it. Therefore the trajectory of the vortex is a straight line, parallel to the wall until the end of the wall is reached and then a semi-circular arc around the tip until it can again move off parallel to the wall. This can be shown asymptotically by reformulating the problem (2.15) and (2.16) as an integral equation using the infinite domain Green's function for (2.15)

$$G(x', y'; x, y) = -\frac{1}{2\pi} K_0 \left(\frac{\sqrt{(x'-x)^2 + (y'-y)^2}}{a} \right). \tag{A.2}$$

Applying Green's theorem, $\widetilde{\eta}$ is given by

$$\widetilde{\eta}(x,y) = \iint_{\mathrm{D}} \widetilde{\eta} \nabla^2 G - G \nabla^2 \widetilde{\eta} \, \mathrm{d}x' \mathrm{d}y' = \underbrace{\int_{\partial \mathrm{D}} \widetilde{\eta} \frac{\partial G}{\partial n} \, \mathrm{d}s}_{\substack{=0 \\ \text{as } \widetilde{\eta} \text{ is continuous} \\ \text{across } \partial \mathrm{D}}} - \int_{\partial \mathrm{D}} G \frac{\partial \widetilde{\eta}}{\partial n} \, \mathrm{d}s, \tag{A.3}$$

where D is the plane with a wall along the positive x-axis. $\widetilde{\eta}$ can now be expressed in terms of an integral along the plate

$$\widetilde{\eta}(x,y) = -\frac{1}{\pi} \int_0^\infty \left. \frac{\partial \widetilde{\eta}}{\partial y'} \right|_{\substack{x'>0 \\ y'=0}} K_0 \left(\frac{\sqrt{(x'-x)^2 + y^2}}{a} \right) \mathrm{d}x', \tag{A.4}$$

in terms of the unknown function $\partial \widetilde{\eta} / \partial y(x, 0)$ (for $x > 0$). From this, expressions for the velocities $\widetilde{u} = -\partial \widetilde{\eta} / \partial y$ and $\widetilde{v} = \partial \widetilde{\eta} / \partial x$ of the vortex are

$$\begin{pmatrix} \widetilde{u}(x_\mathrm{f}, y_\mathrm{f}) \\ \widetilde{v}(x_\mathrm{f}, y_\mathrm{f}) \end{pmatrix} = \frac{1}{\pi a} \int_0^\infty \left. \frac{\partial \widetilde{\eta}}{\partial y'} \right|_{\substack{x'>0 \\ y'=0}} \begin{pmatrix} -y_\mathrm{f} \\ x_\mathrm{f} - x' \end{pmatrix} \frac{1}{\sqrt{(x_\mathrm{f}-x')^2 + y_\mathrm{f}^2}} K_1 \left(\frac{\sqrt{(x'-x_\mathrm{f})^2 + y_\mathrm{f}^2}}{a} \right) \mathrm{d}x'. \tag{A.5}$$

As $a \to 0$, the integral in (A.5) is dominated when the argument of the Bessel function is smallest since the asymptotic form of the Bessel function for large argu-

ment r is

$$K_n(r) \sim \sqrt{\frac{\pi}{2r}}\mathrm{e}^{-r} \text{ for } r \gg 1. \tag{A.6}$$

When $x_\mathrm{f} > 0$, the argument is minimised by $x' = x_\mathrm{f}$. Therefore, $\widetilde{v} \ll \widetilde{u}$ (as the integrand in $\widetilde{v}$ is equal to 0 at $x' = x_\mathrm{f}$) and the vortex moves parallel to the wall. When $x_\mathrm{f} < 0$ the integrals are dominated by the contribution near $x' = 0$. Hence for some small δ, they may be approximated by

$$\begin{pmatrix}\widetilde{u}(x_\mathrm{f}, y_\mathrm{f})\\ \widetilde{v}(x_\mathrm{f}, y_\mathrm{f})\end{pmatrix} \sim \frac{1}{\pi a\sqrt{x_\mathrm{f}^2 + y_\mathrm{f}^2}}\begin{pmatrix}-y_\mathrm{f}\\ x_\mathrm{f}\end{pmatrix}\int_0^\delta \left.\frac{\partial\widetilde{\eta}}{\partial y'}\right|_{\substack{x'>0\\y'=0}} K_1\left(\frac{\sqrt{(x'-x_\mathrm{f})^2 + y_\mathrm{f}^2}}{a}\right)\mathrm{d}x', \tag{A.7}$$

so that

$$(x_\mathrm{f}, y_\mathrm{f})\cdot(\widetilde{u}, \widetilde{v}) = 0, \tag{A.8}$$

and the vortex follows a semi-circular trajectory.

In this limit the movement of the vortex is determined only by the infinitesimally small section of wall closest to it. As the vortex remains a constant distance from this closest section of wall throughout the trajectory its speed must also be constant. This speed is that given by its image in the wall, $|(\widetilde{u}, \widetilde{v})| = (\Gamma/2\pi a)K_1\left(2y_{\mathrm{f}_0}/a\right)$, where y_{f_0} is the initial distance from the wall. These results can equally be derived using a WKB expansion.

A.3 Vortex shedding from a wedge in the rigid-lid limit

In the rigid-lid limit ($a \to \infty$), the ODEs governing the trajectory of a Brown–Michael vortex, shed from the tip of a wedge subject to a flow are found analytically by mapping to the upper half plane and constructing the solution by images. These are then integrated using a standard, high-accuracy Runge–Kutta scheme. The procedure is illustrated in this appendix for the case where the background flow is a single free vortex.

Using the mapping shown in Fig. 2.2, the original rigid-lid Brown–Michael equa-

tion (2.13) becomes

$$\frac{\mathrm{d}Z_\mathrm{s}}{\mathrm{d}t} = c^2|Z_\mathrm{s}|^{-2m} \lim_{Z\to Z_\mathrm{s}} \left(\overline{\frac{\partial \widetilde{W}}{\partial t}}\right) - cZ_\mathrm{s}\frac{\dot{\Gamma}}{\Gamma} \tag{A.9}$$

for the shed vortex position in the mapped plane Z_s, where $\widetilde{W}$ is the complex potential for the flow W with the singular component due to the shed vortex removed i.e.

$$\widetilde{W}(z) = W(z) + \frac{\mathrm{i}\Gamma}{2\pi}\log(Z^{\frac{1}{c}} - Z_\mathrm{s}^{\frac{1}{c}}). \tag{A.10}$$

By the method of images, the complex potential when the background flow is a free vortex at $Z = Z_\mathrm{f}$ is

$$W(Z) = -\frac{\mathrm{i}}{2\pi}\left[\Gamma\log\left(\frac{Z-Z_\mathrm{s}}{Z-\overline{Z_\mathrm{s}}}\right) - \log\left(\frac{Z-Z_\mathrm{f}}{Z-\overline{Z_\mathrm{f}}}\right)\right]. \tag{A.11}$$

Requiring zero velocity at the origin (i.e. $\mathrm{d}W/\mathrm{d}Z|_{Z=0} = 0$) gives the Kutta condition

$$\Gamma = \frac{|Z_\mathrm{s}|^2(Z_\mathrm{f} - \overline{Z_\mathrm{f}})}{|Z_\mathrm{f}|^2(Z_\mathrm{s} - \overline{Z_\mathrm{s}})}. \tag{A.12}$$

Differentiating this and substituting it into (A.9) gives a pair of complex ODEs in terms of the two complex unknowns Z_s and Z_f which, combined with the standard equation for the evolution of the free vortex position, gives a system which is rapidly and accurately integrated with a Runge–Kutta scheme.

A.4 Rigid lid vortex trajectories around a backwards facing step

The existence of a steady state for a Brown–Michael vortex shed from a backward facing step implies the existence of an equilibrium point for constant strength vortices. The trajectories of constant strength vortices can be demonstrated simply using the Kirchoff–Routh path function, a Hamiltonian for the motion of the vortex in the "rigid lid limit" $a \to \infty$ and serve well for illustrative purposes.

In the rigid lid limit $a \to \infty$ the streamfunction satisfies Laplace's equation and

can therefore be found through mapping to the upper half plane and constructing the solution from the method of images. Using this method it is straightforward to find the Kirchoff-Routh path function, which gives the trajectories of free vortices. The path function is found by removing the singular part of the streamfunction due to the vortex, then evaluating at the position of the vortex. This gives a Hamiltonian $H(z_\mathrm{e})$ for the motion of the vortex $z_\mathrm{e} = x_\mathrm{e} + \mathrm{i}y_\mathrm{e}$. If there is a mapping $Z \to z$ from a half plane with coordinates Z to the physical domain with coordinates z then the path function for a point vortex of strength Γ with a background flow of uniform strength U at infinity is given by

$$H(z_\mathrm{e}) = \lim_{z,Z\to z_\mathrm{e},Z_\mathrm{e}} \left(\frac{\mathrm{i}\Gamma}{2\pi} \log\left(\frac{Z - Z_\mathrm{e}}{(z - z_\mathrm{e})(Z - \overline{Z}_\mathrm{e})} \right) + UZ \right). \tag{A.13}$$

A mapping from the lower half plane to the backwards facing step domain is given by

$$z = \frac{1}{\pi}\left(2\log\left(\sqrt{Z-1} + \sqrt{Z+1} \right) - \log 2 - \sqrt{Z^2 - 1} \right). \tag{A.14}$$

Using this in (A.13) gives the vortex Hamiltonian

$$H(Z_\mathrm{e}) = \frac{\mathrm{i}\Gamma}{2\pi} \log\left(\sqrt{\frac{\overline{Z_\mathrm{e} - 1}}{Z_\mathrm{e} + 1}} \frac{\pi}{Z_\mathrm{e} - \overline{Z}_\mathrm{e}} \right) + UZ_\mathrm{e}, \tag{A.15}$$

which has been left in terms of Z_e instead of z_e here for simplicity. This has one degree of freedom in the ratio Γ/U.

An example showing the trajectories of vortices of strength $\Gamma = 5$ and with a steady current of strength $U = 1$ for a range of initial positions are shown in figure A.2. This shows a neutrally stable fixed point (a centre) near the origin and a saddle point near $\boldsymbol{x}_\mathrm{e} \approx (0.8, -0.3)$. There is a further neutrally stable fixed point at infinity. It appears that the effect of the Kutta condition and Brown–Michael correction is to destabilise the stable fixed points and stabilise the saddle point, as well as modifying their positions.

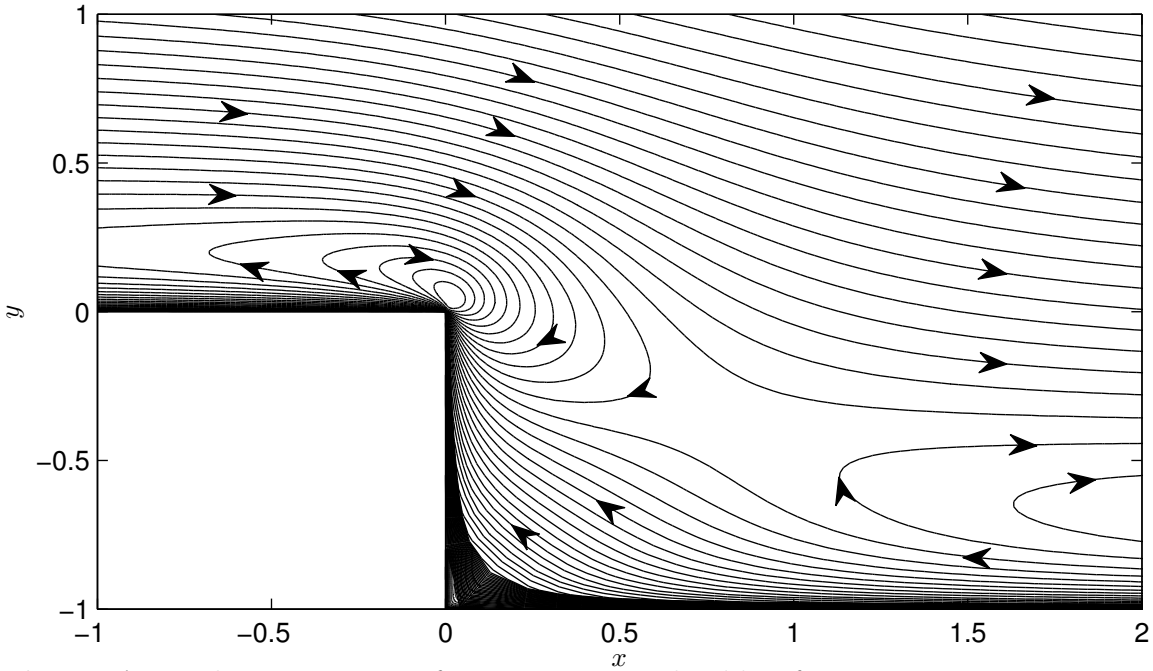

Figure A.2: The trajectories of constant strength eddies for various starting points in the rigid-lid limit $a \to \infty$ for current strength $U = 1$ and vortex circulation $\Gamma = 5$.

A.5 Analytical solutions for QG flow around a semi-infinite plate

In this appendix the Kontorovich-Lebedev transform is used to obtain analytical solutions for the QG streamfunction for flows consisting of either a point vortex or a uniform flow around either a semi-infinite plate or arbitrary angled wedge. In each case the streamfunction is given as an integral.

The streamfunction for QG flow around a semi-infinite plate for arbitrary boundary condition is given in A.5, then applied to a uniform flow in A.5, where the expression for the streamfunction can be simplified, confirming the observed solution along the line $\theta = \pi$. In A.5 the streamfunction for a point vortex around a semi-infinite plate is given and in A.5 solutions are given for a steady current or point vortex in a wedge domain.

A.5.1 The Kontorovich-Lebedev transform

The Kontorovich-Lebedev transform (see e.g. Sneddon [1972]) of a function $f(x)$

is given by

$$\mathcal{K}[f(x);\tau] = \widetilde{f}(\tau) = \int_0^\infty f(x)\frac{K_{\mathrm{i}\tau}(x)}{x}\,\mathrm{d}x, \tag{A.16}$$

where $K_{\mathrm{i}\tau}(x)$ is the MacDonald function, the modified Bessel function of the second kind of imaginary order. A useful formula for this is

$$K_{\mathrm{i}\tau}(x) = \int_0^\infty \mathrm{e}^{-x\cosh(s)}\cos(\tau s)\,\mathrm{d}s. \tag{A.17}$$

The inverse of the Kontorovich-Lebedev transform is given by

$$f(x) = \mathcal{K}^{-1}[\widetilde{f}(\tau)] = \frac{2}{\pi^2}\int_0^\infty \widetilde{f}(\tau)\tau\sinh(\pi\tau)K_{\mathrm{i}\tau}(x)\,\mathrm{d}\tau. \tag{A.18}$$

A.5.2 Quasigeostrophic flow around a semi-infinite plate

Consider the problem of quasigeostrophic flow around a semi-infinite plate satisfying

$$\nabla^2\eta - \frac{1}{a^2}\eta = 0, \tag{A.19a}$$

$$\eta(r,0) = \eta(r,2\pi) = f(r), \tag{A.19b}$$

$$\eta \to 0, \qquad \text{as } r \to \infty, \tag{A.19c}$$

where $f(r)$ is some known boundary condition. Examples of interest are $f(r) = -1$ for a uniform stream and $f(r) = \Gamma/2\pi K_0(|\boldsymbol{x} - \boldsymbol{x}_\mathrm{e}|/a)$ for a point vortex of strength Γ at position $\boldsymbol{x}_\mathrm{e}$.

Looking for separable solutions to this problem of the form

$$\eta(r,\theta) = \psi(r)\mathrm{e}^{\pm\tau\theta}, \tag{A.20}$$

gives the equation

$$\frac{\partial^2\eta}{\partial r^2}+\frac{1}{r}\frac{\partial\eta}{\partial r}+\left(\frac{\tau^2}{r^2}-\frac{1}{a^2}\right)\eta=0. \tag{A.21}$$

One solution of this is $\psi = K_{\mathrm{i}\tau}(r/a)$ giving

$$\eta(r,\theta)=K_{\mathrm{i}\tau}(r/a)\mathrm{e}^{\pm\tau\theta}. \tag{A.22}$$

A more general solution can be obtained through linear superposition i.e.

$$\eta(r,\theta)=\int_0^\infty A_\pm(\tau)K_{\mathrm{i}\tau}\left(\frac{r}{a}\right)\mathrm{e}^{\pm\tau\theta}\,\mathrm{d}\tau, \tag{A.23}$$

for arbitrary functions $A_\pm(\tau)$. For certain choices of $A_\pm(\tau)$ this gives the inversion of the Kontorovich-Lebedev transform. A particular choice of $A_\pm(\tau)$ is used to satisfy the boundary conditions on the problem in the following section.

A.5.3 Solution satisfying the boundary conditions

A solution of (A.19a), satisfying the boundary condition (A.19b) in the form of (A.23) is

$$\begin{aligned}\eta(r,\theta)&=\mathcal{K}^{-1}\left[\frac{\cosh\tau(\theta-\pi)}{\cosh\tau\pi}F(\tau);\tau\to\frac{r}{a}\right]\\&=\frac{2}{\pi^2}\int_0^\infty\frac{\cosh\tau(\theta-\pi)}{\cosh\tau\pi}F(\tau)\tau\sinh(\pi\tau)K_{\mathrm{i}\tau}\left(\frac{r}{a}\right)\,\mathrm{d}\tau,\end{aligned} \tag{A.24}$$

where the function of $F(\tau)$ is the Kontorovich-Lebedev transform of the boundary condition $f(r)$ i.e.

$$\begin{aligned}F(\tau)&=\mathcal{K}\left[f(r);\frac{r}{a}\to\tau\right]\\&=\int_0^\infty f(as)\frac{K_{\mathrm{i}\tau}(s)}{s}\mathrm{d}s.\end{aligned} \tag{A.25}$$

A.5.4 Solution for a uniform flow

For a uniform flow $f(r/a) = -1$ so $F(\tau)$ is given by

$$F(\tau)=\mathcal{K}[-1]=\frac{-\pi}{2\tau\sinh(\pi\tau/2)}. \tag{A.26}$$

Using this in (A.24) gives the solution

$$\begin{aligned}\eta(r,\theta) &= \mathcal{K}^{-1}\left[\frac{\cosh\tau(\theta-\pi)}{\cosh\tau\pi}\frac{-\pi}{2\tau\sinh(\pi\tau/2)};\tau\to\frac{r}{a}\right]\\ &= \frac{-2}{\pi}\int_0^\infty \frac{\cosh\tau(\theta-\pi)}{\cosh\tau\pi}\cosh\left(\frac{\pi\tau}{2}\right)K_{\mathrm{i}\tau}\left(\frac{r}{a}\right)\,\mathrm{d}\tau. \end{aligned} \tag{A.27}$$

Substituting for $K_{\mathrm{i}\tau}(r/a)$ using (A.17) gives

$$\eta(r,\theta) = \frac{-2}{\pi}\int_0^\infty \frac{\cosh\tau(\theta-\pi)}{\cosh\tau\pi}\cosh\left(\frac{\pi\tau}{2}\right)\int_0^\infty \mathrm{e}^{-\frac{r}{a}\cosh(s)}\cos(\tau s)\,\mathrm{d}s\,\mathrm{d}\tau \tag{A.28}$$

$$= \frac{-2}{\pi}\int_0^\infty \mathrm{e}^{-\frac{r}{a}\cosh(s)}\int_0^\infty \frac{\cosh\tau(\theta-\pi)}{\cosh\tau\pi}\cosh\left(\frac{\pi\tau}{2}\right)\cos(\tau s)\,\mathrm{d}\tau\,\mathrm{d}s. \tag{A.29}$$

Where this exchange of the order of integration is only valid for $\pi/2 < \theta < 3\pi/2$. For θ outside of this range the integral with respect to τ in (A.29) does not converge.

A check on the solution

A check on this solution is to compare it to the observed solution for $\theta = \pi$ which is $\eta(x,0) = -\mathrm{erfc}(\sqrt{|x|/a})$ for $x < 0$. This gives the velocity $v(x,0) = -\mathrm{e}^{x/a}/\sqrt{\pi a|x|}$, again for $x < 0$.

Using $\theta = \pi$ in (A.29) gives

$$\eta(r,\pi) = \frac{-2}{\pi}\int_0^\infty \mathrm{e}^{-\frac{r}{a}\cosh(s)}\int_0^\infty \frac{\cosh\left(\frac{\pi\tau}{2}\right)}{\cosh(\pi\tau)}\cos(\tau s)\,\mathrm{d}\tau\,\mathrm{d}s. \tag{A.30}$$

The integral with respect to τ is a Fourier cosine transform[1] and is given by

$$\int_0^\infty \frac{\cosh\left(\frac{\pi\tau}{2}\right)}{\cosh(\pi\tau)}\cos(\tau s)\,\mathrm{d}\tau = \sqrt{\frac{\pi}{2}}\mathcal{F}_c\left[\frac{\cosh\left(\frac{\pi\tau}{2}\right)}{\cosh(\pi\tau)}\right] \tag{A.31}$$

$$= \sqrt{\frac{\pi}{2}}\frac{\sqrt{2\pi}}{\pi}\frac{\frac{1}{\sqrt{2}}\cosh\left(\frac{s}{2}\right)}{\cosh s + 0} \tag{A.32}$$

$$= \frac{1}{\sqrt{2}}\frac{\cosh\left(\frac{s}{2}\right)}{\cosh(s)}. \tag{A.33}$$

[1] The Fourier cosine transform of $f(x)$ is defined as $\mathcal{F}_c[f(x),k] = \sqrt{2/\pi}\int_0^\infty f(x)\cos(kx)\mathrm{d}x$. The inverse is achieved by taking the Fourier cosine transform again.

Where (A.32) is achieved using the known formula

$$\mathcal{F}_c\left[\frac{\cosh(\alpha\tau)}{\cosh(\beta\tau)};s\right]=\frac{\sqrt{2\pi}}{\beta}\frac{\cos\left(\frac{\pi\alpha}{2\beta}\right)\cosh\left(\frac{\pi s}{2\beta}\right)}{\cosh\left(\frac{\pi s}{\beta}\right)+\cos\left(\frac{\pi\alpha}{\beta}\right)}, \tag{A.34}$$

valid for $0<\alpha<\beta$.

Now, using (A.33) in (A.30) gives

$$\eta(r,\pi)=\frac{-\sqrt{2}}{\pi}\int_0^\infty \mathrm{e}^{-\frac{r}{a}\cosh(s)}\frac{\cosh\left(\frac{s}{2}\right)}{\cosh(s)}\,\mathrm{d}s. \tag{A.35}$$

Differentiating with respect to r gives

$$\frac{\partial\eta(r,\pi)}{\partial r}=\frac{\sqrt{2}}{\pi a}\int_0^\infty \mathrm{e}^{-\frac{r}{a}\cosh(s)}\cosh\left(\frac{s}{2}\right)\mathrm{d}s \tag{A.36}$$

$$=\frac{\sqrt{2}}{\pi a}\sqrt{\frac{\pi}{2}}\frac{\mathrm{e}^{-\frac{r}{a}}}{\sqrt{\frac{r}{a}}} \tag{A.37}$$

$$=\frac{\mathrm{e}^{-\frac{r}{a}}}{\sqrt{\pi a r}}. \tag{A.38}$$

which matches with the observed solution $v(x,0)=-\mathrm{e}^{x/a}/\sqrt{\pi a|x|}$ for $x<0$. The difference in sign is because $v_\theta=\partial\eta/\partial r$ points in the negative y direction when $\theta=\pi$.

A simplification of the solution for $\frac{\pi}{2}<\theta<\frac{3\pi}{2}$

For $\pi/2<\theta<3\pi/2$ the exchange of order of integration in (A.29) is valid and the Fourier cosine transform term converges and can be evaluated as

$$\int_0^\infty \frac{\cosh\tau(\theta-\pi)}{\cosh\tau\pi}\cosh\left(\frac{\pi\tau}{2}\right)\cos(\tau s)\,\mathrm{d}\tau=\frac{\sqrt{2}\cosh\left(\frac{s}{2}\right)\Big(\cosh s-1-\cos\theta\Big)\sin\frac{\theta}{2}}{\cosh 2s+\cos 2\theta}. \tag{A.39}$$

Setting $\theta=\pi$ reproduces (A.33). Using (A.39) in (A.29) gives

$$\eta(r,\theta)=\frac{-2\sqrt{2}}{\pi}\sin\left(\frac{\theta}{2}\right)\int_0^\infty \mathrm{e}^{-\frac{r}{a}\cosh(s)}\frac{\cosh\left(\frac{s}{2}\right)\Big(\cosh s-1-\cos\theta\Big)}{\cosh 2s+\cos 2\theta}\,\mathrm{d}s. \tag{A.40}$$

This integral cannot easily be performed. However, for the limit $a \to 0$ it can be approximated using Laplace's method[2] to give

$$\begin{aligned}\eta(r,\theta) &\sim 2\sqrt{\frac{a}{\pi r}}\frac{\cos\theta \sin\frac{\theta}{2}}{1+\cos 2\theta}\mathrm{e}^{-\frac{r}{a}} \\ &= \sqrt{\frac{a}{\pi r}}\frac{\sin\frac{\theta}{2}}{\cos\theta}\mathrm{e}^{-\frac{r}{a}}. \end{aligned} \tag{A.41}$$

This approximation breaks down for θ close to either $\pi/2$ or $3\pi/2$ but is valid around $\theta = \pi$. The same asymptotic formula can be achieved for $\pi/2 < \theta < 3\pi/2$ directly from (A.27). For this range of θ the integral decays exponentially with τ so the expansion $K_{\mathrm{i}\tau}(x) \sim \sqrt{\pi/2x}\exp(-x)$, valid for $x \gg 1, \tau$, can be used to give

$$\eta(r,\theta) \sim -\sqrt{\frac{2a}{\pi r}}\mathrm{e}^{-\frac{r}{a}}\int_0^\infty \frac{\cosh\tau(\theta-\pi)}{\cosh\tau\pi}\cosh\left(\frac{\pi\tau}{2}\right)\mathrm{d}\tau \tag{A.42}$$

$$= \sqrt{\frac{a}{\pi r}}\mathrm{e}^{-\frac{r}{a}}\frac{\sin\frac{\theta}{2}}{\cos\theta}. \tag{A.43}$$

A.5.5 Solution for a point vortex

For the case of a point vortex of strength Γ as position $\boldsymbol{x}_\mathrm{e} = (x_\mathrm{e}, y_\mathrm{e})$, $f(r) = (\Gamma/2\pi)K_0(\sqrt{(r-x_\mathrm{e})^2+y_\mathrm{e}^2}/a)$ so $F(\tau)$ is given by

$$F(\tau) = \mathcal{K}\left[\frac{\Gamma}{2\pi}K_0\left(\frac{\sqrt{(r-x_\mathrm{e})^2+y_\mathrm{e}^2}}{a}\right)\right] \tag{A.44}$$

$$= \frac{\Gamma}{2\pi}\int_0^\infty K_0\left(\sqrt{(s-\widetilde{x}_v)^2+\widetilde{y}_v^2}\right)\frac{K_{\mathrm{i}\tau}(s)}{s}\,\mathrm{d}s, \tag{A.45}$$

where $(\widetilde{x}_v, \widetilde{y}_v) = (x_\mathrm{e}, y_\mathrm{e})/a$. This gives the streamfunction

$$\eta(r,\theta) = \frac{\Gamma}{\pi^3}\int_0^\infty \frac{\cosh\tau(\theta-\pi)}{\cosh\tau\pi}\tau\sinh(\pi\tau)K_{\mathrm{i}\tau}\left(\frac{r}{a}\right)\int_0^\infty K_0\left(\sqrt{(s-\widetilde{x}_v)^2+\widetilde{y}_v^2}\right)\frac{K_{\mathrm{i}\tau}(s)}{s}\,\mathrm{d}s\,\mathrm{d}\tau. \tag{A.46}$$

[2]Consider the integral $I = \int_a^b f(t)\exp(\lambda\phi(t))\,\mathrm{d}t$ in the limit $\lambda \to \infty$. The dominant contribution to the integral comes from where $\phi(t)$ is largest. If this is at $t = a$, but $\phi'(a) = 0$ and $\phi''(a) < 0$ as is the case here then at leading order the integral may be approximated by $I \sim f(a)\exp(\lambda\phi(a))\sqrt{\pi/(-2\lambda\phi''(a))}$.

If the order of integration can legitimately be exchanged then doing so gives

$$\eta(r,\theta) = \frac{\Gamma}{\pi^3}\int_0^\infty \frac{1}{s} K_0\left(\sqrt{(s-\widetilde{x}_v)^2+\widetilde{y}_v^2}\right)\int_0^\infty \tau\cosh\left(\tau(\theta-\pi)\right)\tanh(\pi\tau)K_{\mathrm{i}\tau}\left(\frac{r}{a}\right)K_{\mathrm{i}\tau}(s)\,\mathrm{d}\tau\,\mathrm{d}s. \tag{A.47}$$

Neither of the above integrals can be easily evaluated analytically.

A.5.6 Solution outside a wedge

Consider quasigeostrophic flow outside the infinite wedge $0 < \theta < 2\pi - \alpha$ (for arbitrary wedge angle $0 \le \alpha < 2\pi$) satisfying (using $\gamma = 2\pi - \alpha$)

$$\nabla^2\eta - \frac{1}{a^2}\eta = 0, \tag{A.48a}$$

$$\eta(r,0) = f_1(r), \tag{A.48b}$$

$$\eta(r,\gamma) = f_2(r), \tag{A.48c}$$

$$\eta \to 0, \qquad \text{as } r \to \infty. \tag{A.48d}$$

The solution of this problem is given by

$$\eta(r,\theta) = \mathcal{K}^{-1}\left[\frac{\sinh\tau(\gamma-\theta)}{\sinh\tau\gamma}F_1(\tau) + \frac{\sinh\tau\theta}{\sinh\tau\gamma}F_2(\tau); \tau\to\frac{r}{a}\right] \tag{A.49}$$

$$= \frac{2}{\pi^2}\int_0^\infty\left(\frac{\sinh\tau(\gamma-\theta)}{\sinh\tau\gamma}F_1(\tau) + \frac{\sinh\tau\theta}{\sinh\tau\gamma}F_2(\tau)\right)\tau\sinh(\pi\tau)K_{\mathrm{i}\tau}\left(\frac{r}{a}\right)\,\mathrm{d}\tau, \tag{A.50}$$

where the functions $F_1(\tau)$ and $F_2(\tau)$ are the Kontorovich-Lebedev transforms of the boundary conditions $f_1(r)$ and $f_2(r)$ respectively i.e.

$$F_1(\tau) = \mathcal{K}\left[f_1(r); \frac{r}{a}\to\tau\right] \tag{A.51}$$

$$= \int_0^\infty f_1(as)\frac{K_{\mathrm{i}\tau}(s)}{s}\mathrm{d}s \tag{A.52}$$

and

$$F_2(\tau) = \mathcal{K}\left[f_2(r); \frac{r}{a} \to \tau\right] \tag{A.53}$$

$$= \int_0^\infty f_2(as)\frac{K_{\mathrm{i}\tau}(s)}{s}\mathrm{d}s. \tag{A.54}$$

Uniform flow around a wedge

For a steady flow of unit flux around a wedge $f_1(r) = f_2(r) = -1$, giving $F_1(\tau) = F_2(\tau) = -\pi/(2\tau\sinh(\pi\tau/2))$. Using this in (A.50) gives

$$\eta(r,\theta) = \frac{-2}{\pi}\int_0^\infty \left(\frac{\sinh\tau(\gamma-\theta)}{\sinh\tau\gamma} + \frac{\sinh\tau\theta}{\sinh\tau\gamma}\right)\cosh\left(\frac{\pi\tau}{2}\right)K_{\mathrm{i}\tau}\left(\frac{r}{a}\right)\,\mathrm{d}\tau. \tag{A.55}$$

When $\gamma = 2\pi$, with some rearranging, this reproduces (A.29).

Point vortex outside a wedge

For a point vortex of strength Γ at position $\boldsymbol{x}_\mathrm{e}$ the boundary conditions are

$$f_1(r) = \frac{\Gamma}{2\pi}K_0\left(\frac{\sqrt{(r-x_\mathrm{e})^2+y_\mathrm{e}^2}}{a}\right), \tag{A.56a}$$

$$f_2(r) = \frac{\Gamma}{2\pi}K_0\left(\frac{\sqrt{(r\cos\gamma-x_\mathrm{e})^2+(r\sin\gamma-y_\mathrm{e})^2}}{a}\right). \tag{A.56b}$$

This gives the Kontorovich-Lebedev transforms

$$F_1(\tau) = \frac{\Gamma}{2\pi}\int_0^\infty K_0\left(\sqrt{(s-\widetilde{x}_v)^2+\widetilde{y}_v^2}\right)\frac{K_{\mathrm{i}\tau}(s)}{s}\mathrm{d}s, \tag{A.57a}$$

$$F_2(\tau) = \frac{\Gamma}{2\pi}\int_0^\infty K_0\left(\sqrt{(r\cos\gamma-x_\mathrm{e})^2+(r\sin\gamma-y_\mathrm{e})^2}\right)\frac{K_{\mathrm{i}\tau}(s)}{s}\mathrm{d}s. \tag{A.57b}$$

Using these in (A.50) gives

$$\eta(r,\theta) = \frac{2}{\pi^2}\int_0^\infty \left(\frac{\sinh\tau(\gamma-\theta)}{\sinh\tau\gamma}F_1(\tau) + \frac{\sinh\tau\theta}{\sinh\tau\gamma}F_2(\tau)\right)\tau\sinh(\pi\tau)K_{\mathrm{i}\tau}\left(\frac{r}{a}\right)\,\mathrm{d}\tau. \tag{A.58}$$

Appendix B

Outflows of vortical fluid

B.1 Integrated momentum balance for QG flow

The non-dimensional rotating shallow water equations are

$$\varepsilon\frac{\mathrm{D}\eta}{\mathrm{D}t} + (a^2 + \varepsilon\eta)\boldsymbol{\nabla}\cdot\boldsymbol{u} = 0, \tag{B.1a}$$

$$\varepsilon\frac{\mathrm{D}\boldsymbol{u}}{\mathrm{D}t} + \boldsymbol{k}\wedge\boldsymbol{u} = -\boldsymbol{\nabla}\eta, \tag{B.1b}$$

where ε is the Rossby number and $a = L_\mathrm{R}/\widehat{L}$, for the lengthscale $\widehat{L}$.

Quasigeostrophic flow is obtained when $\varepsilon \ll 1$ by taking an asymptotic expansion of the form $\eta = \eta_0 + \epsilon\eta_1 + \cdots$, $\boldsymbol{u} = \boldsymbol{u}_0 + \varepsilon\boldsymbol{u}_1 + \cdots$ giving, at leading order,

$$\boldsymbol{u}_0 = -\boldsymbol{\nabla}\wedge(\eta_0\boldsymbol{k}), \tag{B.2}$$

and at $\mathcal{O}(\varepsilon)$

$$\frac{1}{a^2}\frac{\mathrm{D}_0\eta_0}{\mathrm{D}_0 t} + \boldsymbol{\nabla}\cdot\boldsymbol{u}_1 = 0, \tag{B.3a}$$

$$\frac{\mathrm{D}_0\boldsymbol{u_0}}{\mathrm{D}_0 t} + \boldsymbol{k}\wedge\boldsymbol{u}_1 = -\boldsymbol{\nabla}\eta_1, \tag{B.3b}$$

where $\mathrm{D}_0/\mathrm{D}_0 t = \partial/\partial t + (\boldsymbol{u}_0\cdot\boldsymbol{\nabla})$. Thus the leading order flow is geostrophic. The governing equation (conservation of PV) for η_0 (1.2) is found from (B.3). (B.2)

shows that QG flow satisfies the momentum equation (B.1b) to leading order trivially. However, the next order balance in the momentum equation, given by (B.3b) can also impose a condition on the leading order flow.

Consider a steady outflow profile. Using the steadiness of the flow and the leading order geostrophy, (B.3a) implies that there exists a streamfunction ψ_1 for the $\mathcal{O}(\varepsilon)$ flow, so $\boldsymbol{u}_1 = -\nabla \wedge (\psi_1 \boldsymbol{k})$. Integrating the x-component of the momentum equation (B.3b) over a control volume S with boundary ∂S for steady flow gives

$$0 = \iint_S u_0 \frac{\partial u_0}{\partial x} + v_0 \frac{\partial u_0}{\partial y} - v_1 + \frac{\partial \eta_1}{\partial x} \,\mathbf{d}\boldsymbol{x}, \tag{B.4}$$

$$= \iint_S \frac{\partial u_0^2}{\partial x} + \frac{\partial u_0 v_0}{\partial y} - \frac{\partial \psi_1}{\partial x} + \frac{\partial \eta_1}{\partial x} \,\mathbf{d}\boldsymbol{x}, \tag{B.5}$$

$$= \oint_{\partial S} -u_0 v_0 \,\mathrm{d}x + \oint_{\partial S} u_0^2 - \psi_1 + \eta_1 \,\mathrm{d}y, \tag{B.6}$$

where the continuity equation has been applied in the second line and Stokes' theorem has been applied in the third. The control volume can either be taken to be a large rectangle $-R < x < R$, $0 < y < H$ or the shape bounded by the outer streamline of the outflow, $-R < x < R$, $0 < y < Y$ for large R. Either way, the only boundaries contributing to the momentum fluxes are at the source and the upstream and downstream sections at $x = \pm R$ if ψ_1 is taken to be zero at the current edge. Where the current exits the domain it has a constant width and is independent of x. Therefore, (B.3b) implies that $\partial \psi_1(\pm R, y)/\partial y = \partial \eta_1(\pm R, y)/\partial y$ and it follows that $\psi_1(\pm R, y) = \eta_1(\pm R, y)$ as both η_1 and ψ_1 are 0 at the current edge. Note that η_1 and ψ_1 are not equal throughout the flow, only in the downstream sections (due to the x-independence). Using this in (B.6) gives the integrated x-momentum equation for the leading order QG flow

$$\int_{\partial S} u_0 v_0 \,\mathrm{d}x = \int_{\partial S} u_0^2 \,\mathrm{d}y, \tag{B.7}$$

which is unchanged when redimensionalised. Redimensionalising, noting that the integrals along streamlines contribute nothing and dropping the subscripts gives

$$\int_{-L}^{L} u(x,0)v(x,0) \,\mathrm{d}x = \int_0^Y u(R,y)^2 - u(-R,y)^2 \,\mathrm{d}y. \tag{B.8}$$

A steady quasigeostrophic flow which is x-independent downstream must satisfy this condition.

B.2 Flow field due to the source

B.2.1 General source profile

The quasigeostrophic streamfunction η for the flow due to the source (with zero PV) satisfies the problem $\mathcal{L}\eta = \nabla^2\eta - \eta/a^2 = 0$ with boundary conditions $\eta(x,0) = Q(x)$ and $\nabla\eta \to 0$ as $y \to \infty$. Taking the Fourier transform (with transform variable k) in x of $\mathcal{L}\eta = 0$ gives

$$\widehat{\eta}_{yy} - \left(k^2 + \frac{1}{L_{\mathrm{R}}^2}\right)\widehat{\eta} = 0, \tag{B.9}$$

which has solution satisfying the boundary conditions

$$\widehat{\eta}(k,y) = \widehat{Q}(k)\mathrm{e}^{-\kappa y}, \tag{B.10}$$

where $\kappa = \sqrt{k^2 + L_{\mathrm{R}}^{-2}}$. Taking the inverse Fourier transform gives the streamfunction

$$\eta(x,y) = \frac{1}{2\pi}\int_{-\infty}^{\infty}\widehat{Q}(k)\mathrm{e}^{-\kappa y}\mathrm{e}^{\mathrm{i}kx}\,\mathrm{d}k, \tag{B.11}$$

and using $\boldsymbol{u} = -\nabla\wedge(\eta\boldsymbol{k})$ gives the velocities

$$\begin{pmatrix} u(x,y) \\ v(x,y) \end{pmatrix} = \frac{1}{2\pi}\int_{-\infty}^{\infty}\begin{pmatrix} \kappa \\ \mathrm{i}k \end{pmatrix}\widehat{Q}(k)\mathrm{e}^{-\kappa y}\mathrm{e}^{\mathrm{i}kx}\,\mathrm{d}k. \tag{B.12}$$

These integrals can be truncated and integrated numerically to give the velocity at any point.

For sources with outflow velocity $v(x,0)$ symmetric in x, $Q(x) = Q_{\mathrm{o}}(x) + Q_0/2$, where $Q_{\mathrm{o}}(x)$ is an odd function and the velocities simplify to

$$\begin{pmatrix} u(x,y) \\ v(x,y) \end{pmatrix} = \frac{Q_0}{2L_{\mathrm{R}}}\begin{pmatrix} \mathrm{e}^{-\frac{y}{L_{\mathrm{R}}}} \\ 0 \end{pmatrix} + \frac{\mathrm{i}}{\pi}\int_0^{\infty}\widehat{Q}_{\mathrm{o}}(k)\mathrm{e}^{-\kappa y}\begin{pmatrix} \kappa\sin(kx) \\ k\cos(kx) \end{pmatrix}\mathrm{d}k \tag{B.13}$$

showing that v is even in x and u is an odd in x function plus a constant in x function.

B.2.2 Point source

For a point source outflow a shortcut to a neat form of the solution can be obtained by exploiting linearity of $\mathcal{L}$ and rewriting the problem for $v = \partial\eta/\partial x$ instead of η, giving $\mathcal{L}v = 0$ with boundary conditions $v = Q_0\delta(x)$ for $y = 0$ and $v \to 0$ as $y \to \infty$. Looking for a solution as an eigenfunction expansion in polar coordinates r and θ (i.e. a modified Bessel and trigonometric function expansion), the solution is symmetric in θ about $\theta = \pi/2$ and must satisfy $v = 0$ on $\theta = 0$ and $\theta = \pi$. These conditions are satisfied by the $\sin(\theta)$ term so picking the coefficient to give the right strength singularity gives the solution

$$v = \frac{Q_0}{\pi L_\mathrm{R}} K_1\left(\frac{r}{L_\mathrm{R}}\right)\sin\theta, \tag{B.14}$$

where K_n is the modified Bessel function of the second kind of order n. Integrating gives the streamfunction

$$\eta(x,y) = \frac{Q_0}{2}\mathrm{e}^{-\frac{y}{L_\mathrm{R}}} + \frac{Q_0 y}{\pi L_\mathrm{R}}\int_0^x \frac{K_1\left(\sqrt{x'^2+y^2}/L_\mathrm{R}\right)}{\sqrt{x'^2+y^2}}\,\mathrm{d}x', \tag{B.15}$$

splitting η into even (1^{st} term) and odd (2^{nd} term) parts. After some algebra, $u(x,y) = -\partial\eta/\partial y$ is given by

$$u(x,y) = \frac{Q_0}{L_\mathrm{R}}\left(\frac{\mathrm{e}^{-\frac{y}{L_\mathrm{R}}}}{2} + \frac{xK_1\left(\frac{r}{L_\mathrm{R}}\right)}{\pi r} + \frac{1}{\pi L_\mathrm{R}}\int_0^x K_0\left(\frac{\sqrt{x'^2+y^2}}{L_\mathrm{R}}\right)\mathrm{d}x'\right). \tag{B.16}$$

B.3 Momentum fluxes for long wave solutions

This appendix computes the momentum fluxes through the control domain $x_1 < x < x_2$, $0 < y < Y(x)$ for the steady analytical solutions in the long wave limit for arbitrary L_R, Π, x_1, x_2 and source profile $Q(x)$.

B.3.1 Source momentum flux

The horizontal momentum flux entering the domain from the source between two points x_1 and x_2 is given by

$$\begin{aligned}\Delta M_\mathrm{s} &= \int_{x_1}^{x_2} u(x,0)v(x,0)\,\mathrm{d}x \\ &= \int_{Q_1}^{Q_2} u(x(Q),0)\,\mathrm{d}Q,\end{aligned} \tag{B.17}$$

since $v(x,0) = \partial Q/\partial x$, where $Q_2 = Q(x_2)$ and $Q_1 = Q(x_1)$. The horizontal velocity at $y = 0$ as a function of Q, given by differentiating (4.10) and substituting Y from (4.12), is

$$u(Q) = L_\mathrm{R}\Pi\sqrt{\left(1+\frac{Q}{L_\mathrm{R}^2\Pi}\right)^2 - \left(1+\frac{2Q_\mathrm{e}}{L_\mathrm{R}^2\Pi}\right)}, \tag{B.18}$$

where Q_e is the constant value of the streamfunction on the current edge $Y(x)$. Substituting (B.18) into (B.17) gives the momentum flux from source

$$\Delta M_\mathrm{s} = \frac{L_\mathrm{R}^3\Pi^2}{2}\Big[(s+1)\mu + (2s_\mathrm{e}+1)\log\left(s+1-\mu\right)\Big]_{Q_1/L_\mathrm{R}^2\Pi}^{Q_2/L_\mathrm{R}^2\Pi} \tag{B.19}$$

using the substitution $s = Q/L_\mathrm{R}^2\Pi$ and $s_\mathrm{e} = Q_\mathrm{e}/L_\mathrm{R}^2\Pi$, $\mu = u(Q)/L_\mathrm{R}\Pi = \sqrt{s^2 + 2(s-s_\mathrm{e})}$.

B.3.2 Alongshore momentum flux

The velocity $u(x,y)$ is found by differentiating (4.10) and substituting Z from (4.12). Integrating the square of this gives the horizontal momentum flux within the current

$$\begin{aligned}\Delta M_\mathrm{c} = \int_0^Y u^2 dy = (L_\mathrm{R}\Pi)^2 \Bigg(&L_\mathrm{R} Z\left(\frac{Q}{L_\mathrm{R}^2\Pi} + 1 - \frac{Z}{2}\right)\log Z \\ &+ \frac{L_\mathrm{R}}{2}\left(\frac{1}{4} + \left(\frac{Q}{L_\mathrm{R}^2\Pi} + 1 - \frac{Z}{2}\right)^2\right)\left(1-Z^2\right)\Bigg).\end{aligned} \tag{B.20}$$

Using $Z = 1 + s - \mu$ and rearranging gives

$$\Delta M_\mathrm{c} = \frac{L_\mathrm{R}^3\Pi^2}{2}\left((s+1)\mu + \frac{1}{2}(s_\mathrm{e}+1) + (2s_\mathrm{e}+1)\log\left(1+s-\mu\right)\right). \tag{B.21}$$

Note that this differs only by a constant, $(s_\mathrm{e}+1)/2$, from the indefinite integral in (B.19), the expression for the source momentum flux.

B.4 Small amplitude interfacial waves

Contour dynamics simulations of coastal outflows often show small Rossby waves perturbing the steady interface solution (see e.g. figs. 5.2, 5.5 and 5.11). This appendix analyses the linearised dynamics of these waves and derives their dispersion relation. For simplicity the analysis is performed for perturbations to a constant width current, but the arguments generalise straightforwardly to a variable width current so long as this variation is gradual. As noted below, if the current profile varies rapidly in then the perturbations are unstable.

Consider adding a small perturbation of height $\gamma(x,t)$ to the steady constant current width $y=Y$, with corresponding small perturbation to the streamfunction $\eta'(x,y)$. As derived in appendix B.4 these satisfy the linearised problem

$$\nabla^2\eta' - \frac{1}{L_\mathrm{R}^2}\eta' = 0, \qquad y>0, \tag{B.22a}$$

$$\eta' \text{ is continuous}, \qquad y>0, \tag{B.22b}$$

$$\eta' = 0, \qquad y=0, \tag{B.22c}$$

$$\eta' \to 0, \qquad y\to\infty, \tag{B.22d}$$

$$\frac{\partial\gamma}{\partial t} + u\frac{\partial\gamma}{\partial x} = \frac{\partial\eta'}{\partial x}, \qquad y=Y, \tag{B.22e}$$

$$\left[\frac{\partial\eta'}{\partial y}\right] = \Pi\gamma, \qquad y=Y, \tag{B.22f}$$

where $[\cdot]$ denotes the jump in a quantity across the line $y=Y$, and $u=-\eta_y$ is the horizontal velocity due to the steady flow. Look for wavelike perturbations of the

form $\gamma = A\exp(\mathrm{i}(kx-\omega t))$, $\eta' = \bar{\eta}'(y)\exp(\mathrm{i}(kx-\omega t))$. Equation (B.22a) becomes

$$\frac{\partial^2\bar{\eta}'}{\partial y^2} - \kappa^2\bar{\eta}' = 0, \qquad y > 0, \tag{B.23}$$

where $\kappa = \sqrt{k^2 + L_{\mathrm{R}}^{-2}}$. This gives an upper solution η'_U for $y > Y$ satisfying (B.22d)

$$\eta'_U = B\mathrm{e}^{\kappa(Y-y)}\mathrm{e}^{\mathrm{i}(kx-\omega t)}, \tag{B.24}$$

and a lower solution η'_L for $0 < y < Y$

$$\eta'_L = \left(C\mathrm{e}^{\kappa(Y-y)} + D\mathrm{e}^{-\kappa(Y-y)}\right)\mathrm{e}^{\mathrm{i}(kx-\omega t)}. \tag{B.25}$$

Equation (B.22c) shows that

$$D = -C\mathrm{e}^{2\kappa Y}. \tag{B.26}$$

Using this with the condition (B.22b) implies that

$$B = C + D = C\left(1 - \mathrm{e}^{2\kappa Y}\right). \tag{B.27}$$

The kinematic boundary condition (B.22e) shows that

$$\omega = k\left(u(y=Y) - \frac{B}{A}\right). \tag{B.28}$$

$u(y=Y) = Q_{\mathrm{e}}/L_{\mathrm{R}}$ and will be written as u in the following few equations for ease of interpretation. Substituting the values of C and D into (B.22f), which takes the form

$$\kappa(C - B - D) = \Pi A, \tag{B.29}$$

gives

$$\frac{B}{A} = \Pi\frac{\mathrm{e}^{-2\kappa Y} - 1}{2\kappa}. \tag{B.30}$$

Using this in (B.28) gives the dispersion relation

$$\omega = k\left(u + \Pi\frac{1 - \mathrm{e}^{-2\kappa Y}}{2\kappa}\right). \tag{B.31}$$

Taking the limit $L_\mathrm{R} \to \infty$ gives the rigid-lid dispersion relation, which for a current with $\Pi = 1$ and $Q_0 = 1/2$ (giving $Y = 1$) [Johnson and McDonald, 2006] is

$$\omega = \frac{1 - \mathrm{e}^{-2|k|}}{2}, \tag{B.32}$$

and taking the limit $Y \to \infty$ gives the dispersion relation for waves along an escarpment with no wall

$$\omega = k\left(u + \frac{\Pi}{2\kappa}\right). \tag{B.33}$$

The frequency of the small waves as given by (B.31) is real, so they are linearly neutrally stable. The dispersion relation (B.31) gives the phase speed

$$c_\mathrm{p} = \frac{\omega}{k} = u + \Pi\frac{1 - \mathrm{e}^{-2\kappa Y}}{2\kappa}, \tag{B.34}$$

and the group speed

$$c_\mathrm{g} = \frac{\partial\omega}{\partial k} = c_\mathrm{p} - \frac{\Pi k}{2Q_\mathrm{e}^3}\underbrace{\left(1 - \frac{1 + 2\kappa Y}{\mathrm{e}^{2\kappa Y}}\right)}_{>0}. \tag{B.35}$$

The phase speed (B.34) has a component in the positive x-direction owing to advection by the steady flow and a component owing to the Rossby waves which is in the positive (or negative) x-direction for positive (or negative) PV Π. The magnitude of the wave component of c_p is a monotonically increasing function of κ[1] and therefore also of k. So longer waves move faster to the right for positive PV. The maximum leftward speed for negative PV is when $k = 0$ and $\kappa = 1/L_\mathrm{R}$ and is given by

$$\max c_\mathrm{p} = \frac{Q_\mathrm{e}}{L_\mathrm{R}} - \Pi\frac{L_\mathrm{R}}{2}\left(1 - \mathrm{e}^{-2Y/L_\mathrm{R}}\right). \tag{B.36}$$

B.4.1 Small perturbation equations derivation

Here the equations (B.22) governing small perturbations to a steady current are derived. Consider a perturbation of height $\gamma(x,t)$ to the constant height of the steady

[1] $\frac{\partial|c_\mathrm{p}|}{\partial\kappa} = |\Pi|(1 - \underbrace{(1 + 2Y\kappa)\mathrm{e}^{-2Y\kappa}}_{<1})/2\kappa^2$

current Y. From here onward, variables relating to the steady flow will be denoted as usual whereas variables relating to the perturbation will be primed. First the nonlinear evolution equations are derived. The PV of the flow $q + q'$ is equal to Π within the domain bounded by the free surface and 0 outside. As $q = \Pi H(Y - y)$ (for the Heaviside function H, with $H(0) = 0$) this gives the equation for the perturbation PV

$$q' = \nabla^2\eta' - \frac{1}{L_{\mathrm{R}}^2}\eta' = \begin{cases} 0, & y < \min(\gamma, Y), \\ \Pi, & \gamma < y < Y, \\ -\Pi, & Y < y < \gamma, \\ 0, & \max(Y, \gamma) < y. \end{cases} \tag{B.37a}$$

So this problem is equivalent to the propagation of a Rossby wave along an escarpment of height Π. Clearly the streamfunction must be continuous so

$$\eta' \text{ is continuous}, \qquad y > 0. \tag{B.37b}$$

The wall along the x-axis is a streamline for the flow with streamfunction value 0 so

$$\eta' = 0, \qquad y = 0, \tag{B.37c}$$

and the streamfunction must decay to 0 at infinity so

$$\eta' \to 0, \qquad y \to \infty. \tag{B.37d}$$

The kinematic boundary condition that particles remain on the free surface (leaving Y in the equation for the moment) is

$$\frac{\mathrm{D}(Y + \gamma - y)}{\mathrm{D}t} = \frac{\partial Y}{\partial t} + \frac{\partial \gamma}{\partial t} + (u + u')\frac{\partial(Y + \gamma)}{\partial x} - (v + v') = 0, \qquad y = Y + \gamma. \tag{B.37e}$$

The final condition is less obvious but follows from conservation of PV

$$\frac{\mathrm{D}(q + q')}{\mathrm{D}t} = \frac{\partial q'}{\partial t} + (\boldsymbol{u} + \boldsymbol{u}') \cdot \nabla q' + \boldsymbol{u}' \cdot \nabla q = 0, \tag{B.37f}$$

using $q_t = 0$ and $\boldsymbol{u} \cdot \nabla q = 0$.

Now, assuming the disturbance is small and linearising the equations (B.37a)–(B.37e) gives the first five of the linearised evolution equations (B.22a)–(B.22e) i.e.

$$\nabla^2\eta' - \frac{1}{L_{\mathrm{R}}^2}\eta' = 0, \qquad y > 0, \tag{B.38a}$$

$$\eta' \text{ is continuous}, \qquad y > 0, \tag{B.38b}$$

$$\eta' = 0, \qquad y = 0, \tag{B.38c}$$

$$\eta' \to 0, \qquad y \to \infty, \tag{B.38d}$$

$$\frac{\partial\gamma}{\partial t} + u\frac{\partial\gamma}{\partial x} = \frac{\partial\eta'}{\partial x}, \qquad y = Y. \tag{B.38e}$$

In the situation where Y is non-constant, if the steady solution is slowly varying in the x-direction then $\partial Y/\partial x$ is small and (B.38e) is still obtained. If however the contour steepens significantly, for example at a shock in the long wave solution, $\partial Y/\partial x$ will enter (B.38e) causing disturbances to be unstable and grow into a series of large waves along the surface. The final equation

$$\left[\frac{\partial\eta'}{\partial y}\right] = \Pi\gamma, \qquad y = Y, \tag{B.39}$$

is derived as follows.

Linearising (B.37f) gives

$$\frac{\partial q'}{\partial t} + \boldsymbol{u}\cdot\nabla q' + \boldsymbol{u}'\cdot\nabla q = 0. \tag{B.40}$$

For constant width currents $v = 0$, $q_x = 0$ and $q_y = -\Pi\delta(y - Y)$, a delta function, so

$$\frac{\partial q'}{\partial t} + u\frac{\partial q'}{\partial x} - \Pi v'\delta(y - Y) = 0. \tag{B.41}$$

Integrating the perturbation PV q' across the line $y = Y$ gives

$$\lim_{\epsilon\to 0}\int_{Y-\epsilon}^{Y+\epsilon} q'\,\mathrm{d}y = \lim_{\epsilon\to 0}\int_{Y-\epsilon}^{Y+\epsilon} \frac{\partial^2\eta'}{\partial x^2} + \frac{\partial^2\eta'}{\partial y^2} - \frac{1}{L_\mathrm{R}^2}\eta'\,\mathrm{d}y \tag{B.42}$$

$$= \left[\frac{\partial\eta'}{\partial y}\right], \tag{B.43}$$

where $[\cdot]$ denotes the jump in a quantity across the line $y = Y$. The other two terms make no contribution to the integral as η' is continuous. Using this result, (B.41) can be integrated across the line $y = Y$ (using integration by parts for the second term) to give

$$\frac{\partial}{\partial t}\left[\frac{\partial\eta'}{\partial y}\right] + u\frac{\partial}{\partial x}\left[\frac{\partial\eta'}{\partial y}\right] = \Pi v', \qquad y = Y. \tag{B.44}$$

Now, comparing this to the kinematic boundary condition (B.38e) shows that

$$\left(\frac{\partial}{\partial t} + u\frac{\partial}{\partial x}\right)\left(\left[\frac{\partial\eta'}{\partial y}\right] - \Pi\gamma\right) = 0, \qquad y = Y. \tag{B.45}$$

So, the quantity $[\eta'_y] - \Pi\gamma$ is conserved, at leading order, following the flow along the contour. By symmetry across the line $y = Y$ (no perturbation should cause no velocity discontinuity and a positive perturbation should cause a discontinuity of the same magnitude as a negative one), its value must be 0, and the final boundary condition is obtained

$$\left[\frac{\partial\eta'}{\partial y}\right] = \Pi\gamma, \qquad y = Y. \tag{B.46}$$

So the linearised perturbation is equivalent to a vortex sheet of strength $\Pi\gamma$ across the line $y = Y$.

Bibliography

An, B. W. *Modelling outflows, coastal currents and eddies.* PhD thesis, University College London, Jan 2004.

An, B. W. and McDonald, N. R. Coastal currents generated by outflow and vorticity and their interaction with topography. *Continental Shelf Research*, 24(13-14): 1531–1547, Aug 2004.

Andrade, I., Sangrà, P., Hormazabal, S., and Correa-Ramirez, M. Island mass effect in the Juan Fernandez Archipelago (33S), Southeastern Pacific. *Deep Sea Research Part I: Oceanographic Research Papers*, 84:86–99, Feb 2014.

Avicola, G. and Huq, P. Scaling analysis for the interaction between a buoyant coastal current and the continental shelf: experiments and observations. *Journal of Physical Oceanography*, 32(11):3233–3248, Nov 2002.

Avicola, G. and Huq, P. The characteristics of the recirculating bulge region in coastal buoyant outflows. *Journal of Marine Research*, 61(4):435–463, Jul 2003.

Barnes, E. J. Eastern Cook Strait region circulation inferred from satellite–derived, sea–surface, temperature data. *New Zealand Journal of Marine and Freshwater Research*, 19(3):405–411, Mar 1985.

Barton, E. D. *Encyclopedia of Ocean Sciences.* Elsevier, 2001. ISBN 9780122274305.

Batchelor, G. K. *An Introduction to Fluid Dynamics.* Cambridge University Press, Cambridge, 1967. ISBN 0521663962.

Beardsley, R., Limeburner, R., Yu, H., and Cannon, G. Discharge of the Changjiang (Yangtze River) into the East China Sea. *Continental Shelf Research*, 4(1-2):57–76, Jan 1985.

Blondeaux, P. and De Bernardinis, B. On the formation of vortex pairs near orifices. *Journal of Fluid Mechanics*, 135(1):111, Apr 1983.

Boebel, O., Lutjeharms, J., Schmid, C., Zenk, W., Rossby, T., and Barron, C. The Cape Cauldron: a regime of turbulent inter-ocean exchange. *Deep Sea Research Part II: Topical Studies in Oceanography*, 50(1):57–86, Jan 2003.

Brown, W. H. and Michael, C. E. Effect of leading-edge separation on the lift of a delta wing. *J. Aerosp. Sci.*, 21:690, 1954.

Broyden, C. G. A class of methods for solving nonlinear simultaneous equations. *Mathematics of Computation*, 19(92):577–577, 1965.

Caldeira, R. M. A. and Sangrà, P. Complex geophysical wake flows. *Ocean Dynamics*, 62(5):683–700, Mar 2012.

Cenedese, C. Laboratory experiments on mesoscale vortices interacting with two islands. *Journal of Geophysical Research*, 110(C9):C09023, 2005.

Chant, R. Interactions between estuaries and coasts: river plumestheir formation transport and dispersal. *Treatise on Estuarine and Coastal Science*, 2011.

Chant, R., Wilkin, J., Zhang, W., Choi, B.-J., Hunter, E., Castelao, R., Glenn, S., Jurisa, J., Schofield, O., Houghton, R., Kohut, J., Frazer, T., and Moline, M. Dispersal of the Hudson River plume in the New York Bight: synthesis of observational and mumerical studies during LaTTE, 2008.

Chapman, D. C. and Beardsley, R. C. On the origin of shelf water in the Middle Atlantic Bight. *Journal of Physical Oceanography*, 19(3):384–391, Mar 1989.

Chelton, D. B., DeSzoeke, R. A., Schlax, M. G., El Naggar, K., and Siwertz, N. Geographical variability of the first baroclinic Rossby radius of deformation. *Journal of Physical Oceanography*, 28(3):433–460, Mar 1998.

Chen, S.-N. Enhancement of alongshore freshwater transport in surface-advected river plumes by tides. *Journal of Physical Oceanography*, 44(11):2951–2971, Nov 2014.

Collins, C., Garfield, N., Rago, T., Rischmiller, F., and Carter, E. Mean structure of the inshore countercurrent and California undercurrent off Point Sur, California. *Deep Sea Research Part II: Topical Studies in Oceanography*, 47(5-6):765–782, May 2000.

Cortelezzi, L. On the unsteady separated flow past a semi-infinite plate: Exact solution of the Brown and Michael model, scaling, and universality. *Physics of Fluids*, 7(3):526, Mar 1995.

Cortelezzi, L. and Leonard, A. Point vortex model of the unsteady separated flow past a semi-infinite plate with transverse motion. *Fluid Dynamics Research*, 11 (6):263–295, Jun 1993.

Crowdy, D. G. and Marshall, J. S. Analytical formulae for the Kirchhoff–Routh path function in multiply connected domains. *Proceedings of the Royal Society A: Mathematical, Physical and Engineering Sciences*, 461(2060):2477–2501, Aug 2005a.

Crowdy, D. G. and Marshall, J. S. The motion of a point vortex through gaps in walls. *Journal of Fluid Mechanics*, 551(-1):31, Mar 2006.

Crowdy, D. G. and Marshall, J. S. The motion of a point vortex around multiple circular islands. *Physics of Fluids*, 17(5):056602, May 2005b.

Davies, P., Jacobs, P., and Mofor, L. A laboratory study of buoyant fresh-water boundary currents in tidal cross-flows. *Oceanologica Acta*, 16(5-6):489–503, Jan 1993.

Dewar, W. K., McWilliams, J. C., and Molemaker, M. J. Centrifugal instability and mixing in the California Undercurrent. *Journal of Physical Oceanography*, 45(5): 1224–1241, May 2015.

Dewar, W. K. Baroclinic eddy interaction with isolated topography. *Journal of Physical Oceanography*, 32(10):2789–2805, Oct 2002.

Donato, T. F. and Marmorino, G. O. The surface morphology of a coastal gravity current. *Continental Shelf Research*, 22(1):141–146, Jan 2002.

Dong, C., McWilliams, J. C., and Shchepetkin, A. F. Island wakes in deep water. *Journal of Physical Oceanography*, 37(4):962–981, Apr 2007.

Dritschel, D. G. Contour surgery: A topological reconnection scheme for extended integrations using contour dynamics. *Journal of Computational Physics*, 77(1): 240–266, Jul 1988.

Duran-Matute, M. and Velasco Fuentes, O. U. Passage of a barotropic vortex through a gap. *Journal of Physical Oceanography*, 38(12):2817–2831, Dec 2008.

Dzwonkowski, B. and Yan, X.-H. Tracking of a Chesapeake Bay estuarine outflow plume with satellite-based ocean color data. *Continental Shelf Research*, 25(16): 1942–1958, Oct 2005.

Eldredge, J. and Wang, C. High-fidelity simulations and low-order modeling of a rapidly pitching plate. *AIAA Paper 2010-4281 40th AIAA Fluid Dynamics Conference*, 2010.

Fong, D., Geyer, W., and Signell, R. The wind-forced response on a buoyant coastal current: Observations of the western Gulf of Maine plume. *Journal of Marine Systems*, 12(1-4):69–81, Aug 1997.

Fong, D. A. and Geyer, W. R. Response of a river plume during an upwelling favorable wind event. *Journal of Geophysical Research*, 106(C1):1067, 2001.

Fong, D. A. and Geyer, W. R. The alongshore transport of freshwater in a surface-trapped river plume. *Journal of Physical Oceanography*, 32(3):957–972, Mar 2002.

Fratantoni, D. M. and Glickson, D. A. North Brazil Current ring generation and evolution observed with SeaWiFS. *Journal of Physical Oceanography*, 32(3):1058–1074, Mar 2002.

Fratantoni, D. M. and Richardson, P. L. The evolution and demise of North Brazil Current rings. *Journal of Physical Oceanography*, 36(7):1241–1264, Jul 2006.

Garraffo, Z.D., Johns, W., Chassignet, E., and Goni, G. North Brazil Current rings and transport of southern waters in a high resolution numerical simulation of the North Atlantic. 68:375–409, Jan 2003.

Garvine, R. W. A dynamical system for classifying buoyant coastal discharges. *Continental Shelf Research*, 15(13):1585–1596, Nov 1995.

Garvine, R. W. The impact of model configuration in studies of buoyant coastal discharge. *Journal of Marine Research*, 59(2):193–225, Mar 2001.

Gómez, R. C. C. and Bulgakov, S. N. Remote sensing observations of the coherent and non-coherent ring structures in the vicinity of Lesser Antilles. *Annales Geophysicae*, 25(2):331–340, Mar 2007.

Goni, G. J. and Johns, W. E. A census of North Brazil Current Rings observed from TOPEX/POSEIDON altimetry: 1992-1998. *Geophysical Research Letters*, 28(1): 1–4, Jan 2001.

Graham, J. M. R. The forces on sharp-edged cylinders in oscillatory flow at low Keulegan-Carpenter numbers. *Journal of Fluid Mechanics*, 97(02):331, Apr 1980.

Graham, J. M. R. The lift on an aerofoil in starting flow. *Journal of Fluid Mechanics*, 133(-1):413, Apr 1983.

Gula, J., Molemaker, M. J., and McWilliams, J. C. Topographic vorticity generation, submesoscale instability and vortex street formation in the Gulf Stream. *Geophysical Research Letters*, 42(10):4054–4062, May 2015.

Hacker, J. N. and Linden, P. F. Gravity currents in rotating channels. Part 1. Steady-state theory. *Journal of Fluid Mechanics*, 457:295–324, Apr 2002.

Heywood, K. J., Stevens, D. P., and Bigg, G. R. Eddy formation behind the tropical island of Aldabra. *Deep Sea Research Part I: Oceanographic Research Papers*, 43 (4):555–578, Apr 1996.

Hickey, B. M., Pietrafesa, L. J., Jay, D. A., and Boicourt, W. C. The Columbia River Plume Study: Subtidal variability in the velocity and salinity fields. *Journal of Geophysical Research*, 103(C5):10339, 1998.

Hickey, B. M., Geier, S., Kachel, N., and MacFadyen, A. A bi-directional river plume: The Columbia in summer. *Continental Shelf Research*, 25(14):1631–1656, sep 2005.

Horner-Devine, A., Fong, D. A., Monismith, S. G., and Maxworthy, T. Laboratory experiments simulating a coastal river inflow. *Journal of Fluid Mechanics*, 555: 203, May 2006.

Horner-Devine, A. R. The bulge circulation in the Columbia River plume. *Continental Shelf Research*, 29(1):234–251, Jan 2009.

Horner-Devine, A. R., Fong, D. A., and Monismith, S. G. Evidence for the inherent unsteadiness of a river plume: Satellite observations of the Niagara River discharge. *Limnology and Oceanography*, 53(6):2731–2737, 2008.

Horner-Devine, A. R., Hetland, R. D., and MacDonald, D. G. Mixing and transport in coastal river plumes. *Annual Review of Fluid Mechanics*, 47(1):569–594, Jan 2015.

Howe, M. S. Emendation of the Brown and Michael equation, with application to sound generation by vortex motion near a half-plane. *Journal of Fluid Mechanics*, 329:89–101, Dec 1996.

Isobe, A. Ballooning of river-plume bulge and its stabilization by tidal currents. *Journal of Physical Oceanography*, 35(12):2337–2351, Dec 2005.

Isoguchi, O., Shimada, M., Sakaida, F., and Kawamura, H. Investigation of Kuroshio-induced cold-core eddy trains in the lee of the Izu Islands using high-resolution satellite images and numerical simulations. *Remote Sensing of Environment*, 113 (9):1912–1925, sep 2009.

Jiang, M., Zhou, M., Libby, S. P., and Anderson, D. M. Dynamics of a mesoscale eddy off Cape Ann, Massachusetts in May 2005. *Deep Sea Research Part I: Oceanographic Research Papers*, 58(11):1130–1146, Nov 2011.

Jiménez, B., Sangrà, P., and Mason, E. A numerical study of the relative importance of wind and topographic forcing on oceanic eddy shedding by tall, deep water islands. *Ocean Modelling*, 22(3-4):146–157, Jan 2008.

Jochumsen, K., Rhein, M., Hüttl-Kabus, S., and Böning, C. W. On the propagation

and decay of North Brazil Current rings. *Journal of Geophysical Research*, 115 (C10):C10004, Oct 2010.

Johns, W. E., Zantopp, R. J., and Goni, G. *Interhemispheric Water Exchange in the Atlantic Ocean*, volume 68 of *Elsevier Oceanography Series*. Elsevier, 2003. ISBN 9780444512673.

Johnson, E. R. and McDonald, N. R. The motion of a vortex near a gap in a wall. *Physics of Fluids*, 16:462–469, Mar 2004a.

Johnson, E. R. and McDonald, N. R. The motion of a vortex near two circular cylinders. *Proceedings of the Royal Society A: Mathematical, Physical and Engineering Sciences*, 461(460):939–954, Apr 2004b.

Johnson, E. R. and McDonald, N. R. The point island approximation in vortex dynamics. *Geophysical and Astrophysical Fluid Dynamics*, 99:49–60, Mar 2005a.

Johnson, E. R. and McDonald, N. R. Vortices near barriers with multiple gaps. *Journal of Fluid Mechanics*, 531:335–358, May 2005b.

Johnson, E. R. and McDonald, N. R. Vortical source-sink flow against a wall: The initial value problem and exact steady states. *Physics of Fluids*, 18(7):076601, Jul 2006.

Johnson, E. R. and Southwick, O. R. Free-surface vorticies near boundaries. *In preparation*, 2016.

Klinger, B. A. Baroclinic eddy generation at a sharp corner in a rotating system. *Journal of Geophysical Research*, 99(C6):12515, 1994.

Krasny, R. Desingularization of periodic vortex sheet roll-up. *Journal of Computational Physics*, 65(2):292–313, Aug 1986.

Kubokawa, A. On the behaviour of outflows with low potential vorticity from a sea strait. *Tellus A*, 1991.

Lake, I., Borenäs, K., and Lundberg, P. Potential-vorticity characteristics of the Faroe Bank Channel deep-water overflow. *Journal of Physical Oceanography*, 35 (6):921–932, Jun 2005.

Lane-Serff, G. F. and Baines, P. G. Eddy formation by overflows in stratified water. *Journal of Physical Oceanography*, 30(2):327–337, Feb 2000.

Lentz, S. The response of buoyant coastal plumes to upwelling-favorable winds. *Journal of Physical Oceanography*, 34(11):2458–2469, Nov 2004.

Lentz, S. J. and Helfrich, K. R. Buoyant gravity currents along a sloping bottom in a rotating fluid. *Journal of Fluid Mechanics*, 464:251–278, Aug 2002.

Lutjeharms, J. R. E., Boebel, O., and Rossby, H. T. Agulhas cyclones. *Deep Sea Research Part II: Topical Studies in Oceanography*, 50(1):13–34, Jan 2003.

Manela, A. and Huang, L. Point vortex model for prediction of sound generated by a wing with flap interacting with a passing vortex. *The Journal of the Acoustical Society of America*, 133(4):1934–44, Apr 2013.

Marques, G. M., Padman, L., Springer, S. R., Howard, S. L., and Özgökmen, T. M. Topographic vorticity waves forced by Antarctic dense shelf water outflows. *Geophysical Research Letters*, 41(4):1247–1254, Feb 2014.

Martin, J. R. and Lane-Serff, G. F. Rotating gravity currents. Part 1. Energy loss theory. *Journal of Fluid Mechanics*, 522:35–62, Jan 2005.

Martin, J. R., Smeed, D. A., and Lane-Serff, G. F. Rotating gravity currents. Part 2. Potential vorticity theory. *Journal of Fluid Mechanics*, 522:63–89, Jan 2005.

Matano, R. P. and Palma, E. D. The spindown of bottom-trapped plumes. *Journal of Physical Oceanography*, 40(7):1651–1658, Jul 2010a.

Matano, R. P. and Palma, E. D. The upstream spreading of bottom-trapped plumes. *Journal of Physical Oceanography*, 40(7):1631–1650, Jul 2010b.

McCreary, J. P., Zhang, S., and Shetye, S. R. Coastal circulations driven by river outflow in a variable-density 1 1/2-layer model. *Journal of Geophysical Research*, 102(C7):15535, 1997.

Michelin, S. and Llewellyn Smith, S. G. Falling cards and flapping flags: understanding fluid solid interactions using an unsteady point vortex model. *Theoretical and Computational Fluid Dynamics*, 24(1):195–200, 2010.

Michelin, S., Llewellyn Smith, S. G., and Glover, B. J. Vortex shedding model of a flapping flag. *Journal of Fluid Mechanics*, 617(1):1–10, 2008.

Michelin, S. and Llewellyn Smith, S. G. An unsteady point vortex method for coupled fluid solid problems. *Theoretical and Computational Fluid Dynamics*, 23 (2):127–153, 2009.

Molemaker, M. J., McWilliams, J. C., and Dewar, W. K. Submesoscale instability and generation of mesoscale anticyclones near a separation of the California Undercurrent. *Journal of Physical Oceanography*, 45(3):613–629, Mar 2015.

Nelson, R. B. and McDonald, N. R. Finite area vortex motion on a sphere with impenetrable boundaries. *Physics of Fluids*, 21(1):016602, Jan 2009.

Nilawar, R. S., Johnson, E. R., and McDonald, N. R. Finite Rossby radius effects on vortex motion near a gap. *Physics of Fluids*, 24(6):066601, Jun 2012.

Nof, D. Eddy-wall interactions. *Journal of Marine Research*, 46(3):527–555, Aug 1988.

Nof, D. The momentum imbalance paradox revisited. *Journal of Physical Oceanography*, 35(10):1928–1939, Oct 2005.

Nof, D. and Pichevin, T. The ballooning of outflows. *Journal of Physical Oceanography*, 31(10):3045–3058, Oct 2001.

Nof, D., Pichevin, T., and Sprintall, J. "Teddies" and the origin of the Leeuwin Current. *Journal of Physical Oceanography*, 32(9):2571–2588, sep 2002.

Pedrizzetti, G. Vortex formation out of two-dimensional orifices. *Journal of Fluid Mechanics*, 655:198–216, May 2010.

Penven, P., Lutjeharms, J. R. E., Marchesiello, P., Roy, C., and Weeks, S. J. Generation of cyclonic eddies by the Agulhas Current in the lee of the Agulhas Bank. *Geophysical Research Letters*, 28(6):1055–1058, Mar 2001.

Pichevin, T. and Nof, D. The momentum imbalance paradox. *Tellus A*, 49(2): 298–319, Mar 1997.

Piedeleu, M., Sangrà, P., Sánchez-Vidal, A., Fabrés, J., Gordo, C., and Calafat, A. An observational study of oceanic eddy generation mechanisms by tall deep-water islands (Gran Canaria). *Geophysical Research Letters*, 36(14):L14605, Jul 2009.

Pingree, R. D. A shallow subtropical subducting westward propagating eddy (Swesty). *Philosophical Transactions of the Royal Society A: Mathematical, Physical and Engineering Sciences*, 354(1710):979–1026, May 1996.

Rabalais, N. N., Turner, R. E., and Wiseman, W. J. Gulf of Mexico hypoxia, a.k.a. "the dead zone". *Annual Review of Ecology and Systematics 33. Annual Reviews: 23563*, 2002.

Richardson, P. Caribbean Current and eddies as observed by surface drifters. *Deep Sea Research Part II: Topical Studies in Oceanography*, 52(3-4):429–463, Feb 2005.

Richardson, P., Bower, A., and Zenk, W. A census of Meddies tracked by floats. *Progress in Oceanography*, 45(2):209–250, Feb 2000.

Rott, N. Diffraction of a weak shock with vortex generation. *Journal of Fluid Mechanics*, 1(01):111, Mar 1956.

Sadoux, S., Baey, J.-M., Fincham, A., and Renouard, D. Experimental study of the stability of an intermediate current and its interaction with a cape. *Dynamics of Atmospheres and Oceans*, 31(1-4):165–192, Jan 2000.

Saffman, P. G. *Vortex Dynamics*. Cambridge University Press, Cambridge, 1992.

Sangrà, P., Auladell, M., Marrero-Díaz, A., Pelegrí, J. L., Fraile-Nuez, E., Rodríguez-Santana, A., Martín, J. M., Mason, E., and Hernández-Guerra, A. On the nature of oceanic eddies shed by the Island of Gran Canaria. *Deep Sea Research Part I: Oceanographic Research Papers*, 54(5):687–709, May 2007.

Sangrà, P., Pascual, A., Rodríguez-Santana, Á., Machín, F., Mason, E., McWilliams, J. C., Pelegrí, J. L., Dong, C., Rubio, A., Arístegui, J., Marrero-Díaz, Á., Hernández-Guerra, A., Martínez-Marrero, A., and Auladell, M. The Canary Eddy Corridor: A major pathway for long-lived eddies in the subtropical North Atlantic.

Deep Sea Research Part I: Oceanographic Research Papers, 56(12):2100–2114, Dec 2009.

Serra, N., Ambar, I., and Käse, R. H. Observations and numerical modelling of the Mediterranean outflow splitting and eddy generation. *Deep Sea Research Part II: Topical Studies in Oceanography*, 52(3-4):383–408, Feb 2005.

Sheng, J. X., Ysasi, A., Kanso, E., Nitsche, M., and Schneider, K. Simulating vortex wakes of flapping plates. *IMA Volume on Natural Locomotion in Fluids and on Surfaces: Swimming, Flying, and Sliding*, 155:255–262, 2011.

Simmons, H. L. and Nof, D. The squeezing of eddies through gaps. *Journal of Physical Oceanography*, 32(1):314–335, Jan 2002.

Sneddon, I. N. *The Use of Integral Transforms*. 1972.

Spall, M. A. and Price, J. F. Mesoscale variability in Denmark Strait: the PV outflow hypothesis. *Journal of Physical Oceanography*, 28(8):1598–1623, Aug 1998.

Stern, M. E. and Pratt, L. J. Dynamics of vorticity fronts. *Journal of Fluid Mechanics*, 161:513, Apr 1985.

Takikawa, T., Onitsuka, G., Fukudome, K.-i., Yoon, J.-H., Morimoto, A., Moku, M., and Watanabe, A. Spatial and temporal variation of a cyclonic eddy detected downstream of the Tsushima Islands in November 2007. *Estuaries and Coasts*, 34 (4):775–784, Apr 2011.

Tanabe, A. and Cenedese, C. Laboratory experiments on mesoscale vortices colliding with an island chain. *Journal of Geophysical Research*, 113(C4):C04022, Apr 2008.

Teinturier, S., Stegner, A., Didelle, H., and Viboud, S. Small-scale instabilities of an island wake flow in a rotating shallow-water layer. *Dynamics of Atmospheres and Oceans*, 49(1):1–24, Jan 2010.

Thomas, P. J. and Linden, P. F. Rotating gravity currents: small-scale and large-scale laboratory experiments and a geostrophic model. *Journal of Fluid Mechanics*, 578:35, Apr 2007.

Trenberth, K. E., Smith, L., Qian, T., Dai, A., and Fasullo, J. Estimates of the global water budget and its annual cycle using observational and model data. *Journal of Hydrometeorology*, 8(4):758–769, Aug 2007.

van Maren, D. and Hoekstra, P. Seasonal variation of hydrodynamics and sediment dynamics in a shallow subtropical estuary: the Ba Lat River, Vietnam. *Estuarine, Coastal and Shelf Science*, 60(3):529–540, 2004.

Walters, R. A., Gillibrand, P. A., Bell, R. G., and Lane, E. M. A study of tides and currents in Cook Strait, New Zealand. *Ocean Dynamics*, 60(6):1559–1580, Nov 2010.

Whitehead, J. The deflection of a baroclinic jet by a wall in a rotating fluid. *J. Fluid Mech*, 1985.

Wu, H., Deng, B., Yuan, R., Hu, J., Gu, J., Shen, F., Zhu, J., and Zhang, J. Detiding measurement on transport of the Changjiang-derived buoyant coastal current. *Journal of Physical Oceanography*, 43(11):2388–2399, Nov 2013.

Yankovsky, A. E. The cyclonic turning and propagation of buoyant coastal discharge along the shelf. *Journal of Marine Research*, 58(4):585–607, Jul 2000.

Yankovsky, A. E. and Chapman, D. C. A simple theory for the fate of buoyant coastal discharges. *Journal of Physical Oceanography*, 27(7):1386–1401, Jul 1997.

Ysasi, A., Kanso, E., and Newton, P. K. Wake structure of a deformable Joukowski airfoil. *Physica D: Nonlinear Phenomena*, 240(20):1574–1582, Oct 2011.